

# **High Radio Frequency Applications of Soft Conductors and Flexible Dielectrics**

Xiaoyou Lin

A thesis submitted to  
Auckland University of Technology  
in fulfilment of the requirements for the degree of  
Doctor of Philosophy (PhD)

2018

Department of Electrical and Electronic Engineering  
School of Engineering, Computer and Mathematical Sciences  
Auckland University of Technology

# Abstract

As essential components of smart textiles, flexible radio-frequency (RF) structures have gained much attention in recent years. These structures are based on flexible metal foils, conductive textiles, conductive inks and various types of dielectric fabrics, covering most types of passive RF devices such as transmission lines, antennae and periodic structures (e.g. high-impedance surfaces and filters). With the use of microwave band increasingly constrained by spectrum congestion, solutions for future wireless systems are being developed to use quasi-millimetre-wave (quasi-mm-wave) and mm-wave bands, which offer wider bandwidth and faster bit rate in the higher frequency range above 20 GHz.

From the literature review, it is identified that research gaps still exist in designing wearable RF devices at mm-wave bands. Therefore, this thesis proposes and studies the design of such wearable RF structures, including a method to characterise dielectric materials at mm-wave bands, electromagnetic bandgap (EBG) that aims to enhance the performance of the on-body antennae, and body sensing antennae based on changing dielectric constant of fabric-based substrates under different temperature and humidity levels. The frequency band of interest covers the unlicensed industrial, scientific and medical (ISM) band (24.5 GHz), and two candidate bands (28 and 38 GHz) for future 5<sup>th</sup> Generation (5G) cellular networks.

This thesis is organised as below: the first three chapters cover the introduction, essential background concepts, and literature review. Thereafter, the thesis proposes a novel hybrid-transmission-line (hybrid-TL) method for characterising flexible and thin dielectric laminates in a fast and accurate manner. Unlike other existing techniques based on transmission-line method, the RF characteristics of the transitions are not required to be known a priori due to the use of two error boxes by the proposed hybrid-TL method.

Next, a flexible fractal EBG structure is investigated for body-worn antennae operating at mm-wave bands. The proposed EBG can significantly improve the performance of wearable antennae such as an optimised operating bandwidth and enhanced radiation gain. In addition, the measurements show that the EBG structure can eliminate most of the influences to the antennae asserted from the human bodies.

The final part of this thesis studies the variation of dielectric behaviours of selected textile fabrics when they are subjected to different temperature and humidity levels. A humidity sensing antenna operating at 38 GHz is designed, fabricated and evaluated. The results show that the resonant frequency of the designed antenna has a relatively linear response to ambient humidity and high sensing resolution of 26 MHz per 1% relative humidity (RH).

# Table of Contents

Abstract .....	I
List of Figures .....	VII
List of Tables.....	X
Attestation of Authorship.....	XI
Acknowledgement.....	XII
List of Acronyms .....	XIV
List of Symbols .....	XVII
Chapter 1 Introduction .....	1
1.1. Overview .....	1
1.2. Research Gaps, Motivations and Scope .....	2
1.3. Contributions and Publications .....	3
1.4. Thesis Organisation .....	6
Chapter 2 Background .....	7
2.1. Introduction .....	7
2.2. Theoretical Background of RF Systems.....	7
2.2.1. Transmission line .....	7
2.2.2. Two-port network and scattering parameters.....	11
2.3. Antennae and High-Impedance Surfaces .....	13
2.3.1. Antennae .....	13
2.3.2. High impedance surfaces .....	18
2.4. Smart Textiles and Body Area Networks.....	19
2.5. Millimetre-wave Techniques.....	23
2.5.1. Millimetre-wave spectrum .....	23
2.5.2. Wave propagation at mm-wave frequencies .....	24
2.5.3. Hardware architectures and devices.....	24
2.6. Simulation Environment and Measurement System .....	25

2.6.1.	Finite element method and ANSYS Electronics Desktop.....	25
2.6.2.	Measurement facilities .....	26
2.7.	Summary .....	28
Chapter 3	Literature Review.....	29
3.1.	Introduction .....	29
3.2.	Material Characterisation at Radio Frequency .....	29
3.2.1.	Dielectric material characterisation.....	30
3.2.2.	Conductive material characterisation.....	36
3.3.	Electromagnetic Bandgaps .....	38
3.3.1.	Significance of using EBG.....	38
3.3.2.	Typical EBG structures .....	39
3.3.3.	Fabric EBG structures .....	41
3.4.	Wireless Sensing Antennae .....	42
3.4.1.	Overview .....	42
3.4.2.	Sensing by mechanical deformation .....	43
3.4.3.	Sensing by electrical permittivity .....	46
3.5.	Summary .....	47
Chapter 4	A Hybrid-Microstrip-Line Method for Material Characterisation.....	48
4.1.	Introduction .....	48
4.2.	Hybrid-transmission-line Method .....	49
4.2.1.	Hybrid-transmission-line method.....	50
4.2.2.	Test fixture design.....	53
4.3.	Characterisation Procedure.....	56
4.3.1.	Measurement setup and steps.....	56
4.3.2.	Measurement illustration.....	57
4.4.	Complex Permittivity of Measured Materials .....	58
4.5.	Validation and Discussion.....	63
4.5.1.	Method validation .....	63

4.5.2.	Accuracy comparison with two-transmission-line method.....	64
4.6.	Summary .....	66
Chapter 5	Flexible EBG Design for MM-wave Wearable Antennae .....	68
5.1.	Introduction .....	68
5.2.	Proposed Electromagnetic Bandgap Structure .....	69
5.2.1.	Design of the EBG .....	70
5.3.	Design of Coplanar Waveguide Antenna .....	77
5.4.	Integration of EBG with the CPW antenna .....	79
5.5.	On-body Performance of the EBG-back CPW Antenna .....	83
5.5.1.	Bending performance .....	83
5.5.2.	On-body performance .....	84
5.6.	Summary .....	87
Chapter 6	Wearable Environmental Sensing Antennae over 5G Network.....	89
6.1.	Introduction .....	89
6.2.	Design of the Sensing Antenna .....	90
6.2.1.	Antenna's geometry .....	91
6.2.2.	Simulated results of the antenna .....	93
6.3.	Material Characterisation .....	95
6.3.1.	Test setup .....	96
6.3.2.	Temperature behaviour .....	97
6.3.3.	Humidity behaviour .....	98
6.4.	Performance of the Humidity Sensing Antenna .....	100
6.4.1.	Fabricated antenna prototype .....	100
6.4.2.	Antenna response to ambient humidity.....	102
6.5.	Summary .....	105
Chapter 7	Conclusion and Future Work .....	106
7.1.	Conclusion.....	106
7.2.	Contributions .....	106

7.3. Limitations and Future work .....	108
Appendix A Design of Test Fixture .....	110
A.1. Bill of Materials.....	110
A.2. Mechanical Drawings .....	111
A.2.1. Test fixture ear .....	111
A.2.2. Fixture base .....	111
A.2.3. Dielectric board.....	113
Appendix B MATLAB Code for Characterising Dielectric Materials.....	114
References .....	116

# List of Figures

Figure 2.1. Lumped-element equivalent circuit of a transmission line [28].	8
Figure 2.2. Transmission and reflection coefficients [28].	8
Figure 2.3. Stripline: (a) geometry; (b) EM field distribution [28].	10
Figure 2.4. CPW line: (a) geometry; (b) EM field distribution [29].	10
Figure 2.5. Microstrip line: (a) geometry; (b) EM field distribution [28].	10
Figure 2.6. Two-port network: (a) model; and (b) signal flow graph [28].	11
Figure 2.7. Cascading network consisting of $n$ networks.	13
Figure 2.8. Rectangular microstrip antenna: (a) geometry; (b) equivalent circuit.	14
Figure 2.9. Geometry of a coplanar waveguide antenna.	15
Figure 2.10. Resonant frequency and bandwidth of a microstrip patch antenna.	16
Figure 2.11. Radiation pattern of a dipole antenna: (a) 3D pattern; (b) 2D pattern with E-plane (solid line) and H-plane (dash line).	17
Figure 2.12. (a) In-phase reflection of AMC; (b) reflection diagram of EBG [36].	19
Figure 2.13. (a) Mushroom-like EBG and its equivalent circuit [35]; (b) suspended stripline for measuring transmission coefficient.	19
Figure 2.14. Basic architecture of sensor nodes [47].	22
Figure 2.15. Allocation of EM spectrum [28].	23
Figure 2.16. Illustration of a direct conversion receiver and transmitter [52].	25
Figure 2.17. FEM process in HFSS.	26
Figure 2.18. (a) RF anechoic chamber; (b) antenna positioning system.	27
Figure 2.19. Climate test chamber (Model: WEISS WKL34).	28
Figure 3.1. Two-transmission line method: (a) short line; (b) long line.	31
Figure 3.2. Covered-transmission-line method: (a) uncovered TL; (b) covered TL and (c) side view of covered-TL method.	33
Figure 3.3. Resonator method: (a) model; (b) measured by a UTF.	35
Figure 3.4. Microstrip resonator.	38
Figure 3.5. UC-EBG structure with periodic square pads [79].	40
Figure 3.6. Moore space-filling geometry with different iterations.	41
Figure 3.7. The working principle of: (a) pressure sensing antenna; (b) strain sensing antenna; and (c) a shift to the resonant frequency ( $f_0$ ) due to the external force.	44
Figure 3.8. Smart belly band: (a) knitting structure; (b) knitted microstrip sensing antenna; and (c) $S_{11}$ response to the stretch [105].	45

Figure 4.1. Hybrid-TL model for (a) uncovered; (b) covered scenarios and (c) side view of covered scenario. ....	50
Figure 4.2. Reflections at impedance discontinuous points. ....	53
Figure 4.3. Designed test fixture: (a) top view; (b) side view; and (c) plastic base model. ....	54
Figure 4.4. Measured $S$ -parameters of the designed test fixture. ....	55
Figure 4.5. Measuring $S$ -parameters of the fixture: (a) test setup; and (b) MUT placed on the fixture. ....	56
Figure 4.6. Simulated and measured $S_{21}$ phase for RT/d5880. ....	58
Figure 4.7. Simulated and measured $S_{21}$ phase for polyester. ....	58
Figure 4.8. Test samples. ....	59
Figure 4.9. Microstrip antenna designed based on the characterised polyester fabric: (a) geometry; and (b) fabricated prototype. ....	63
Figure 4.10. Measured and Simulated $S_{11}$ of the microstrip antenna. ....	64
Figure 4.11. Samples fabricated for L-L method: group (a) RT/d5880; (b) polyester fabric (Unit in mm). ....	65
Figure 4.12. Characterised $\epsilon_r$ for (a) RT/d5880; and (b) polyester fabric. ....	65
Figure 5.1. Domestic steam iron (Philips NI-P300T) for bonding fabric materials. ....	70
Figure 5.2. Fabrication of sample 5: (a) a thermal-bonding film sandwiched between two polyester fabrics; and (b) a finalised four-layer polyester fabric. ....	71
Figure 5.3. Laser-cut slots and strips on conductive fabric. ....	71
Figure 5.4. Laser-cut conductive patterns from copper foil. ....	72
Figure 5.5. Laser-cut conductive patterns under an optical microscope. ....	73
Figure 5.6. Proposed EBG: (a) geometry; and (b) equivalent circuit of one unit cell. ...	73
Figure 5.7. Microstrip line with three unit cells EBG: (a) top view; and (b) bottom view. ...	74
Figure 5.8. Simulated magnitude of transmission coefficient ( $S_{21}$ ) for different values of: (a) $S_1$ ; (b) $S_2$ ; (c) $W_1$ ; and (d) $W_2$ . In each sub-figure, other dimension values are maintained as shown in Table 5.1. The unit is in mm. ....	75
Figure 5.9. Simulated current flow of one unit cell. ....	76
Figure 5.10. EBG with $3 \times 3$ unit-cells fabricated on polyester fabric substrate. ....	76
Figure 5.11. CPW antenna: (a) geometry; (b) fabricated prototype; and (c) side view. ...	78
Figure 5.12. Simulated and the measured $S_{11}$ of the fabricated CPW antenna. ....	78
Figure 5.13. Fabricated EBG-backed CPW antenna. ....	79
Figure 5.14. Measured magnitude of reflection coefficient of the CPW antenna with and without the EBG in free space. ....	80

Figure 5.15. Current distribution of the CPW antenna (a) with; and (b) without the EBG at 24, 28 and 38 GHz.....	81
Figure 5.16. Setup for measuring radiation patterns. ....	81
Figure 5.17. Measured radiation patterns for the CPW antenna with EBG (solid line) and without EBG (dashed line) at 24, 28 and 38 GHz in free space. ....	82
Figure 5.18. Bending of the EBG-backed CPW antenna along (a) $x$ ; and (b) $y$ axes on a rolled foam. ....	83
Figure 5.19. Measured magnitude of the reflection coefficient along $x$ and $y$ axes.....	84
Figure 5.20. EBG-backed CPW antenna attached on the (a) forearm; (b) thigh; and (c) chest.....	85
Figure 5.21. Measured magnitude of $S_{11}$ of the EBG-backed CPW antenna on human body.....	86
Figure 5.22. Measured radiation pattern of the EBG-backed CPW antenna in free space (dashed line) and on-body (solid line) at 28 GHz. ....	86
Figure 6.1. Geometry of the microstrip antenna: (a) top view; and (b) side view. ....	92
Figure 6.2. Antenna on the body phantom.....	93
Figure 6.3. Simulated magnitude of $S_{11}$ for the antenna on (a) polyester fabric; and (b) cotton fabric. ....	94
Figure 6.4. Radiation patterns for the antenna on polyester fabric: (a) free space; and (b) on body.....	95
Figure 6.5. Radiation patterns for the antenna on cotton fabric: (a) free space; and (b) on body.....	95
Figure 6.6. Test setup inside the climate test chamber. ....	96
Figure 6.7. Measured phase of transmission coefficient under different RH levels. ....	99
Figure 6.8. Simulated $S_{11}$ response with the variation of RH levels. ....	100
Figure 6.9. Fabricated prototype of the humidity sensing antenna. ....	101
Figure 6.10. Measurement setup of measuring $S_{11}$ . ....	101
Figure 6.11. Measured and simulated $S_{11}$ for the sensing antenna.....	102
Figure 6.12. Measured $S_{11}$ response of antenna to ambient RH level.....	103
Figure 6.13. Humidity-resonant frequency relationship. ....	103
Figure A.1. Test fixture ear: (a) 3D view; (b) 2D view. ....	111
Figure A.2. Test fixture base: (a) top view; (b) zoom-in of the top part of the base. ...	112
Figure A.3. Dielectric board and microstrip line (unit: mm). ....	113

# List of Tables

Table 2.1. Parameters of stripline, CPW and microstrip line.....	11
Table 2.2. Conversion between $[S]$ and $[T]$ .....	13
Table 2.3. Free-space loss for different operating frequencies ( $R = 5$ m).....	24
Table 4.1. Parameters of the test fixture. ....	55
Table 4.2. Test samples and their characterised complex permittivity values.....	59
Table 4.3. Dielectric properties of each measurements for sample type 1. ....	62
Table 4.4. Dielectric properties of each measurements for sample type 5. ....	62
Table 5.1. Dimensions of one unit cell of the proposed EBG (unit: mm). ....	75
Table 5.2. Final dimensions of the CPW antenna (unit: mm).....	77
Table 5.3. Bandwidth comparison of the CPW antenna with and without the EBG. ....	80
Table 5.4. Realised gain of CPW antenna with and without EBG on human body (unit in dBi). .....	87
Table 6.1. Values for the parameters of the microstrip antenna (unit: mm). ....	93
Table 6.2. Electrical properties of body phantom at 38 GHz [114, 123]. ....	94
Table 6.3. Comparison between the results for free-space and on-body scenarios. ....	95
Table 6.4. The variation of $\epsilon_r$ of polyester substrate with temperature. ....	97
Table 6.5. The variation of $\epsilon_r$ of cotton fabric to RH levels. ....	99
Table 6.6. Measured and simulated resonant frequency of the antenna response to the ambient RH levels, and the measured weight under each humidity level. ....	104
Table A.1. Bill of materials.....	110

# Attestation of Authorship

I, Xiaoyou Lin, hereby declare that this submission is my own work and that, to the best of my knowledge and belief, it contains no material previously published or written by another person (except where explicitly defined in the acknowledgements), nor material which to a substantial extent has been submitted for the award of any other degree or diploma of a university or other institution of higher learning.

---

Signature

Xiaoyou Lin

20/ September/ 2018

---

Date

# Acknowledgement

First and foremost, I would like to express my sincere appreciation to my primary supervisor, Associate Professor Boon-Chong Seet. His guidance and support started from 2014 when I was still a Master student, and continued through all stages of this PhD study. I would like to thank him for giving me the confidence and encouraging me to overcome the difficulties and problems that we encountered in the past few years. He guided me with his valuable suggestions and kept me motivated at all times. It has been a great pleasure to work with him. His professional skills and the way that he analyses academic problems will be invaluable in my life. Without his contributions and endless efforts, there was no possibility for me to complete this thesis in three years.

Next, special thanks should go to my secondary supervisor, Associate Professor Frances Joseph, for her guidance and professional suggestions in the textile area, which is not my strong suit as an electrical engineering student. Her guidance has served me well. Furthermore, I also would like to thank her for securing the funding to purchase the required instruments and test facilities in this research.

I also would like to thank Associate Professor Chirn-Chye Boon and his VIRTUS Lab, at Nanyang Technological University (NTU), Singapore, for providing access to their facilities while I was there for one-month as a visiting research student.

Many thanks for the help from the AUT EEE technician group: Mr. Jian Huang for providing industrial fabrication suggestions for the test fixture and PCB boards, and helping with the installation of the new instruments; Mr. Justin Matulich and Mr. Brett Holden for assembling and optimising the test fixture used for material characterisation; Mr. Stephen Hartley for procuring the components and materials; as well as Kate Zizys, technician from the School of Art and Design, who has rendered much assistance on the screen-printing of fine conductive antenna patterns.

Besides, I would like to thank my following peers in the lab: Brandt Li for his help with measuring the antenna performance and setting up the test environment; Asim Anwar for sharing his expertise on MATLAB coding; and Jianchao Zhang for some general advice.

Furthermore, I would like to acknowledge the financial support from AUT: the tuition fee scholarship from the School and the stipend from the Engineering Research Institute (ERI), without which I will not be able to fully focus on my study.

Thanks to many friends whom I have met in New Zealand for their companionship and help to enjoy the life outside the research.

Finally, I would like to express my respect and thanks to my parents in China for their continued understanding and support. Without their everlasting love, this thesis would never have been completed.

# List of Acronyms

5G	Fifth-generation (cellular network)
ADC	Analogue-digital convertor
AMC	Artificial magnetic conductor
AUT	Antenna under test
BAN	Body area network
BW	Bandwidth
CPW	Coplanar waveguide
DAC	Digital-analogue convertor
DC	Direct current
EBG	Electromagnetic bandgap
EM	Electromagnetic field
E-textile	Electronic textile
FSS	Frequency selective surface
GND	Ground
GSM	Global systems for mobile communication
HFSS	High frequency structure simulator
HIS	High impedance surface
IL	Insertion loss
ISM	Industrial, scientific and medical (frequency band)
LNA	Low noise amplifier
LOS	Line of sight
MM-wave	Millimetre-wave

MMID	Millimetre-wave identification
MR	Moisture regain
MUT	Material under test
PA	Power amplifier
PCB	Printed circuit board
PEC	Perfect electric conductor
PMC	Perfect magnetic conductor
$Q$ -factor	Quality factor
RC	Reflection coefficient
R.H.	Relative humidity
RL	Return loss
RF	Radio frequency
RMS	Root mean square
SEM	Scanning electron microscope
SWR	Standing wave ratio
TC	Transmission coefficient
TDMA	Time division multiple access
TE mode	Transverse electric mode
TEM mode	Transverse electromagnetic mode
TL	Transmission line
TM mode	Transverse magnetic mode
UHF	Ultra high frequency
UTF	Universal test fixture
VHF	Very high frequency
VSWR	Voltage standing wave ratio

WCDMA	Wideband code division multiple access
WLAN	Wireless local area network
WSN	Wireless sensor network

# List of Symbols

$\alpha$	Attenuation constant
$\beta$	Phase constant; wave number; propagation constant for lossless dielectrics
$\gamma$	Complex propagation constant
$\epsilon$	Permittivity
$\epsilon_0$	Vacuum permittivity
$\epsilon_{eff}$	Effective relative permittivity, effective dielectric constant
$\epsilon_r$	Relative permittivity; dielectric constant
$\theta$	Elevation angle of radiation pattern
$\lambda$	Wavelength
$\lambda_0$	Wavelength in the vacuum
$\mu$	Permeability
$\sigma$	Conductivity
$\rho$	Resistivity
$\varphi$	Phase angle; azimuth angle of radiation pattern
$\omega$	Angular frequency
$\Gamma$	Reflection coefficient
$C$	Capacitance
$c$	Speed of light in vacuum = $2.998 \times 10^8$ m/s
dB	Decibels
dBd	Decibels relative to a dipole antenna
dB <sub>i</sub>	Decibels relative to a isotropic antenna
D <sub>tex</sub>	Grams per 10 kilometres of yarn
e.p.i	Ends per inch
$G$	Conductance
$G$	Antenna gain
$G_{re}$	Realised gain
gsm	Grams per square meter
Hz	Hertz

$k_0$	Wave number in the vacuum
$L$	Inductance
p.p.i	Picks per inch
$Q$	Quality factor
$R$	Resistance
[ $S$ ]	Scattering parameters
$T$	Transmission coefficients
[ $T$ ]	Scattering transfer parameters
$\tan\delta$	Loss tangent
$Z_0$	Characteristic impedance

# Chapter 1 Introduction

## 1.1. Overview

Smart textiles, also known as interactive textiles, refer to textile products that are embedded with miniature and flexible electronics to provide intelligent functions [1–2]. Smart textiles is a new and developing research area, which integrates advances from multiple disciplinary areas including textile science and fabrication, physical sensing and wireless communication. Consequently, research on smart textiles may encompass areas such as distributed biomedical wireless sensors, on-body channel characterisation and flexible wearable antennae. Smart-textiles have a wide range of military and civilian applications, typically deployed in the form of body area networks (BAN) for health monitoring, activity tracking and human-machine interfacing [3–9].

A BAN is a specialised wireless sensing network (WSN), which normally consists of physiological sensors, electronic circuits and wireless transmission units [10]. Electronic circuits are the controlling and data processing modules whereas the wireless transmission unit is used to communicate with external application users. As a bridge between on-body circuit boards and their external application users, flexible radio-frequency (RF) structures have gained much attention in recent years. These structures are based on flexible conductors such as metal foils, conductive textiles or nano-silver inks, and flexible dielectrics such as textile fabrics or thin plastic films, covering most RF components like transmission lines, antennae, high-impedance surfaces (HISs), and so on [11–14]. In particular, flexible antennae operating at microwave frequencies (0.3–30 GHz) have been extensively studied for both on- and off-body scenarios. The electrical properties of flexible conductive and dielectric (including textile) materials and their structural effect on RF performance have also been reported in previous literatures [15–20]. Furthermore, due to the crowded spectrum at microwave range, there are an increasing number of textile-based antennae currently being deployed for body-centric communication at millimetre-wave (mm-wave) frequencies to access wider bandwidth and achieve faster transmission rate than previous microwave systems [21–22].

In this context, this thesis focuses on investigating flexible and wearable RF structures operating at quasi-mm-wave and mm-wave frequencies from 20 to 40 GHz, covering the unlicensed industrial, scientific and medical (ISM) frequency band (24.5 GHz) [27], and

two candidate frequency bands (28 and 38 GHz) for future 5<sup>th</sup> Generation (5G) cellular network [47]. Specifically, the objectives of this thesis are to deliver:

- A novel hybrid-transmission-line method to characterise dielectric materials;
- A fractal design of flexible electromagnetic bandgap (EBG) to improve the performance of on-body antennae at mm-waves;
- Sensing antennae operating at 38 GHz for monitoring near-body environmental parameters (i.e. temperature and relative humidity).

## **1.2. Research Gaps, Motivations and Scope**

From the literature review, it has been found that there still exist a number of research gaps on introducing wearable antennae and other flexible RF structures for body-centric wireless communication systems over mm-wave frequencies:

- Unknown and unpredictable dielectric properties of textile fabrics due to a variety of available textile fabrication methods and complex fabric structures [19]. However, the requirements and procedures of characterising dielectric materials at mm-waves with existing methods are complex and demanding in terms of time and effort [15, 19];
- The performance of current on-body antennae at mm-wave bands is poor, such as having limited operating bandwidth and low antenna gain. Most existing methods to improve the performance of wearable antennae lead to either complex radiating patches or high-profile antennae [12, 21, 23, 27], which reduces the manufacturability and ease of use of wearable antennae; and
- In the current BAN systems, separate antennae and sensor modules are used for RF function and sensing, respectively. This follows the same structure of WSNs but the power consumption by the BAN nodes remains at a level similar to that of WSNs [1]. In order to further reduce the power consumption of the nodes, current methods have focused on developing new algorithms for physical and medium access control layers, such as the Time Division Multiple Access (TDMA) based strategy [10]. However, an alternative approach to solve this problem can be a design of passive units with combined sensing and communication functions, which, to the best of our knowledge, has not been proposed for BANs operating at mm-wave bands in previous literatures.

In terms of the motivations, first of all, a prior understanding of the substrate materials' dielectric properties is critical in designing mm-wave components since the dielectric deviations of the substrate materials can contribute to a significant frequency shift [25]. However, most substrate materials do not contain information about their dielectric properties above 10 GHz in their technical datasheet. Besides, dielectric materials used for RF applications are currently not limited to conventional rigid ceramic laminates (e.g. FR4, Rogers RT/d5880), but can include non-conventional flexible materials such as textile fabrics, many of which have no existing characterised dielectric values. Therefore, having a simple and fast method to characterise dielectric materials at mm-waves can significantly shorten the RF design cycle and minimise the frequency shift problem.

Secondly, there exist a number of flexible antennae designed for on- and off-body wireless communication at mm-waves, such as the end-fire antenna operating at 60 GHz [22] and the inkjet-printed Yagi-Uda antenna operating at 24.5 GHz [27]. However, these mm-wave wearable antennae suffer from either a high backward radiation gain ( $> 5$  dBi) that increases the radiation hazard to human users, or insufficiently wide bandwidth ( $< 20\%$ ). Therefore, there is a need to enhance their on-body performance to satisfy anticipated future requirements.

Finally, for deploying sensors in the near space around the human body, clothing is an obvious platform. However, unlike conventional rigid components, wearable applications require highly flexible sensors and antennae with structural integrity [26]. Flexible antennae have been extensively studied at both microwave and mm-wave frequencies due to their flexibility to conform on the human body and softness for comfortable wearing, and have been successfully used in various BANs for wireless communications (e.g. [8, 14, 21, 22, 24]). However, it is still an ongoing challenge to realise highly integrated, lightweight and ultra-low-power sensors for such wearable applications. A promising solution proposed in this thesis is to design sensing antennae by relating the dielectric material properties with modifiable RF characteristics due to external phenomena (e.g. temperature and humidity).

### **1.3. Contributions and Publications**

This thesis makes three primary contributions as follows:

- **A hybrid microstrip-line (ML) method** is firstly proposed for characterising unknown dielectric materials at mm-waves. In this new method, two error boxes are introduced to represent the impedance mismatch and discontinuities caused by signal path transitions between two different types of transmission lines. Therefore, unlike conventional covered- or two-transmission-line methods, the proposed method requires neither a perfect impedance match between the test fixture and the coaxial cables nor a high reproducibility of the transitions' RF characteristics. The proposed method was applied to characterise several different types of dielectric materials, including conventional high-frequency laminates and common fabric materials for on-body applications, using a single setup with an in-house designed universal test fixture in the 37–39 GHz range. The results show good agreement between the measured and known dielectric values.
- **A flexible EBG for mm-wave wearable antennae** is designed based on the characterised properties of dielectric materials. The unit cell of the EBG has a fractal design with self-similar window-like structure, which can be easily fabricated at millimetre-scale. The fabricated EBG is a 3×3 cell array laser-cut from adhesive copper foil on polyester fabric substrate. Results show that the gain and –10 dB bandwidth of a wearable coplanar waveguide (CPW) antenna backed by the proposed EBG are improved by 3 dB, and 40%, respectively, across the frequency range from 20 to 40 GHz. Backward radiation is also decreased by 15 dB, significantly reducing the potential health risk posed by the radiating antenna to the human wearer. Furthermore, on-body measurements show that the CPW-EBG antenna performance is not highly sensitive to human body proximity.
- **Body-worn environmental sensing antennae** operating at mm-waves are also proposed in this thesis. Firstly, the geometry of the proposed sensing antenna is presented and simulated to operate at 38 GHz, which is a candidate frequency for future 5<sup>th</sup> generation (5G) cellular networks. Next, two candidate substrate materials are selected and measured at different temperature and RH levels in the climate test chamber, and preliminary analysis is given for the measured result. Further, a humidity sensing antenna is fabricated on the cotton substrate. Both simulated and measured results show that the resonant frequency of the antenna has a relatively linear response to the RH and a sensing resolution of 26 MHz per 1% RH can be achieved.

This research has resulted in the following publications:

1. X. Lin, and B.-C. Seet, “Dielectric Characterization at Millimetre Waves with Hybrid Microstrip-line Method”, *IEEE Transactions on Instrumentation and Measurement*, vol. 66, no. 11, 2017.
2. X. Lin, B. -C. Seet, F. Joseph, and E. Li, “Flexible Fractal Electromagnetic Bandgap for Millimetre-Wave Wearable Antennas”, *IEEE Antennas and Wireless Propagation Letters*, vol. 17, no. 7, 2018.
3. X. Lin, B.-C. Seet, and F. Joseph, “Wireless Sensing Systems for Body Area Networks”, in O. A. Postolache, S. C. Mukhopadhyay, K. P. Jayasundera, & A. K. Swain (Eds.), *Sensors for Everyday Life: Healthcare Settings*, Springer, UK, 2017.
4. X. Lin, B.-C. Seet, and F. Joseph, “Accuracy of Dielectric Material Characterization at Millimetre-wave”, in Proceedings of IEEE 7th Asia-Pacific Conference on Antennas and Propagation, Auckland, New Zealand, August 2018.
5. X. Lin, B.-C. Seet, and F. Joseph, “Wearable Humidity Sensing Antenna for BAN Applications over 5G Networks”, in Proceedings of IEEE 19<sup>th</sup> Wireless and Microwave Technology Conference, Sand Key, FL, USA, April 2018.
6. X. Lin, B.-C. Seet, and F. Joseph, “Fabric Antenna with Body Temperature Sensing for BAN Applications over 5G Wireless Systems”, in Proceedings of IEEE 9<sup>th</sup> International Conference on Sensing Technology, Auckland, New Zealand, December 2015.

Other publications and co-authored papers from related projects undertaken:

7. X. Lin, and B.-C. Seet, “Battery-free Smart Sock for Abnormal Relative Plantar Pressure Monitoring”, *IEEE Transactions on Biomedical Circuits and Systems*, vol. 11, no. 2, 2017.
8. X. Lin, B.-C. Seet, and F. Joseph, “Fine-pitch Surface Component Mounting on Screen-printed Fabric Circuits”, *IET Electronics Letters*, vol. 52, no. 12, 2016.
9. X. Lin, and B.-C. Seet, “A Linear Wide-Range Textile Pressure Sensor Integrally Embedded in Regular Fabric”, *IEEE Sensors Journal*, vol. 15, no. 10, 2015.
10. E. Li, X. J. Li, B.-C. Seet, and X. Lin, “Flexible Ink-printable Wideband Log-periodic Dipole Array Antenna for 5G Applications”, in Proceedings of IEEE 7<sup>th</sup> Asia-Pacific Conference on Antennas and Propagation, Auckland, New Zealand, August 2018.

## **1.4. Thesis Organisation**

The thesis is organised as follows:

Chapter 2 provides an overview of three different areas: the systems operating at high frequency, smart textiles and body area network, and mm-waves technologies, which form a background of this research. In addition, the simulation environment and measurement facilities used for this work are presented in this chapter.

Chapter 3 reviews relevant research literature, including several characterisation methods for both dielectric and conductive operating at high frequency. Besides, the state-of-the-art design of EBGs are discussed. Finally, common working mechanisms of sensing antennae and their applications are briefly analysed.

Chapter 4 first proposes the hybrid microstrip-line method and the design of a fixture based on the proposed method. Next, the properties of several conventional rigid PCB and fabric materials are analysed with the proposed characterisation method. Finally, the measurement accuracy is also briefly discussed.

Chapter 5 investigates the design of a wideband flexible fractal EBG operating at mm-waves. Besides, this chapter also studies its application of working with a wearable coplanar waveguide antenna for both free space and on body scenarios.

Chapter 6 presents the design of body-worn environmental sensing antennae. Two types of fabric materials are selected and measured when they are subjected to different temperature and humidity levels. A microstrip antenna structure is adopted since it inherently features a relatively narrow bandwidth and a high quality-factor, which lead to a design sensitive to small variation in the substrate's dielectric constant. Finally, a humidity sensing antenna is fabricated and its performance is characterised in free space.

Chapter 7 concludes this thesis with a summary of the contributions and some discussion on future research directions.

# Chapter 2 Background

## 2.1. Introduction

Flexible RF devices have gained significant attention during the past few years due to their flexibility to conform to the body curvature, lightweight for ease of integration into everyday clothing, and low cost to fabricate with existing techniques [7–9].

Wireless channels are modelled based on Maxwell’s Equations but this theory gives relatively complex EM field solutions which are not necessarily required while analysing RF circuits. During the practical process, transmission line (TL) is the basic hardware element for any system operating at high frequency whereas network concept is used to handle many RF analysis and design problems [28]. It is important to first introduce some concepts and definitions of RF systems and the tools used to analyse high-frequency circuits in order to gain a better understanding of the remaining chapters.

So far, flexible antennae have been extensively used as the wireless interface of body area networks (BANs) for data transmission. On the other hand, BANs are increasingly being developed to communicate at mm-waves because they provide ultra-fast data rates and reduced size of constituting components such as antennae and filters [21, 22].

This chapter provides a fundamental background of the above three areas related with this research. Firstly, basic concepts of RF systems and several types of high-frequency structures relevant to this work are presented. Next, smart textiles technologies and mm-wave techniques will be covered. Finally, the simulation software and measurement facilities used for this work will be briefly introduced.

## 2.2. Theoretical Background of RF Systems

### 2.2.1. Transmission line

#### 2.2.1.1. Basic transmission line theory

Figure 2.1 is the lumped-element equivalent circuit of a transmission line (TL), where  $R$ ,  $L$ ,  $G$  and  $C$  are the series resistance, series inductance, shunt conductance and shunt

capacitance per unit length, respectively, of infinitesimal length  $\Delta z$ ;  $v(z, t)$  and  $i(z, t)$  are the time-dependent sinusoidal voltage and current, respectively, at the distance of  $z$ .

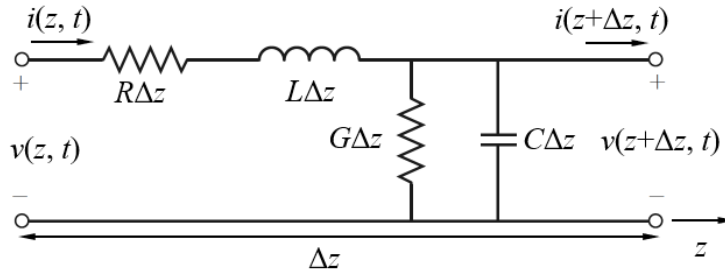


**Figure 2.1. Lumped-element equivalent circuit of a transmission line [28].**

The characteristic impedance of a TL ( $Z_0$ ) at high frequency is related by the magnitude of the voltage and current waves:

$$\frac{V_0^+}{I_0^+} = Z_0 = \frac{-V_0^-}{I_0^-} \quad (2.1)$$

where  $V_0^+$  and  $I_0^+$  are the voltage and current propagating along  $+z$  direction, respectively;  $V_0^-$  and  $I_0^-$  are the voltage and current propagating along  $-z$  direction, respectively.

The wave reflection occurs at the position where the impedance changes. This is shown in Figure 2.2, where one TL with characteristic impedance of  $Z_0$  is terminated by a load  $Z_L$  of different impedance. Due to the impedance discontinuity, only part of the incident energy will be delivered to the load, and the rest will be reflected back to the source.

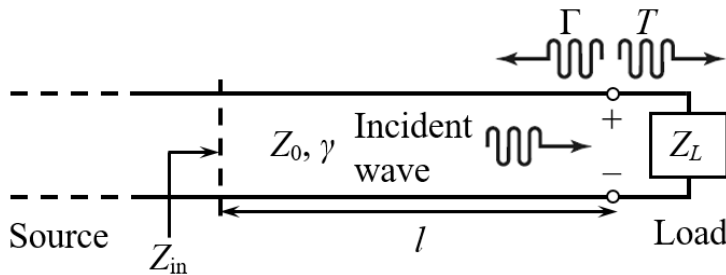


**Figure 2.2. Transmission and reflection coefficients [28].**

Therefore, the reflection coefficient (RC,  $\Gamma$ ) and the transmission coefficient (TC,  $T$ ) are defined as below:

$$\Gamma = \frac{Z_L - Z_0}{Z_L + Z_0} \quad (2.2a)$$

$$T = 1 + \Gamma = \frac{2Z_L}{Z_L + Z_0} \quad (2.2b)$$

Both  $\Gamma$  and  $T$  values in the unit interval  $[0, 1]$ , and can be expressed in decibel (dB) as return loss (RL) and insertion loss (IL), respectively:

$$\text{RL} = -20 \log(|\Gamma|) \text{ dB} \quad (2.3a)$$

$$\text{IL} = -20 \log(|T|) \text{ dB}. \quad (2.3b)$$

Furthermore, the input impedance ( $Z_{\text{in}}$ ), which describes the presented impedance of a terminated TL (e.g. TL loaded with antenna), as seen from a distance  $l$  away from the load (see Figure 2.2) is:

$$Z_{\text{in}} = Z_0 \frac{Z_L + jZ_0 \tan \beta l}{Z_0 + jZ_L \tan \beta l}. \quad (2.4)$$

This shows that  $Z_{\text{in}}$  is a function of both frequency (due to the phase constant  $\beta$ ) and  $l$ . Besides, it can be inferred from (2.3a) that in order to maximise the power delivered to the load (i.e. no power reflection), the value of  $Z_L$  should equal to that of  $Z_0$ , i.e.,  $Z_L = Z_0$ . Moreover, assuming that the load is an antenna,  $Z_L$  will be also generally a function of frequency due to the electrical geometry. Since the characteristic impedance of TL mainly depends on its geometry, designing a broadband antenna requires matching the impedance of the antenna with  $Z_0$  over a broad bandwidth with  $Z_0$ , and this is determined by a number of factors, including the antenna geometry, exciting methods, and so on.

#### 2.2.1.2. Transmission line types

In reality, TL has various types of forms such as coaxial cables and microstrip lines. This section will briefly introduce three types, namely stripline, coplanar waveguide (CPW) and microstrip line, and their properties at high frequency.

Stripline is a conductive planar line (centre conductor) sandwiched between two conductive plates (ground planes, GNDs). The space between the centre conductor and ground planes can be either air (dielectric constant  $\epsilon_r = 1$ ) or any other dielectrics with a certain  $\epsilon_r$  value. The geometry and the field distribution of a stripline are illustrated in Figure 2.3. A typical stripline is able to support TEM waves since the excited EM field is only contained within one type of dielectric material between the signal line and the GNDs.

Unlike stripline, both CPW and microstrip line can be etched with conventional printed circuit board (PCB) techniques. A CPW is typically constructed by two GNDs separated by a centre conductor. All these three conductors are on the same side of the substrate as shown in Figure 2.4(a), and thus the term *coplanar* is used. The impedance of CPW can

be tuned by adjusting the gap ( $g$ ) between the centre conductor and the GNDs, and the width of the centre conductor  $W$  [29].

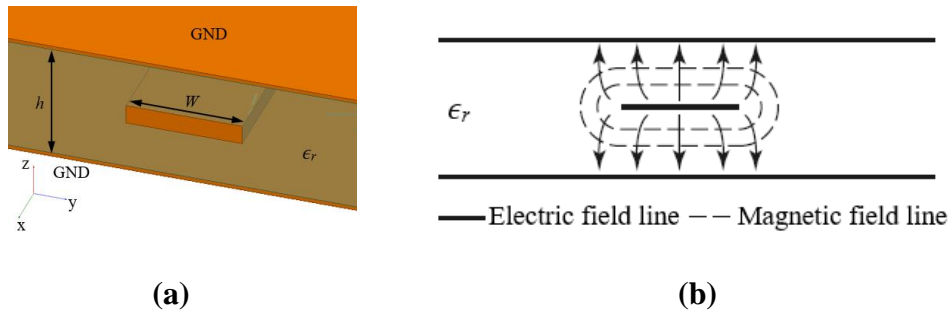


**Figure 2.3. Stripline: (a) geometry; (b) EM field distribution [28].**

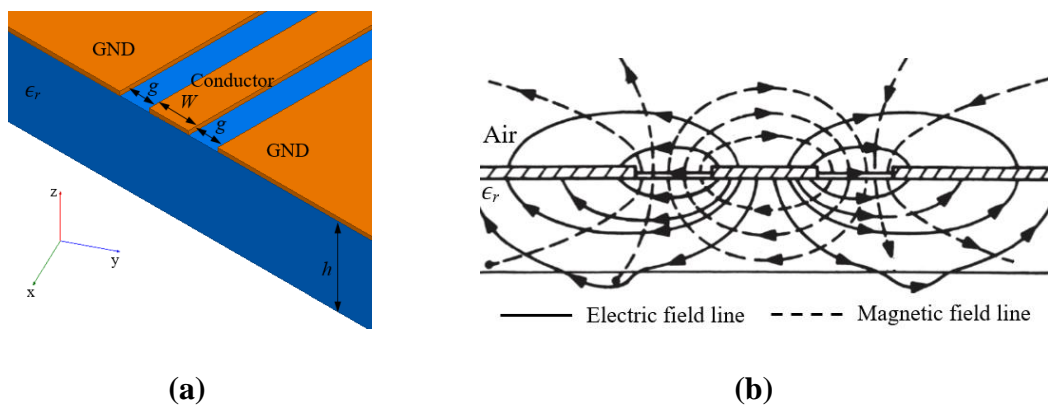


**Figure 2.4. CPW line: (a) geometry; (b) EM field distribution [29].**

On the other hand, a microstrip line has one strip line (signal trace) on one side of the substrate whereas its return conductor (GND) is on the other side of the substrate (see Figure 2.5(a)). As compared to CPW, a microstrip line has simpler structure but suffers from more loss at higher frequency (e.g. mm-waves) since the distance between the signal trace and GND is normally larger than that of CPW [28].

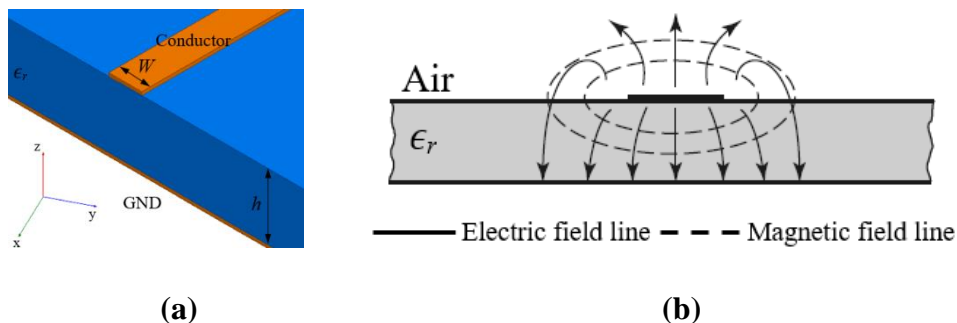


**Figure 2.5. Microstrip line: (a) geometry; (b) EM field distribution [28].**

Figure 2.4(b) and Figure 2.5(b) illustrate the EM field for CPW and microstrip line, respectively. It should be noted that for both types, the excited EM field exists not only

in the dielectric material but also in the air directly above. Therefore, both of them cannot support a pure TEM wave but a hybrid TM-TE mode wave that can be referred as quasi-TEM mode [28, 29]. For this reason, effective dielectric constant  $\epsilon_{eff}$  is used as the dielectric constant of a homogeneous material that equivalently replaces the air and dielectric regions of CPW and microstrip line.

Some important parameters of the above three types of TLs are summarised in Table 2.1, where  $k_0$  is the wave number in free space,  $W_e$  is the effective width of the signal conductor, and  $K()$  is the complete elliptic integral of the first kind [30].

**Table 2.1. Parameters of stripline, CPW and microstrip line.**

Parameters	Stripline	CPW	Microstrip line
$\epsilon_{eff}$	N.A.	$\frac{1}{2} + \frac{\epsilon_r - 1}{2} \frac{K(k')}{K(k)}$	$\frac{\epsilon_r + 1}{2} + \frac{\epsilon_r - 1}{2} \frac{1}{\sqrt{1 + \frac{12h}{W}}}$
$\beta$	$\sqrt{\epsilon_r} k_0$	$\sqrt{\epsilon_{eff}} k_0$	$\sqrt{\epsilon_{eff}} k_0$
$Z_0$	$\frac{30\pi}{\sqrt{\epsilon_r}} \frac{h}{W_e + 0.441h}$	$\frac{30\pi}{\sqrt{\epsilon_{eff}}} \frac{K(K')}{K(k)}$	$\frac{120\pi}{\sqrt{\epsilon_{eff}} \left[ \frac{W}{h} + 1.393 + 0.667 \ln \left( \frac{W}{h} + 1.444 \right) \right]}$

### 2.2.2. Two-port network and scattering parameters

Unlike Maxwell's equations that give EM field solutions for an RF system, two-port network analyses the same system from a circuit viewpoint. A typical two-port network consists of one black box and two terminal ports (see Figure 2.6(a)). Normally, port 1 is regarded as the input whereas port 2 is the output. RF properties of the circuit inside the black box can be expressed by a  $2 \times 2$  matrix such as Z- or Y-parameters. This thesis mainly focuses on the scattering-parameters, i.e. S-parameters or  $[S]$ , which are defined by the magnitude and phase of both incident and reflected signal waves.

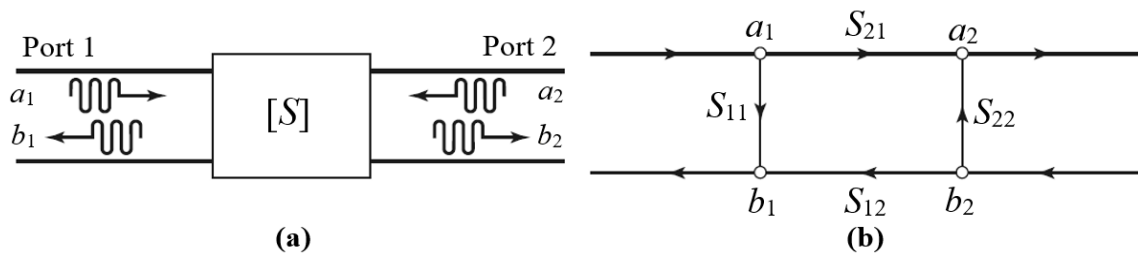


**Figure 2.6. Two-port network: (a) model; and (b) signal flow graph [28].**

As shown in Figure 2.6(a),  $a_1$  and  $a_2$  are the incident waves at Port 1 and Port 2, respectively, while  $b_1$  and  $b_2$  are their reflected waves. Then,  $[S]$  of this network can be defined as [28]:

$$\begin{pmatrix} b_1 \\ b_2 \end{pmatrix} = \begin{pmatrix} S_{11} & S_{12} \\ S_{21} & S_{22} \end{pmatrix} \begin{pmatrix} a_1 \\ a_2 \end{pmatrix}. \quad (2.5)$$

In (2.5),  $S_{11}$  and  $S_{22}$  are the RC whereas  $S_{12}$  and  $S_{21}$  are the TC. For a reciprocal and lossless network,  $S_{11} = S_{22}$  and  $S_{12} = S_{21}$ . Here  $S_{11}$  and  $S_{21}$  are used to illustrate their definition:

$$S_{11}(\text{dB}) = -20 \log \Gamma = -20 \log \frac{Z_{in} - Z_0}{Z_{in} + Z_0} \quad (2.6a)$$

$$S_{21}(\text{dB}) = -20 \log T = -20 \log \frac{2Z_{in}}{Z_{in} + Z_0}, \quad (2.6b)$$

where  $Z_{in}$  is the input impedance at port 1. In most systems including this work,  $Z_0$  is 50  $\Omega$  unless otherwise stated.  $S_{11}$  and  $S_{21}$  are of more interest since  $S_{11}$  is the RC of a one-port network (e.g. microstrip antennae), and  $S_{21}$  is the forward TC, which is useful when characterising materials' properties at high frequency.

One special case of the two-port network is when its ports are well matched with external circuits, and thus there are no reflection waves ( $S_{11} = S_{22} = 0$ ). Therefore:

$$S_{12} = S_{21} = e^{-\gamma l} \quad (2.7)$$

where  $\gamma = \alpha + j\beta$  is the complex propagation constant and  $l$  is the propagation distance.

Another useful matrix to analyse RF circuits is scattering-transfer-parameters ( $T$ -parameters or  $[T]$ ), which is closely related to  $[S]$ . The difference between them is that  $T$ -parameters is defined by the incident and reflected waves at each port:

$$\begin{pmatrix} b_1 \\ a_1 \end{pmatrix} = \begin{pmatrix} T_{11} & T_{12} \\ T_{21} & T_{22} \end{pmatrix} \begin{pmatrix} a_2 \\ b_2 \end{pmatrix}. \quad (2.8)$$

For a well-matched two-port network, its  $T$ -parameters can be expressed by:

$$[T] = \begin{bmatrix} e^{-\gamma l} & 0 \\ 0 & e^{\gamma l} \end{bmatrix}. \quad (2.9)$$

The advantage of using  $[T]$  is that it can easily describe a cascading system consisting of two or more networks by simply multiplying the associated individual  $T$ -parameters. For example, the  $T$ -parameters  $[T_T]$  of the cascading network shown in Figure 2.7 can be determined by:

$$[T_T] = [T_1][T_2][T_3] \cdots [T_n]. \quad (2.10)$$

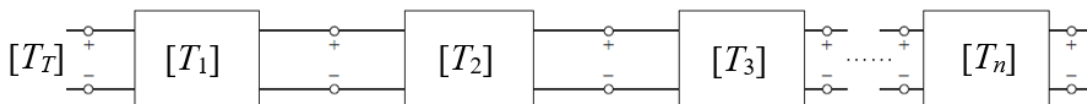


**Figure 2.7. Cascading network consisting of  $n$  networks.**

$[S]$  and  $[T]$  can be converted to each other using the equations in Table 2.2.

**Table 2.2. Conversion between  $[S]$  and  $[T]$ .**

	$T$		$S$
$S_{11}$	$\frac{T_{12}}{T_{22}}$	$T_{11}$	$-\frac{\det(S)}{S_{21}}$
$S_{12}$	$\frac{\det(T)}{T_{22}}$	$T_{12}$	$\frac{S_{11}}{S_{21}}$
$S_{21}$	$\frac{1}{T_{22}}$	$T_{21}$	$-\frac{S_{22}}{S_{21}}$
$S_{22}$	$\frac{-T_{21}}{T_{22}}$	$T_{22}$	$\frac{1}{S_{21}}$

## 2.3. Antennae and High-Impedance Surfaces

This section will first introduce microstrip and CPW antennae, followed by a discussion of several important parameters to evaluate the antennae' performance. Finally, the properties of the high-impedance surface (HIS) will be presented.

### 2.3.1. Antennae

#### 2.3.1.1. Microstrip and CPW antennae

The microstrip antenna is first introduced by Deschamps in 1953 [30]. It then received considerable attention from the 1970s due to its low profile, easy fabrication, compatibility with MMIC design and flexibility to conform to planar or non-planar surfaces.

Typically, a microstrip antenna consists of a radiation patch, a microstrip feed line, and an impedance tuning circuit. A variety of tuning circuits can be chosen including  $LC$  circuits, stub-tuning strip, or inserted slot tuning circuits [31]. When a suitable shape is selected, this type of antenna is able to achieve flexible tuneable impedance, resonant frequency and radiation patterns. However, it suffers from some disadvantages such as low efficiency, high  $Q$ -factor, and narrow operating bandwidth.

The geometry of a rectangular microstrip antenna with an inserted slot tuning design and its equivalent lumped-component circuit are illustrated in Figure 2.8(a) and (b), respectively, where  $Z_A$  stands for the impedance of the antenna.

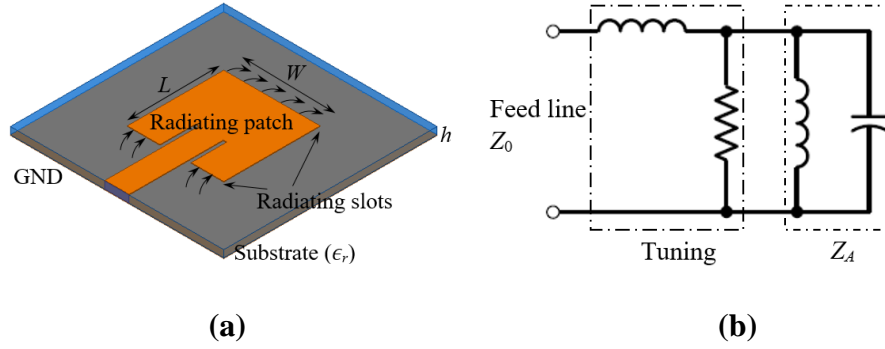


**Figure 2.8. Rectangular microstrip antenna: (a) geometry; (b) equivalent circuit.**

For designing an antenna patch with sufficiently high efficiency, its geometry should be of first consideration. The choice of a suitable substrate is another important factor. A thick substrate with low  $\epsilon_r$  leads to a high-efficiency, large bandwidth antenna but with large element size, and vice versa [31]. Formulae for calculating the theoretical dimension of a microstrip antenna are shown as follow:

$$W = \frac{c}{2f_0 \sqrt{\frac{\epsilon_r + 1}{2}}} \quad (2.11a)$$

$$L = \frac{c}{2f_0 \sqrt{\epsilon_{eff}}} - 2\Delta L \quad (2.11b)$$

$$\Delta L = 0.412h \left[ \frac{(\epsilon_{eff} + 0.3) \left( \frac{W}{h} + 0.264 \right)}{(\epsilon_{eff} - 0.258) \left( \frac{W}{h} + 0.8 \right)} \right] \quad (2.11c)$$

where  $f_0$  is the desired resonant frequency,  $c$  is the speed of the light,  $h$  is the thickness of the substrate,  $\Delta L$  is the extended length due to the fringing field,  $\epsilon_{eff}$  is the effective dielectric constant that can be obtained from Table 2.1,  $L$  and  $W$  are the length and width of the antenna, respectively.

The CPW antenna was proposed by Wen in 1969 [29]. It has a radiating patch design similar to that of a microstrip antenna. However, its ground plane is around the patch but not on the other side of the substrate as shown in Figure 2.9.

As mentioned previously, a CPW structure emits more EM field in the air between the patch and the GND, and less in the dielectric substrate as compared to the microstrip antennae. Therefore, CPW antennae incur less dielectric loss, which makes it more suited

for mm-wave applications. Besides, unlike microstrip antennae, which have major radiation towards one side of the antenna, the CPW antenna has a dipole-like radiation pattern that travels in the direction perpendicular to the radiating patch and along both sides of the antenna.

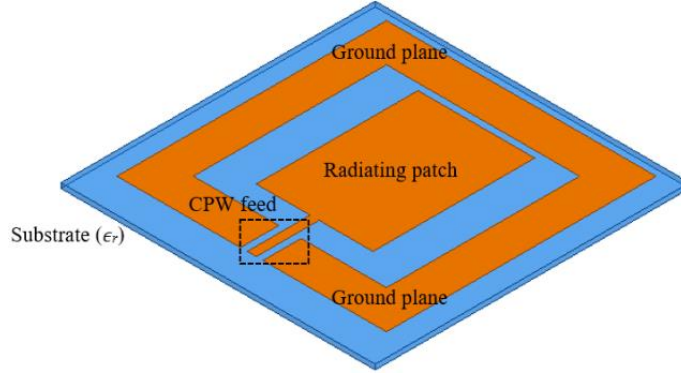


**Figure 2.9. Geometry of a coplanar waveguide antenna.**

### 2.3.1.2. Antenna's impedance, reflection coefficient and resonant frequency

One important parameter to evaluate the antenna performance is its impedance, which is a complex number, and the load impedance that the antenna presents to a connecting TL [31]. As mentioned previously, the ability of an antenna to accept power delivered from a source is determined by the presented load impedance of the antenna.

From (2.3a) and (2.4a), the RC of an antenna with certain input impedance can be calculated in decibel (dB). A lower RC magnitude indicates a better matching between the antenna and TL. To give reasonable performance, an antenna should have < 10% power reflection, which is equivalent to < -10 dB calculated RC. The frequency band(s) of an antenna with RC < -10 dB is considered as its *impedance bandwidth (BW)* or *operating BW*, where the minimum value point is its *resonant frequency (f<sub>0</sub>)*. Figure 2.10 shows the operating BW of a simple microstrip patch antenna resonating at 38 GHz.

Besides in absolute form, the operating BW of an antenna, or any RF system, can also be expressed in a relative form:

$$BW\% = 200\% \times \frac{f_H - f_L}{f_H + f_L} \quad (2.12)$$

where  $f_L$  and  $f_H$  are the low and high frequency points where -10 dB RC are observed (see Figure 2.10). Relative BW gives a normalised measure of how much frequency variation a system can handle. A system with over than 20% BW can be regarded as a wideband system [33].

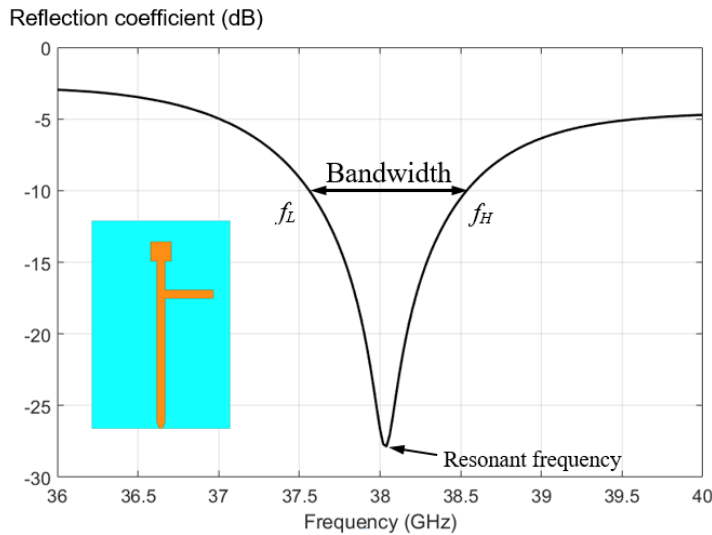


**Figure 2.10. Resonant frequency and bandwidth of a microstrip patch antenna.**

### 2.3.1.3. Antenna's radiation performance

Antennae are defined as metallic devices for radiating and receiving radio waves, and thus there exist a number of parameters to analyse antennae' radiation performance [31].

*Radiation pattern* or *antenna pattern* is a mathematical function or graphical representation of the radiation properties of the antenna as a function of space coordinates. There are near- and far-field regions around antennae but only far-field radiation is considered in most cases, which is because the angular distribution of an antenna is independent of the measuring distance from the antenna [32]. If the antenna under test has a maximal physical dimension  $L$ , then its far-field region is  $\frac{2L^2}{\lambda}$  away from the antenna, where  $\lambda$  is the wavelength of the operating frequency.

The radiation patterns of antennae can be described in 3D or 2D coordinates. Particularly, for a linearly polarised antenna, its radiation patterns can be plotted in E- and H- planes. E-plane is defined as the plane that contains the electric-field vector and the direction of maximum radiation, and the H-plane is perpendicular to the E-plane, which contains the magnitude-field vector and the direction of maximum radiation [33]. Figure 2.11 illustrates the antenna patterns of a dipole antenna in its 3D and 2D formats on both E- ( $xz$ -) and H- ( $yz$ -) planes.

Another important parameter related with antenna pattern is antenna gain, which describes the directive property of antenna. It is usually measured in dBi (decibels as referenced to an isotropic antenna element) or dBd (decibels as referenced to a dipole antenna element).

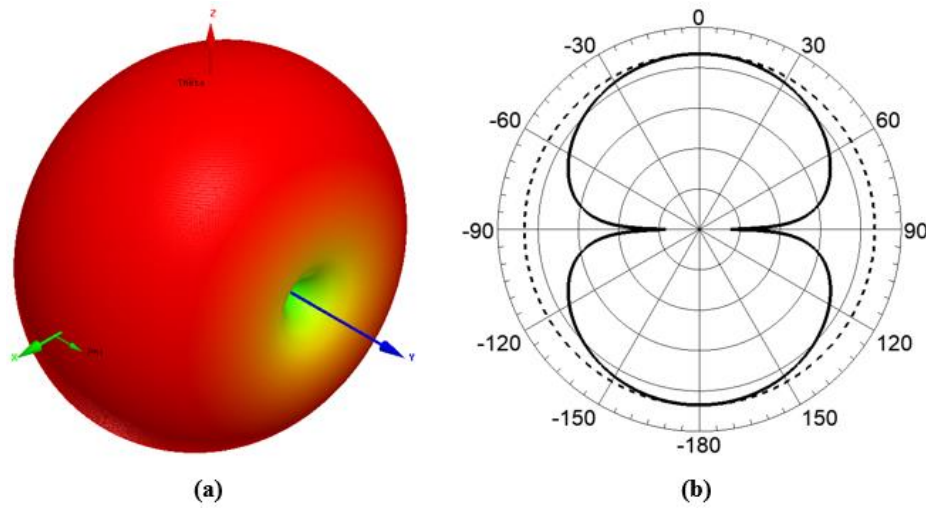


**Figure 2.11. Radiation pattern of a dipole antenna: (a) 3D pattern; (b) 2D pattern with E-plane (solid line) and H-plane (dash line).**

Relative gain which is used in most cases, is defined as the ratio of the power gain in a given direction to the power gain of a reference antenna in its referenced direction. The reference antenna is normally selected from an antenna, e.g. horn or dipole antenna, with known gain values. Besides, unless clearly stated, the gain is usually only measured in the direction of maximum direction [31, 32], which is the same in this work.

There are two gains defined: *gain* ( $G$ ) and *realised gain* ( $G_{re}$ ), where the latter takes into account of the reflection/mismatch losses [32]:

$$G_{re}(\theta, \varphi) = (1 - |\Gamma|^2)G(\theta, \varphi) \quad (2.13)$$

where  $\theta$  and  $\varphi$  are the elevation and azimuth angle, respectively.

Antenna pattern and gain is normally measured in open space, or in a RF anechoic chamber which can simulate an environment equivalent to open-space [31]. For the measurements in the chamber, the antenna under test (AUT) is mounted on a rotatable antenna positioner, which should be beyond the far-field boundary of the source antenna and in the quiet zone of the chamber. When the AUT is rotated, its received power from the source antenna is recorded at different  $\theta$  and  $\varphi$ , which are then mapped on either a 3D or 2D system to obtain radiation patterns.

The two-antenna method is employed for measuring the realised gain in this thesis. Briefly, there are two steps for the measurement. In the first step, the AUT is used as a receiving antenna and the received power ( $P_T$ ) in the maximum radiation direction is recorded. In the second step, an antenna with standard gain of  $G_S$  (e.g. horn) is used to

replace the AUT while all other settings (e.g. source power, distance between source and receiving antennae) are maintained as those in the first step. If the maximum received power in the second step is  $P_S$ , then the realised gain of AUT can be obtained by:

$$G_{re} = G_S + 10 \log \left( \frac{P_T}{P_S} \right) \quad (2.14)$$

### 2.3.2. High impedance surfaces

High impedance surfaces (HISs) are a metal-backed substrate fabricated with periodic conductive patches, which can exhibit surface wave bandgaps to prohibit the propagation of EM waves. A typical example of HIS is perfect magnetic conductor (PMC), which has a high surface impedance and small tangential magnetic field, even if the electric field is large. In reality, the PMC is realised in the form of artificial magnetic conductor (AMC) [33, 34].

Because of special boundary conditions, AMCs often act as high-impedance grounds for low-profile antennae to improve antenna radiating properties. There are two major advantages of using AMCs: in-phase reflection and EM wave suppression [34].

As illustrated in Figure 2.12(a), an antenna is placed far less than one operating wavelength ( $\ll \lambda$ ) above the AMC. Unlike a whole metal sheet that has an out-of-phase reflection, AMC reflects all the incident power in-phase. In other words, rather than destructive interference, the direction of the image current produces a constructive one, resulting a more effective radiation of the antenna.

Practically, electromagnetic bandgap (EBG) is the most common form of AMCs, which reflect the incident wave from  $+180^\circ$  to  $-180^\circ$  as illustrated in Figure 2.12(b). The useful bandwidth of the EBG is from  $+90^\circ$  to  $-90^\circ$ , where the magnitude of the surface impedance of the ENG will be greater than the impedance of free space ( $120\pi$ ). The response frequency crosses  $0^\circ$  and should be located at the desired frequency.

Besides, with periodic designs, AMC can prohibit the propagation of surface waves in certain frequency bands. Figure 2.13(a) illustrates a basic mushroom-like EBG with its configuration schematic and equivalent lumped-component model [35], which consists of a ground plane (GND), periodic metallic square patches, and a dielectric substrate with via connections. Its equivalent inductance  $L$ , capacitance  $C$  and resonant frequency are determined by:

$$C = \frac{W(\epsilon_0 + \epsilon_r)}{\pi} \cosh^{-1} \left( \frac{2W+g}{g} \right) \quad (2.15a)$$

$$L = \mu_0 h \quad (2.15b)$$

$$f_0 = \frac{1}{2\pi\sqrt{LC}} \quad (2.15c)$$

where  $W$  is the length of one conductive unit cell,  $g$  is the spacing between elements,  $h$  is the thickness of the substrate.

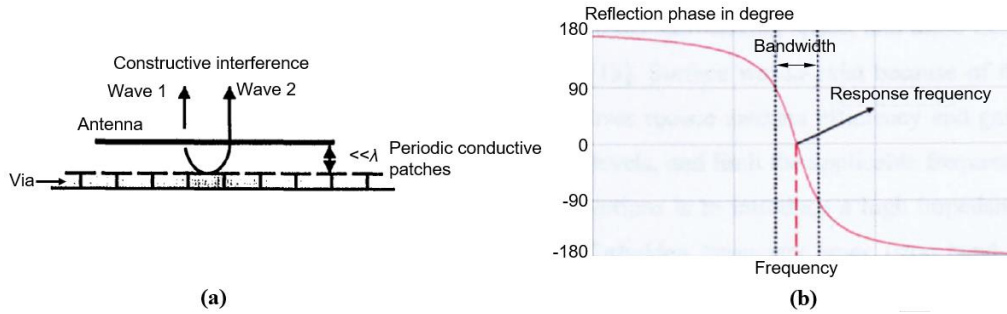


**Figure 2.12. (a) In-phase reflection of AMC; (b) reflection diagram of EBG [36].**

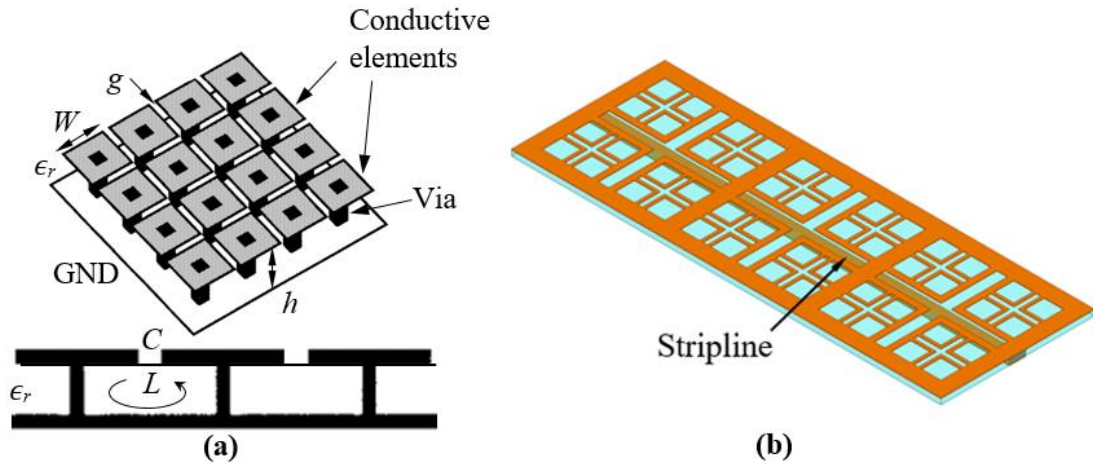


**Figure 2.13. (a) Mushroom-like EBG and its equivalent circuit [35]; (b) suspended stripline for measuring transmission coefficient.**

The mushroom-like EBG behaves as a network of parallel LC circuits, which acts as a 2D electric filter to block the flow of current along the sheet. As shown in Figure 2.13(b), EM wave suppression is commonly evaluated by the measured TC (e.g.  $S_{21}$ ) of suspended TL placed over the AMC/EBG surface [36]. Theoretically, the EM wave transmission within the bandgap of AMC/EBG should be blocked. Thus, the reduction of  $S_{21}$  at certain frequency bands can indicate the EM wave suppression bandgap of the AMC/EBG.

## 2.4. Smart Textiles and Body Area Networks

Smart textiles are defined as textile products such as woven, knitted or other rendered structures using fibres and yarns, which can sense or interact with the external

environmental conditions and/or stimuli in a predetermined way [37]. These external conduction and stimuli are regarded as trigger signals that may come from sources such as mechanical, thermal, chemical, and electrical signals.

Smart textiles, which are integrated with high levels of detection, response and intelligence, can be divided into three categories, namely passive, active and ultra-smart textiles [1, 38]. Passive smart textiles can only gain feedback from environmental or physical phenomena based on the information from sensors. Under this category, sensors (including conventional rigid and textile sensors) can be implemented to detect physiological parameters (e.g. EEG and respiratory rate), and environmental parameters (e.g. temperature and pressure) [1]. In addition, conductive yarns or fine metal wires can be integrated into fabric structures to replace regular conductive traces or cables in the circuit for connecting between sensors and other on- or off-body electronic devices [39].

Unlike passive smart textiles, active smart textiles are able to react to the sensed signals from the environment, integrating an actuator function and a sensing device. This means that different types of electronic components have been substituted by their textile equivalent. A few typical examples of active functionality include power generation and storage, wireless communication and RF functions, and human-machine interfaces [38]. The environmental sensing antennae developed in Chapter 6, which serve as both sensing element and wireless communication unit, fall within this category.

Finally, ultra-smart textiles, or very smart textiles, are able to sense, react and adapt their behaviour to particular circumstances. Here components such as logic boards and devices such as transistors can be realised using microelectronics and textile-based componentry within this category. Typically, applications under this category consist of a unit that works as a central unit, with cognition, reasoning and activating capacities [38]. The development of ultra-smart textiles requires a highly-integrated knowledge of a variety of sciences such as traditional textiles, material sciences, sensor and actuator technology, artificial intelligence, data processing algorithms, wireless communication, and biomedical sciences. [39].

Within the field of smart textiles, electronic devices or computers may be placed on or integrated with clothing items and accessories that can be comfortably worn by humans. Smart textiles can be more powerful than hand-held devices (e.g. smart phones or pads) since it can provide additional functions such as sensing and scanning features to provide biofeedback and physiological monitoring [37].

Smart textiles foresee the potential of future electronics to be an integral part of people's daily lives. Research on new textile fibres, flexible materials, advanced fabrication techniques and miniature electronic devices are accelerating the realisation of smart textiles [1, 38].

Various types of textile components have been reported thus far. These tend to be focused on three areas: *Fabric antennae* are used as the wireless interface bridging between the on-body components with external devices. Low-profile antennae are preferable for on-body applications since the coplanar structure ensures an easier integration between the antenna and daily clothes. Besides, to achieve good performance, fabric antennae need to be lightweight, robust to external environment and the rigours of daily use [11, 12]. Recently, a novel self-made conductive thread was manufactured by twisting 7 fine copper filaments together. This new thread was introduced to embroider a dipole antenna onto regular cotton textiles, whose performance is comparable to that of conventional copper antennae at microwave frequencies [40]. Similarly, a broad-band spiral dipole antenna was designed and embroidered on a cotton fabric with a commercialised silver-coated silver yarn for off-body wireless communications [41]. *Fabric connectors* provide reliable electrical connections between on-body components. It is easy to realise such connections directly with conductive threads. However, to suit special requirements for wearable applications, stretch-ability is required for fabric connectors, which can be realised with new stretchable conductive inks [42] and elasticised knitted structures [43]; *Fabric sensors* are the basic element for on-body networks, which are employed to monitor some vital physical parameters such as heart beat and blood pressure and to detect external environmental phenomena such as temperature and humidity. Many types of fabric sensors, including pressure sensors [44], strain sensors [45], and humidity sensors [46], have been reported and implemented for wearable applications.

In addition to the above types of textile components, there are more complex systems, including body area networks (BANs), which are specialised forms of small-scale wireless sensor networks (WSNs) operating near human bodies. This technology embodies the convergence of wearable, sensing, and wireless communication techniques, with a focus on health monitoring, human-machine interaction, and motion capturing applications [10]. Clothing is an ideal platform to embed developed sensor nodes near the human body, and thus smart textiles are particularly suitable for physiological and physical monitoring tasks.

A BAN is typically constructed of multiple intelligent sensors, which are attached to or implanted in the human bodies. Smart textiles are important enablers of BANs. However,

BANs can also interact with existing infrastructures and systems, such as cellular networks and WLAN at homes and hospitals. Body sensors provide data to a body aggregator (e.g. pad or smart phone), which is central to managing bodily events. A body aggregator performs several functions, including sensing, fusing data from body sensors, serving as a user interface, and bridging with external wireless network [47].

A wireless sensor node is the basic element in a BAN, consisting of sensors, signal processing circuits and wireless communication units [47, 48].

- Sensors are fundamental to all BANs and can be classified into three categories: *physiological* sensors are designed for monitoring vital body parameters such as blood pressure, electrocardiography (ECG) and body temperature; *biokinetic* sensors measure the acceleration and angular rate of rotation from human movement; and *ambient* sensors are used to measure environmental phenomena, such as temperature, humidity and light intensity. To get optimised performance of sensors such as high-quality data capture, proper placement of these sensors is required. Besides, sensors with low-energy consumption are preferred for BANs to provide long-term and continuous monitoring.
- Signal processing extracts valuable information from data collected from sensors, normally performed by processing algorithms executed on microprocessors. The extracted information is then fed to wireless communication units (i.e. antennae) for transmission to external devices and users.

The number of sensor nodes employed in one BAN typically ranges from 20 to 50 [10]. As illustrated in Figure 2.14, one node typically consists of an energy source, one or more sensors, a signal processor, and a communication transceiver. Some nodes may contain data storage units and support feedback control to body-based actuators such as an insulin pump or robotic prosthetic [47].

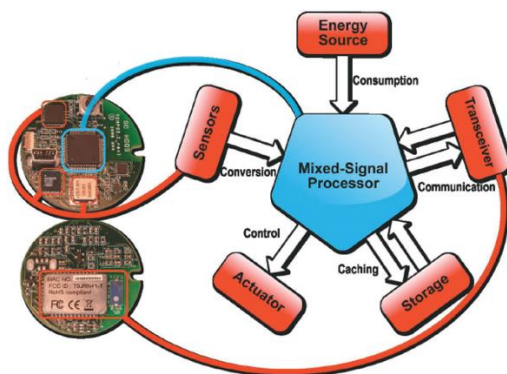


**Figure 2.14. Basic architecture of sensor nodes [47].**

## 2.5. Millimetre-wave Techniques

### 2.5.1. Millimetre-wave spectrum

Wireless communication is the tetherless transfer of information between two or more devices. The most common wireless technologies use radio waves, which are EM waves transmitted at *radio-frequency (RF)*, defined as the spectrum including very high frequency (VHF, 30–300 MHz), ultra-high frequency (UHF, 300–3000 MHz), super-high frequency (SHF, 3–30 GHz), and extremely high frequency (EHF, 30–300 GHz). The term *microwave* is typically used for referring to frequencies in the UHF and SHF bands, while the term *millimetre waves* (mm-waves) refers to frequencies in the EHF band where signals have an electrical wavelength  $\lambda$  between 1 and 10 mm. Figure 2.15 shows the breakdown of EM spectrum, ranging from medium frequency (300 kHz) up to F band (140 GHz).

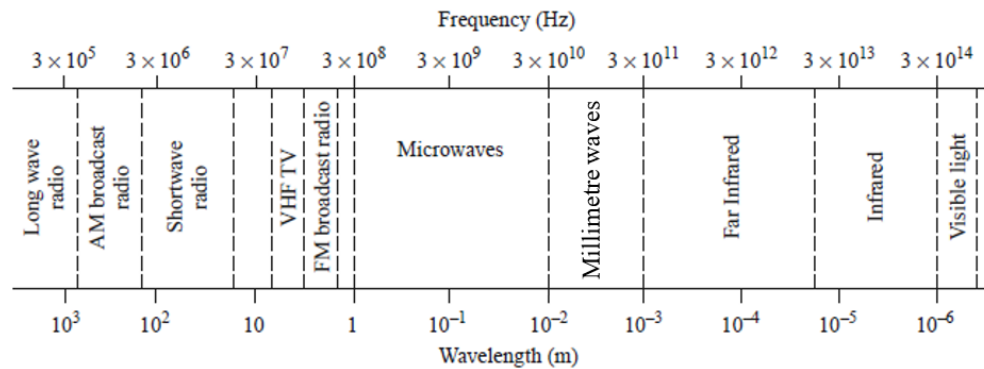


**Figure 2.15. Allocation of EM spectrum [28].**

Up to now, the majority of RF applications are wireless networks, security systems, radar systems, and medical systems. Limited by the manufacturing techniques, signal sources and other components, VHF and UHF bands have been extensively explored and developed for various RF communication systems, such as the global system for mobile communication (GSM), wideband code division multiple access (WCDMA) system, wireless local area network (WLAN) and Bluetooth (BT). However, due to the serious spectrum congestion below 20 GHz, quasi mm-wave and mm-wave frequencies have been proposed for future wireless communication in order to gain access to wider bandwidths and achieve faster data rates than previous microwave systems. The most attractive frequency bands above 20 GHz are: 1) 24.5 GHz, which is allocated for free industrial, scientific and medical (ISM) frequency band [27]; 2) 28 and 38 GHz, which are two candidate frequency bands of future 5th generation (5G) cellular network [49]; and 3) 60 GHz, which is a frequency band identified for unlicensed short-range

communication for future BANs [7, 21, 22]. Other useful bands include 35, 77, 140 and 220 GHz, to support various applications from security screening devices to short-range radar [50].

### 2.5.2. Wave propagation at mm-wave frequencies

Similar to all other propagating EM waves, the power of an mm-wave falls off as the square of the range. This is because of the spherical spreading of the radio waves as they propagate. There exist four mechanisms that will affect over-the-horizon propagation of signals: diffraction, reflection, refraction and transmission by means of surface waves [51]. In free space, the line-of-sight (LOS) propagation loss ( $L$ ) can be expressed by the following equation (measured in dB):

$$L = 20 \log \left( 4\pi \frac{R}{\lambda} \right) \quad (2.16)$$

where  $\lambda$  is the free-space wavelength of the signal frequency, and  $R$  is the LOS distance between the transmitting and receiving antennae. At mm-waves, this loss can be quite significant even for short distances. Table 2.3 lists the free-space path loss for different operating frequencies when the LOS distance  $R$  is 5 m. Therefore, it is recommended that mm-waves are most ideal for short-distance communication [51].

As high path loss exists at mm-waves, there is a need to push forward the design for achieving an acceptable system performance. One promising solution is to design antennae with medium to high realised gain (8–15 dBi) and architecture [21, 27].

**Table 2.3. Free-space loss for different operating frequencies ( $R = 5$  m).**

Application	Frequency (GHz)	$L$ (dB)
GSM	0.85	45
WCDMA	2.1	53
5G	38	78
BAN	60	82

### 2.5.3. Hardware architectures and devices

Figure 2.16 illustrates an architecture of direct conversion receiver and transmitter [52, 53]. On the receiver side, the signal is firstly filtered by a band-pass filter, followed by a low-noise amplifier (LNA). The processed signal is mixed in quadrature with cosine waves. The resulting waves are filtered by a low-pass filter to minimise the interference, and then amplified and sampled with an analogue-digital convertor (ADC). The signal

transmission involves mixing baseband signal with cosine or sine waves and amplifying the signal with a power amplifier (PA).

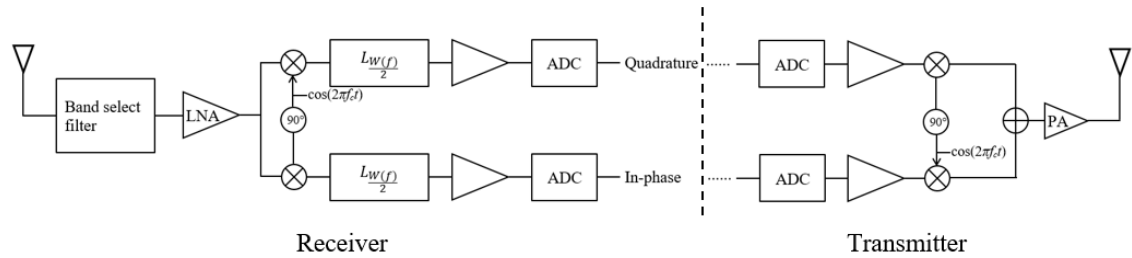


**Figure 2.16. Illustration of a direct conversion receiver and transmitter [52].**

As mentioned above, RF devices operating at mm-waves include passive components such as antennae and filters, and active devices such as ADC and amplifiers. One advantage of these devices is that their sizes can be made as many multiples of one wavelength and still can easily fit within a package or on a chip. However, medium to high gain is preferable for antennae and extremely low loss should be maintained for all devices to ensure that maximal power is delivered from the source to the load. One of the topics of this thesis will focus on the design of mm-wave antennae and the method of improving the designed antenna.

## 2.6. Simulation Environment and Measurement System

To facilitate the design and evaluation of the high-frequency structures proposed in this thesis, simulation tools and RF measurement equipment are used. Thus, it is essential to introduce the software environment used for the initial design and simulation, and the facilities for performance measurement of the fabricated structures.

### 2.6.1. Finite element method and ANSYS Electronics Desktop

The finite element method (FEM), or finite element analysis, is a numerical method for solving problems such as structural analysis, fluid flow and EM fields. FEM typically obtains solutions to boundary value problems through a series of partial differential equations. This method first divides the problem domain into a collection of subdomains (meshes), and then into a set of element equations for representing each subdomain. Thereafter, a systematic recombination of all subdomains into a global system of equations for the final calculation is performed. The global system of equations has known solution techniques and can be calculated from the initial values of the original problem to obtain a numerical answer [54].

Anslys’s High Frequency Structure Simulator (HFSS) is a well-known platform for EM circuit and system simulation. In HFSS, a 3D structure of the RF device is first created and then subdivided into smaller subsections. The finite element used by HFSS is called “tetrahedral”, and the collection of tetrahedral is called a “mesh”. Boundary conditions are then applied. Solutions are found for the EM fields within the finite elements and they are interrelated so that Maxwell Equations are satisfied across inter-element boundaries, yielding a field solution for the original structure. Finally, the generalised  $S$ -matrix solution is determined (see Figure 2.17).

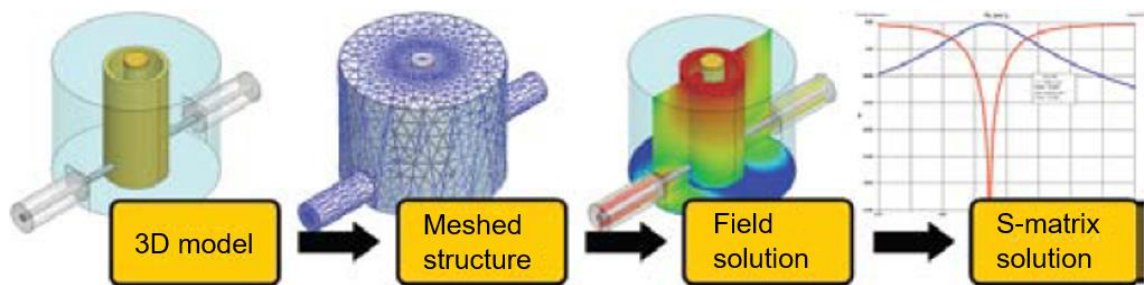


**Figure 2.17. FEM process in HFSS.**

### 2.6.2. Measurement facilities

For the fabricated prototypes of the designed structures, their performance must be examined and compared with the simulated results. In this work, three measurement facilities are mainly used: vector network analyser (VNA) for  $S$ -parameter measurement, anechoic chamber for obtaining radiation patterns, and a climate chamber for providing a controllable and stable environment when performing measurements under the impacts of different environmental conditions.

A portable Anritsu Site Master S820E with built-in VNA module is used for obtaining  $S$ -parameters. S820E has a wide operating frequency band from 1 MHz to 40 GHz, which is adequate for the RF structures designed in this work. For antenna measurements, the VNA can also serve as both transmitting source for the standard reference antenna and receiving terminal for the AUT.

Furthermore, an indoor RF anechoic chamber supplied by Holland Shielding Systems is employed to simulate an open space condition and controlled field environment (see Figure 2.18(a)). This chamber consists of a Faraday cage and RF absorbers that cover the inner walls, ground and ceiling of the cage, which is also able to minimise RF interferences from both outside and inside the chamber.

The test setup of the antenna positioning system inside the chamber for evaluating the far-field radiation of AUTs is illustrated in Figure 2.18(b), which consists of a linear polarised horn (WR28) with 15-dBi gain as the source antenna, and an antenna positioner that supports AUT rotating in both  $\theta$  and  $\varphi$  directions to complete full 360° scanning. The AUT resides in the quiet zone of the chamber. The measured TC will be recorded by S820E for plotting radiation patterns in MATLAB.

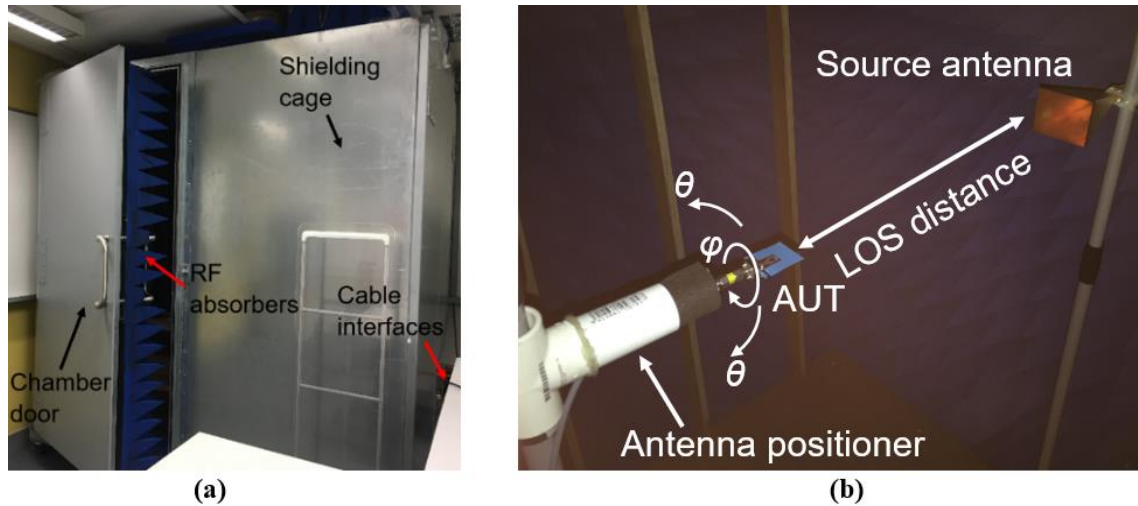


**Figure 2.18. (a) RF anechoic chamber; (b) antenna positioning system.**

Finally, a temperature and humidity controllable climate test chamber (Weiss WKL34) (see Figure 2.19) is used. This chamber is able to provide reproducible temperature and humidity environment, ranging from +10°C to +180°C and from 10% to 95% RH (temperature dependent), respectively. The maximal temperature and humidity deviation are  $\pm 5^\circ\text{C}$  and  $\pm 3\%$  R.H., respectively. A through hole exists on one side of chamber wall for cabling to be inserted into inner space for measurements.

Unless otherwise stated, all the dielectric characterisation measurements in this work are performed under room temperature ( $25 \pm 2^\circ\text{C}$ ) with  $50\% \pm 10\%$  humidity level.



**Figure 2.19. Climate test chamber (Model: WEISS WKL34).**

## **2.7. Summary**

This chapter presents the background on RF transmission systems, BAN and wearable technology, and mm-wave techniques, which are relevant to this research.

It also covers the simulation software and measurement facilities used to design and evaluate the performance of fabricated RF structures. The setup and procedure of measuring the antenna's radiation patterns are presented as well.

# Chapter 3 Literature Review

## 3.1. Introduction

This chapter presents an in-depth review of research literature relevant to this thesis.

Firstly, a number of methods that are used to characterise dielectrics and conductors at high frequency are discussed. While flexible dielectrics and soft conductors are newly developed materials, the theory of characterising their RF properties is the same as that used for conventional materials. Next, the designing of electromagnetic bandgap (EBG) operating at both classical microwave ( $<30$  GHz) and millimetre-wave (mm-wave,  $\geq 30$  GHz) are discussed. Finally, work on flexible sensing antennae and radio-frequency (RF) based flexible sensors for body area networks (BANs) is reviewed. Current flexible RF devices can be classified as either passive or active, with the majority being passive, meaning that they do not introduce power into their circuits. On the other hand, active devices such as RF amplifiers introduce and rely on power to operate in their circuits.

## 3.2. Material Characterisation at Radio Frequency

Future wearable applications may require radio-frequency (RF) circuits to be fully integrated into everyday textile clothing. Conventionally, materials used for RF circuits can be divided into two types: conductors with high conductivity for directing signals and electromagnetic (EM) waves, and dielectrics with poor conductivity acting as the medium of wave propagation. Recently, a number of studies have demonstrated that the majority of our everyday clothing could function as dielectrics at high frequency [11, 13, 18–19]. Furthermore, new techniques have been developed for high quality conductive textiles and inks with metallic particles [15–17, 26, 27]. These conductive materials have great potential to replace conventional metals (e.g. copper) for future wearable applications. Therefore, it is essential to know the EM properties of these new materials before designing and modelling textile RF circuits.

The electrical properties of both dielectrics and conductors are determined by their response to external EM fields [28]. This section will firstly introduce the parameters

describing these materials at high RF and review a number of methods that are used to characterise these parameters. Since magnetic materials are not considered in this thesis, permeability ( $\mu$ ) will not be discussed.

### 3.2.1. Dielectric material characterisation

#### 3.2.1.1. Dielectric materials

Dielectric materials are normally regarded as poor conductors, but as good media for electrostatic current flow. When EM waves are travelling inside dielectrics, the speed of propagation decreases as if the wavelength is shortened. The parameter used to measure how a material can bundle electric flux is permittivity ( $\epsilon$ ), which is a complex value and defined as [28]:

$$\epsilon = \epsilon' - j\epsilon'' = \epsilon_0 \left( \frac{\epsilon'}{\epsilon_0} - j \frac{\epsilon''}{\epsilon_0} \right) = \epsilon_0 (\epsilon_r - j \tan \delta) \quad (3.1)$$

where  $\epsilon_r = 8.85 \times 10^{-12}$  F/m is the permittivity in the vacuum;  $\epsilon_r$  is the relative permittivity of the dielectric material, or *dielectric constant* for most cases, and  $\tan \delta$  is *loss tangent* for describing the material's loss factor. For lossless dielectrics (e.g. vacuum),  $\tan \delta = 0$ . On the other hand, metals or good conductors have negative permittivity at RF, where no EM propagation exists [57].

As seen in (3.1), dielectric materials are defined by  $\epsilon_r$  and  $\tan \delta$ , and thus once these two parameters are identified, accurate design and simulation of RF circuits can be performed. It should be noted here that, both  $\epsilon_r$  and  $\tan \delta$  are physical parameters determined by the response of dielectric polarisation of a material to an electric field, regardless of the materials physical sizes such as length and thickness.

So far, various methods have been proposed to characterise the dielectrics, which can be generally classified as either non-resonant or resonant methods [58, 59]. Non-resonant methods mainly include reflection methods and transmission/reflection (T/R) methods. Basically, both types of methods derive the material's dielectric values by using information on the reflection of EM waves from and TC through the material under test (MUT). Non-resonant methods are useful when measuring dielectric properties over a wide frequency band and are suitable for materials with medium to high loss factors [59].

On the other hand, resonant methods determine materials' dielectric properties from the variation of measured resonant frequency and quality factor ( $Q$ -factor) of the resonator, which are due to the presence of the MUT. Resonant methods are more accurate than non-

resonant methods but have the drawback of being able to characterise materials' properties only at a single frequency or several discrete frequencies [57, 58].

In the following sub-sections, three widely used methods for characterising dielectric materials will be discussed, namely two-transmission-line (L-L) and covered-transmission-line (covered-TL) non-resonant methods, and resonator based resonant method, along with several related works on optimising their measurement accuracy. In this chapter, the term *transmission line* may refer to any TL type such as microstrip line, coaxial cables, and so on.

### 3.2.1.2. Two-transmission-line method

Two-transmission-line method (L-L method), which is illustrated in Figure 3.1, was first proposed by N. K. Das *et al.* [59]. Assuming two TLs with identical characteristic impedance ( $Z_0$ ) but different lengths, the long line is  $\Delta L$  longer than the short line.  $Z_0$  does not have to be  $50 \Omega$ , and is only determined by the geometry of the line and the dielectric constant ( $\epsilon_r$ ) of the dielectric material according to (2.1).

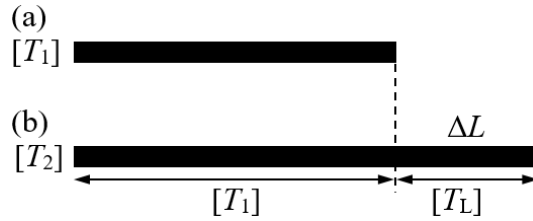


**Figure 3.1. Two-transmission line method: (a) short line; (b) long line.**

Here,  $[T_1]$  and  $[T_2]$  are the  $T$ -parameters of the short line and long line, respectively. According to the cascading property of  $T$ -parameters (2.10),  $[T_2]$  can be expressed as:

$$[T_2] = [T_L][T_1] \quad (3.2)$$

where  $[T_L]$  is the  $T$ -parameters of the lossy transmission line  $\Delta L$ . By multiplying  $[T_1]^{-1}$  at both sides of (3.2), we will have:

$$[T_L] = [T_2][T_1]^{-1} \quad (3.3)$$

Both  $[T_1]$  and  $[T_2]$  can be converted from their measured  $S$ -parameters, and  $[T_L]$  is solely determined by the complex propagation constant  $\gamma$ , or  $\beta$  if the system is lossless by applying (2.9). Once  $\gamma$  or  $\beta$  is obtained, the  $\epsilon_r$  (for TEM-supported TLs) or the  $\epsilon_{eff}$  (for quasi-TEM-supported TLs) is determined by  $(\beta/k_0)^2$ , where  $k_0$  is the wave number in free space. For a lossy dielectric, its  $\tan\delta$  is given by:

$$\tan \delta = \frac{2\alpha}{k} \quad (3.4a)$$

or

$$\tan \delta \approx 0.0366 \frac{\alpha \lambda_0 \sqrt{\epsilon_{eff}} (\epsilon_r - 1)}{\epsilon_r (\epsilon_{eff} - 1)}. \quad (3.4b)$$

Eqs. (3.4a) and (3.4b) are used for TEM- and quasi-TEM-supported TLs, respectively.

One factor that impacts the measurement accuracy is the difference of the electrical length between two TLs ( $\Delta L_e$ ), which could lead to an error as large as 40% [59]. One solution to this problem is to choose two lines with a significantly large  $\Delta L_e$  [19]. Another solution is measuring on TLs with multiple electrical length differences [60]. By implementing the electrical length correction algorithm, the resultant error can be reduced to 1.7%.

However, there still exist several other disadvantages of the L-L method when it is used in practical measurements. The major one is the poor result accuracy if the RF property (i.e.  $[S]$ ) of the transitions between the coaxial measuring cables to the TLs is not reproducible [59], which will lead to an inaccurate de-embedded  $[S]$  of the TLs.

Several methods have been proposed to remove the effect of transitions. In [62], an error cost function ( $e$ ) is introduced to process the measured data, which is defined as:

$$e = \frac{1}{n} \sum_{f_{start}}^{f_{stop}} \{ \|\text{Tr}([T_1][T_2^{-1}]) - \text{Tr}([T_2][T_1^{-1}])\| + \|\text{Tr}([T_1^{-1}][T_2]) - \text{Tr}([T_2^{-1}][T_1])\| \} \quad (3.5)$$

where  $n$  is the number of measured frequency points and  $\|\cdot\|$  is a suitable norm. Besides, at least 10 independent measurements are required for each line, and the error cost function has to be recalculated for each measurement. It is shown that this method can reduce the measurement error to 0.33%.

Regarding the characterisation of flexible dielectrics (e.g. fabrics), since the materials are too soft to support rigid connectors, it is a huge challenge to realise transitions with identical properties. Besides, the flexibility and compressibility of the substrates as well as their fabrication inaccuracies can result in significant variation of  $Z_0$ . Therefore, in [19], the pencil-matrix method is proposed to process the calculated  $\gamma$ . In short, all the aforementioned factors are considered as unknown noises distributions in the system, which can be used to write  $\gamma$  in a series of complex exponentials of noise-contaminated data as a function of frequency. By performing the matrix-pencil method, the resultant results show an error of 4% and 22% for  $\epsilon_r$  and  $\tan \delta$ , respectively, for fabric dielectrics.

### 3.2.1.3. Covered-transmission-line method

Covered-transmission-line (covered-TL) method is illustrated in Figure 3.2 [59]. Unlike the L-L method, the covered-TL method requires that the  $Z_0$  of TL equals to that of the measuring system, which is  $50 \Omega$  for most RF systems. Besides, the TL should be fabricated with a “standard” dielectric material, whose dielectric properties should have been measured precisely beforehand. This method derives the unknown dielectric properties from the variation of transmission coefficient (TC,  $T$ ) of the TL before and after being covered by the MUT.

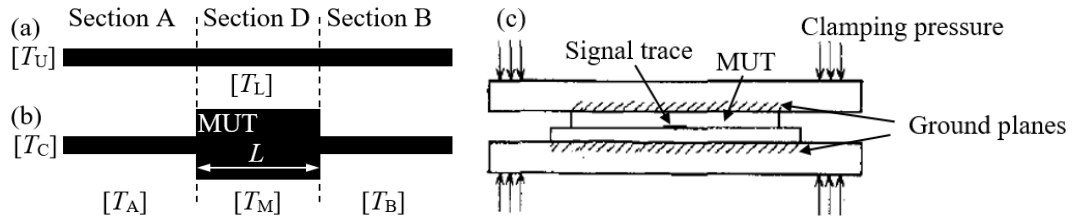


**Figure 3.2. Covered-transmission-line method: (a) uncovered TL; (b) covered TL and (c) side view of covered-TL method.**

There are two scenarios for the TL during the whole measurement: uncovered and covered as shown in Figure 3.2(a) and (b), respectively. In each scenario, the TL can be divided into three sections: section D, whose length  $L$  is the same as that of MUT, and is in-between section A ( $[T_A]$ ) and section B ( $[T_B]$ ). For the MUT, one side is free of copper but the other side should be well grounded.

For coplanar TLs (e.g. microstrip line), a clamper is normally used in order to avoid possible air gaps that may exist between the dielectric and conductive signal trace, and ensure the MUT is well-grounded [refer to Figure 3.2(c)].

By applying (2.10), the following can be obtained for the  $[T]$  of a cascading system for each scenario:

$$[T_U] = [T_A][T_L][T_B] \quad (3.6a)$$

and

$$[T_C] = [T_A][T_M][T_B] \quad (3.6b)$$

where  $[T_U]$ ,  $[T_C]$ ,  $[T_L]$  and  $[T_M]$  are the  $T$ -parameters of uncovered and covered TL, uncovered and covered section D, respectively. With sections A and B having the same length,  $[T_A] = [T_B] = [T]$ , which rewrites (3.6a) to:

$$[T_U] = [T][T_L][T]. \quad (3.7)$$

Then we will have the element  $T_{U22}$  of  $[T_U]$ :

$$T_{U22} = T_{22}^2 T_{L,22} + T_{L11} T_{21} T_{12} + T_{L21} T_{22} T_{12} + T_{L12} T_{21} T_{22}. \quad (3.8)$$

Given the relationships between  $T$ - and  $S$ -parameters in Table 2.1, and the fact that each section of the TL under both scenarios is reciprocal,  $S_{U21}$  can be obtained as:

$$S_{U21} = \frac{1}{T_{U,21}} = \frac{S_{L,12} S_{12}^2}{1 - 2S_{11} S_{L11} + S_{L11}^2 S_{11}^2 - S_{L12}^2 S_{11}^2}. \quad (3.9)$$

Similarly, the  $S_{C21}$  of the covered scenario is:

$$S_{C21} = \frac{1}{T_{C,21}} = \frac{S_{M12} S_{12}^2}{1 - 2S_{11} S_{M11} + S_{M11}^2 S_{11}^2 - S_{M12}^2 S_{11}^2}. \quad (3.10)$$

Dividing (3.10) by (3.9) [61]:

$$\frac{S_{C21}}{S_{U21}} = \frac{S_{M12}(1 - 2S_{11} S_{L11} + S_{L11}^2 S_{11}^2 - S_{L12}^2 S_{11}^2)}{S_{L12}(1 - 2S_{11} S_{M11} + S_{M11}^2 S_{11}^2 - S_{M12}^2 S_{11}^2)} = \Delta\alpha e^{-j\Delta\theta} \quad (3.11)$$

where  $\Delta\alpha$  and  $\Delta\theta$  are the variation of the measured magnitude and phase of  $S_{21}$ , respectively. By simulating the same covered-TL structure, and matching the measured  $\Delta\alpha$  and  $\Delta\theta$  with the simulated one, the dielectric property of the MUT can be derived.

There are three major factors that may affect the measurement accuracy of the covered-TL method. The first one is the same as the L-L method, which is due to the impedance mismatch of the RF transitions. Therefore, the same solutions used for the L-L method can be adapted for covered-TL method.

Secondly, a reasonable reflection coefficient (RC) is required for the whole measuring system. A poor RC value results in a narrow measurable range for both  $\epsilon_r$  and  $\tan\delta$ . For example, a test system with an RC of  $-10$  dB can only measure a material with  $\epsilon_r$  up to 8, but can be up to 16 if RC is  $-20$  dB [63]. This presents challenges to both problems of transition matching and TL fabrication, particularly at mm-waves.

Furthermore, the air gap between the TL and the MUT may also introduce errors, which is more serious for frequencies in the mm-wave range since the air significantly changes the EM field distribution, which in turn alters the calculated  $\epsilon_r$  of MUT. It is found that the slope of the simulated  $\epsilon_r$  over the frequency is a function of the air gap size [63]. Therefore, by matching the calculated  $\epsilon_r$  with the simulated one, the effect of the air gap can be largely removed.

For applications that are not using coplanar TLs, Taylor series expansion is proposed for processing (3.11) [64]. Then, the  $\epsilon_r$  and  $\tan\delta$  of the MUT can be found by applying the root-searching method. An error of 0.2% is observed for the measured  $\epsilon_r$ . However, this requires that the MUT should be as long as possible to minimise the error occurred at lower frequency band.

#### 3.2.1.4. Resonator method

The resonator method derives the  $\epsilon_r$  of dielectric materials from the measured resonant frequency ( $f_0$ ) and the  $Q$ -factor of a dielectric resonator with certain size. For this method, a certain type of resonator requires to be fabricated on the MUT.

In [58], a T-type resonator is proposed to determine the dielectric properties of the substrate material (see Figure 3.3(a)), which consists of a microstrip line and an open-ended stub (resonator arm). This resonator resonates at odd integer multiples of its quarter wavelength frequency. A universal test fixture (UTF) is normally used to provide a perfect impedance match for the transitions between coaxial cables from instruments and the on-board microstrip line as illustrated in Figure 3.3(b).

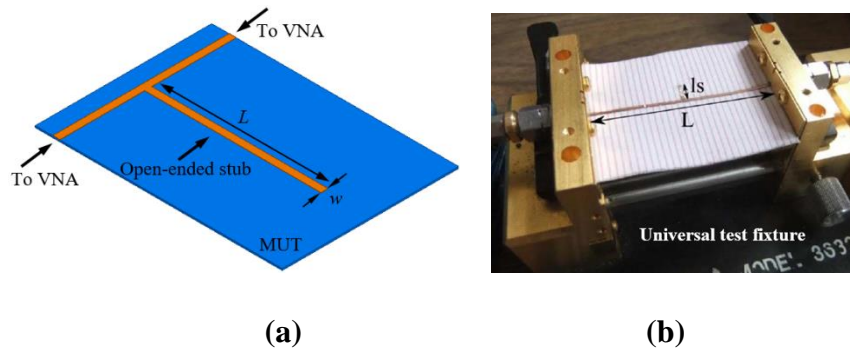


**Figure 3.3. Resonator method: (a) model; (b) measured by a UTF.**

The length  $L$  of the open-ended stub measures a quarter wavelength, which can be determined by:

$$L = \frac{nc}{4f_0\sqrt{\epsilon_{eff}}} \quad (n = 1, 3, 5 \dots) \quad (3.12)$$

where  $n$  is the order of the resonance. The effective dielectric constant  $\epsilon_{eff}$  however needs to be estimated as priori. Equation (3.12) can be used to calculate the actual  $\epsilon_r$  of the substrate based on the measured  $f_0$ . However, to achieve better accuracy, the fringing field effect from the T-junction and open-ended strip needs to be considered:

$$\epsilon_{eff} = \left[ \frac{nc}{4\left(L+\frac{w}{2}+L_{eo}-d\right)f(n)} \right] \quad (3.13)$$

where  $L$  is the physical length of the resonator arm,  $w$  is the width of the microstrip line,  $L_{eo}$  and  $d$  are correction factors for the effects of the open end, and the T-junction, respectively. The actual dielectric constant value  $\epsilon_r$  is calculated from the measured effective dielectric constant  $\epsilon_{eff}$  obtained from (3.13).

The loss of the MUT can be derived from the  $Q$ -factor. The unloaded  $Q$  ( $Q_0$ ) of the resonator can be determined by:

$$Q_0 = \frac{Q_L}{\sqrt{1-2 \times 10^{-(L_A/10)}}} = \frac{f_0}{BW_{3dB} \sqrt{1-2 \times 10^{-(L_A/10)}}} \quad (3.14)$$

where  $Q_L$  is the loaded  $Q$ -factor that is calculated from the resonant frequency  $f_0$  and the 3-dB bandwidth of the resonance.  $L_A$  is the value of insertion loss at the resonance. The  $Q_0$  consists of the loss from dielectric ( $Q_d$ ), conductor ( $Q_c$ ) and radiation ( $Q_r$ ):

$$\frac{1}{Q_0} = \frac{1}{Q_d} + \frac{1}{Q_c} + \frac{1}{Q_r} \quad (3.15)$$

$Q_c$  and  $Q_r$  can be easily calculated from existing equations designed for T-junction resonators with a given geometry. Therefore, the loss tangent  $\tan\delta$  of the MUT can be obtained from:

$$\tan \delta = \frac{\epsilon_{eff}(\epsilon_r-1)}{Q_d \epsilon_r (\epsilon_{eff}-1)}. \quad (3.16)$$

It should be mentioned here that other types of resonators can be used, such as in [18] where the authors used patch antennae to determine the MUT's dielectric constant. In this case, the above formulae should be replaced by (2.11) for calculating the size of patch antennae based on the material's  $\epsilon_r$ . However, the derivation procedure will be similar as above. The error of the characterised dielectric constant can be reduced to 4.2% without using any post-process procedure, which is significantly lower than the 40% of the L-L method if no data optimisation is implemented.

### 3.2.2. Conductive material characterisation

#### 3.2.2.1. Conductive materials

In RF circuits, conductive materials are used for directing the propagation of EM waves. The parameter used to measure conductors is conductivity ( $\sigma$ ), which is defined by the ratio of the current density to the electric field strength. It is specified in Siemens per

meter (S/m), which is also defined as the inverted resistivity ( $\rho$ ,  $\Omega \cdot \text{m}$ ). If considering perfect conductors (i.e.  $\sigma = \infty$ ), all EM fields will only exist beyond the surface of conductors and within the dielectric medium. However, real conductors exhibit a certain amount of resistivity, which results in conductor loss ( $P_{lc}$ ) defined as the integration of current flow over conductor's surface area ( $S$ ) as follows [28]:

$$P_{lc} = \frac{R_s}{2} \int_s |\vec{J}_s|^2 ds \quad (3.17)$$

where  $R_s$  is the surface resistance of conductor, which is defined as a two-dimensional resistance of a thin film regardless of the thickness, and  $\vec{J}_s$  is the surface current density.

Unlike in direct current (DC) mode, the skin effect becomes more significant with increasing operating frequency, thereby enlarging the effective RF resistance ( $R_{rf}$ ) and causing more energy loss. The relationships among  $R_s$ ,  $R_{rf}$  and surface depth  $\delta$  (due to skin effect) are:

$$R_s = \frac{1}{\sigma\delta} = \sqrt{\frac{\omega\mu_0}{2\sigma}} \quad (3.18a)$$

$$R_{rf} = \frac{L}{\sigma P\delta} = \frac{L}{P} R_s \quad (3.18b)$$

where  $\mu_0 = 1.257 \times 10^{-6}$  is the vacuum permeability,  $L$  is the length of the conductor with uniformly distributed current flow, and  $P$  is the physical length of the cross section. The total power loss in the conductor can be derived from (3.17) and (3.18). Therefore, it is suggested that the thickness of the conducting layer should be larger than the skin depth to minimise conductor loss.

### 3.2.2.2. Conductive material characterisation

Obviously, a higher DC conductivity indicates a lower RF conductor loss. However, to better understand the unknown electrical properties of conductive materials (MUT), the simplest way is to measure  $S_{21}$  of a TL structure whose signal trace is rendered by the MUT [17]:

$$R_{rf} = \frac{2Z_0 S_{21}(\text{dB})}{20L \log e} = \frac{Z_0 S_{21}(\text{dB})}{4.343L} \quad (3.19)$$

where  $L$  is physical length of the TL. Therefore, knowing the precise value of  $Z_0$  is critical when determining  $R_{rf}$ , which can be measured by oscilloscopes equipped with time-domain reflectometry (TDR) function [65].

The resonator method is another option for characterising conductive materials [66–69]. As shown in Figure 3.4, the MUT is fabricated as a short microstrip line, and placed between two open-ended microstrip stubs to form a resonator operating at the frequency of interest ( $f_0$ ). The width of both microstrip stub and MUT are well controlled according to the  $\epsilon_r$  of the substrate such that their  $Z_0$  is  $50 \Omega$ .

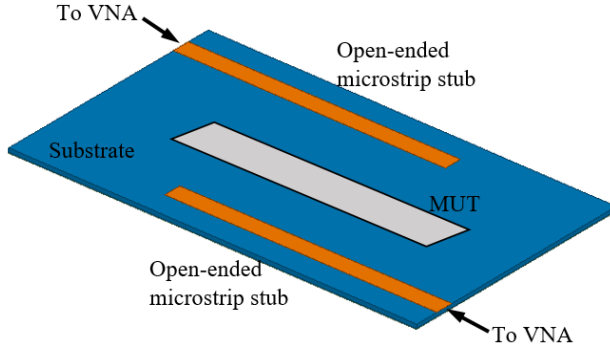


**Figure 3.4. Microstrip resonator.**

The  $Q_L$  and the magnitude of  $S_{21}$  of the resonator with MUT at resonance can be measured, and the  $Q_0$  can then be calculated from [66, 67]:

$$Q_0 = \frac{Q_L}{1 - |S_{21}|} \quad (3.20a)$$

which can be used to derive the loss factor ( $\alpha$ ) of the MUT at the desired resonant frequency [68]:

$$\alpha = \frac{8.686\pi f_0 \sqrt{\epsilon_{eff}}}{cQ_0} \quad (3.20b)$$

### 3.3. Electromagnetic Bandgaps

As described in Chapter 2, electromagnetic bandgap (EBG) is one realisable form of PMC/AMC, which can prohibit EM wave propagation within a certain frequency band. EBG is normally constructed by repeatable individual elements fabricated on a metal-backed substrate. The surface with periodic patterns can also be used alone in free space as frequency selective surface (FSS) [70, 71].

#### 3.3.1. Significance of using EBG

Due to the in-phase reflection property, the EBG can improve the radiation efficiency of the antennae placed close to it [72]. Another advantage of EBG is its ability to suppress surface wave, which exists at the interface between two different materials in the form of

surface currents. The surface wave is generated due to the finite size of antennae, which can significantly alter their performance, such as reduced gain, increased cross-polarisation and limited bandwidth [34, 35]. However, surface waves cannot propagate along EBG surfaces, and thus antennae that use EBGs as GNDs normally have better radiation performance or enhanced operating bandwidth [73, 74].

Furthermore, when working with coplanar structures (e.g. patch antennae or power dividers), EBG can block the propagation of high-order harmonic waves [75]. Particularly in wearable applications, EBG can significantly reduce antennae's backward radiation. Besides, with its wave guiding property, the radiation along a certain direction can be improved, which results in an enhanced gain [76].

### 3.3.2. Typical EBG structures

A variety of EBG structures have been proposed. One class of EBGs is known as mushroom-like EBG [34], which are constructed in 3D structures. This type of EBGs has a lattice of metal plate connected to the GND with conductive via holes through the substrates. Via connections create inductance effect whereas the gap between each periodic pattern contributes capacitance in the LC circuit. The detailed working mechanism of this type was presented in Section 2.3.1.4. Therefore, by adjusting the size and shape of periodic patterns, and the gap between patterns, the designed EBG can resonate at the desired frequency band [76–78].

On the other hand, EBG structures without via connections are classified as uniplanar-compact EBG (UC-EBG) [79], these have become attractive recently due to their advantages of low manufacturing cost and compatibility with standard planar circuits. A simple UC-EBG structure with periodic square pads is illustrated in Figure 3.5. The narrow strips connecting individual cell units are used as inductive elements and the gap between two cells contributes series capacitive coupling. The series reactance elements together with the shunt capacitance determine the operating frequency of the EBG.

Recently, more RF applications are required to operate at multiple frequency bands, and thus several EBG structures have been investigated to have a relatively wide band-stop frequency band. In [80], the author proposed an FSS design with multiple-concentric square patches for individual periodic cells, whose resonance and the number of resonant frequencies can be controlled by the slot openings on the square patch. This design has been successfully adapted as an EBG ground to optimise antenna's  $S_{11}$  and radiation performance [81, 82] for Wi-Fi applications.

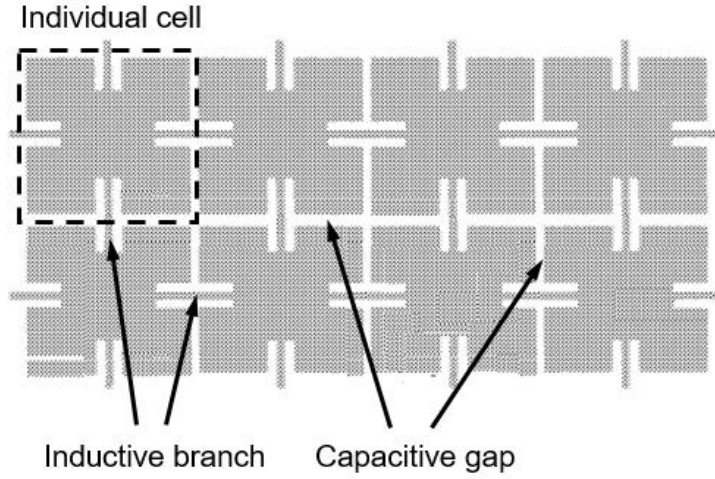


**Figure 3.5. UC-EBG structure with periodic square pads [79].**

Fractal geometries are now becoming popular in the antenna and EBG design since it enables the creation of smaller structures for the frequency of interest, and an increased operating BW. The term *fractal* was firstly proposed by Mandelbrot to characterise a set of complicated shapes that own inherent self-similarity and space-filling properties in their geometrical structure [83]. In [84], simple sub-division of the square patch is applied with multiple iterations. The simulation shows excellent wave suppression on dual frequency bands, which is useful in reducing the mutual coupling between antennae.

To achieve a wider bandwidth, H-shaped slots with different sizes are proposed to be alternately organised into a symmetrical cell, and the achieved bandwidth is 105.4% [85]. In [86], a fractal EBG based on Moore space-filling geometry is studied. Because Moore curve is aimed at filling a given area with a continuous line, this design inherently behaves like a strip with long electrical length (see Figure 3.6). The measured results show an ultra-wide bandwidth of 123% with a relative compact design. This design has been successfully implemented for both improving antenna's  $S_{11}$  [86] and reducing mutual coupling in the antenna array [87].

For an EBG cell with fractal design, its property is still determined by parallel  $LC$  circuits [85]. The  $f_0$  of one EBG cell and its outer dimension is related by [88]:

$$f_0 = \frac{c}{\lambda_0 \sqrt{\frac{\epsilon_{eff}}{2}}} \quad (3.21a)$$

$$\lambda_{EBG} = \frac{\lambda_0}{2} \quad (3.22b)$$

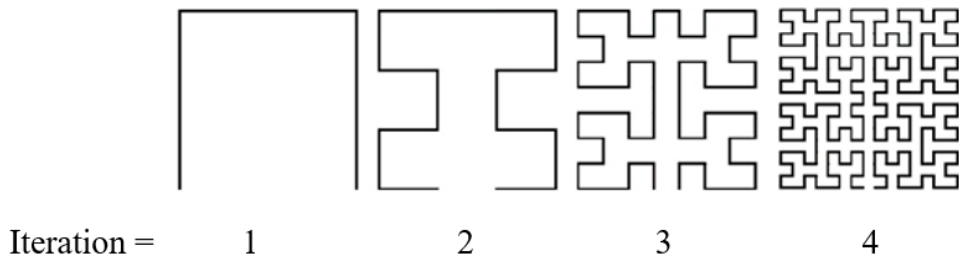


**Figure 3.6. Moore space-filling geometry with different iterations.**

where  $\lambda_0$  and  $\lambda_{\text{EBG}}$  are the wavelength at resonance and the periodic dimension of the metallic component, respectively.

EBGs operating at mm-waves also follow the above RF principles and structure designs. For example, both the UC-EBG structures presented in [89] and [90] similarly utilise the design in [79], with the only difference being their operating frequencies are shifted to 60 GHz and 28 GHz, respectively.

### 3.3.3. Fabric EBG structures

There also exist EBGs that are flexible or designed to work near human body. In [91], a square loop array is screen-printed and woven onto the polyester and cotton fabric, respectively. In [13], a surface smooth paste is applied onto the rough surface of cotton fabric, and thus the same loop array as [91] can be printed on cotton. The measured results in both works demonstrate that the woven or printed prototypes can achieve a relatively low TC at the desired frequency band.

The dual-band fabric EBG proposed in [81, 82] is designed for enhancing the antenna's radiation performance for on-body communications. The conductive patterns are cut from high-conductive fabric "Zelt", and then attached to flexible felt with a low dielectric constant. The free-space measurement shows that the EBG can significantly reduce the backward radiation by at least 12 dB, and improve the antenna gain by 3 dB. The EBG's performance is also robust when it is being attached to human body with curved surfaces, and only slight changes in both  $S_{11}$  and radiation patterns are observed. However, the EBG narrows the operating bandwidth of the antenna.

Due to the limited space for placing on-body devices, another pure-textile EBG design with compact geometry is presented in [92] for operating at ISM 2.4 GHz. The special T-shaped strips introduce more inductance into the design [91], and while the size of its EBG cell can be significantly reduced to  $0.47\lambda$ , its free-space and on-body performances remain similar to those presented in [81] and [82].

In addition to attaching the individual conductive patches to the substrates, the periodic patterns can be integrated into regular fabrics during the fabrication process. In [93], an inductive FSS was fabricated on a knitted polyester fabric. Similarly, an HIS pattern was knitted in [94] as a spacer fabric with commercialised conductive yarns on a flatbed knitting machine. This developed knitting process, which moves the conductive yarn from the back layer to the front, so that conductive via holes can be realised on the finalised textile HIS within the structure of spacer fabrics. However, this technique requires a special flatbed knitting machine, which is bulky and expensive. More importantly, knitting is not suitable for fabricating structures operating at mm-wave bands, because knitted fabrics are elastic, which will lead to a significant frequency shift.

The fabrication becomes more complex with an increasing frequency because the fabric is compressive, and the sizes of fibre are also in the same order of the ordinary textile fabrication accuracy of around 0.2–0.5 mm [11]. So far there is very limited literature on the performance of textile or wearable EBGs operating at mm-waves [95, 96], and thus this area of research is still in its infancy.

### **3.4. Wireless Sensing Antennae**

As stated in Section 2.4, there is limited space for wearable devices such as sensors and antennae to be deployed for on-body applications. Therefore, there is a need to realise highly integrated, lightweight and ultra-low-power sensors for BANs [10]. One promising solution is to integrate both sensor and antenna modules by designing antennae with sensing capability.

#### **3.4.1. Overview**

A wireless sensing antenna detects external physical phenomenon by modifying its  $f_0$ . It is known that the resonant frequency of an RF structure is defined as the frequency point where minimum  $S_{11}$  occurs. For RF structures used for radiating microwaves, i.e. antennae, or other RF structures embedded with antennae, the RF energy transmitted and/or reflected back by the antenna forms a peak at the receiver side [28, 31]. Therefore, a wireless sensing antenna can be realised by relating the detected variation of  $f_0$  with the property of the sensed phenomenon, or sensed signal.

An initial resonant frequency value ( $f_0$ ) is normally set for a wireless sensing antenna when there is no external phenomenon is applied to the sensing structure, which

represents a state of *non-excitement* of the antenna. It is quite common that the variation of the resonant frequency of most wireless sensing antennae have a relatively linear response to the sensed signal ( $S$ ), so that this response can be modelled as [97]:

$$S(f_0) = \frac{|f_0 - f_0|_{S=0}|}{\frac{df}{dS}} \quad (3.23)$$

where  $S(f_0)$  is the measured value of the sensed phenomenon,  $f_0|_{S=0}$  is the initial resonant frequency,  $f_0$  is the resonant frequency after excitation by the sensed signal, and the  $\frac{df}{dS}$  is the system sensitivity.

It is of interest to understand which parameters can affect the  $f_0$  of antennae. Generally, for a simple microstrip antenna,  $f_0$  depends on the geometry of the antenna patch and the permittivity of the substrate material [28]. Therefore, by relating the property of the sensed signal with the variation of either geometrical dimension or permittivity value, a wireless sensing antenna can be designed.

However, sometimes the above resonant-frequency-shifting effect due to external phenomenon, e.g. temperature or pressure, is not significant. Therefore, several approaches have been proposed to mitigate this effect. The first approach is to cover the electrodes, e.g. antennae or  $LC$  tank circuits, with a sensitive layer such as cellulose acetate butyrate (CAB) which is sensitive to the humidity [98]. The second approach is to use the sensitive substrate directly which would bring down the design complexity [99].

There are two common designs for the RF-based sensing structures. The first design utilises an antenna, which shifts its  $f_0$  with the property of the sensed phenomenon, and works with other RF components, e.g. RF identification (RFID) tag chips or active RF transmitters, which can provide the RF signals [100]. Therefore, such systems could be battery-free (e.g. when working with a passive RFID tag integrated circuits). The second design utilises resonant circuits, e.g. a  $LC$  tank circuit, in conjunction with antennae, or just the  $LC$  circuit alone for short-range applications [101–103]. In the latter design, the resonant circuits are the sensing structures and can be designed to be a highly compactable structure, thereby further minimising their sizes.

### **3.4.2. Sensing by mechanical deformation**

The easiest way to achieve mechanical deformation is to change the geometrical dimensions of the sensing structures. This can be achieved by applying force to compress

(see Figure 3.7(a)) or stretch (see Figure 3.7(b)) the wireless sensing structures, as they are applied to realise pressure sensors, and strain sensors, respectively.

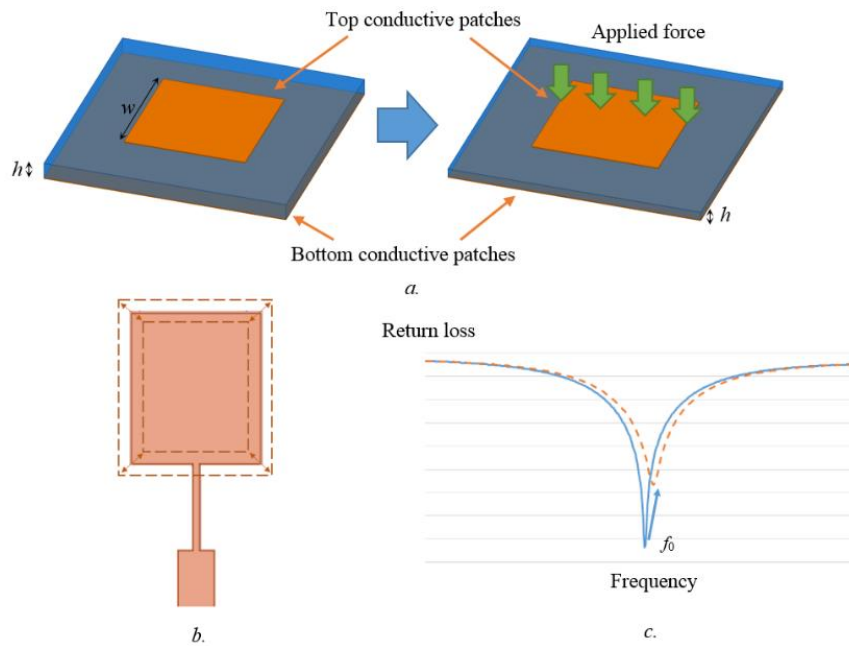


**Figure 3.7. The working principle of: (a) pressure sensing antenna; (b) strain sensing antenna; and (c) a shift to the resonant frequency ( $f_0$ ) due to the external force.**

Pressure sensors normally have a dielectric material sandwiched between two conductive patches [104]. For example, assuming the sensing structure is a patch antenna, with the top conductive patch being normally the radiation patch whereas the patch on the other side of the substrate acts as the ground plane. Because the EM field that decides the resonant frequency propagates only within the dielectric between two patches, the change of physical thickness ( $h$ ) of the dielectric substrate leads to the redistribution of the EM field inside the substrate. This effect impacts the  $\epsilon_{eff}$  of the antenna and results in a change of the  $f_0$  (see Figure 3.7(c)). Suppose the geometrical dimension of both conductive plates does not change when the forces are applied, then the  $f_0$  of the antenna will increase with decreasing thickness of the substrate:

$$f_0 \sim \frac{1}{h} \sim \frac{1}{\epsilon_{eff}}. \quad (3.24)$$

Therefore, the critical part that affects the performance of a pressure sensing antenna is the choice of a suitable deformable dielectric substrate.

Strain sensing antennae are designed based on the theory that the antenna resonates when its geometrical size is similar to that of its electrical length [28]:

$$l_e = \frac{l}{\lambda_0} = \frac{l \times f_0}{c} \quad (3.25)$$

where  $l$  is the physical length,  $l_e$  is the electrical length,  $\lambda_0$  is the wavelength of operating frequency, and  $c$  is the speed of the light. As can be concluded from (3.25), the variation in the physical length  $l$  will definitely alter its resonant frequency  $f_0$ . The strain sensing has potential applications in measuring surface-deformation (e.g. skin ulceration and pregnancy), heart beats, blood pressure, and so on [103].

In [104], an ultra-small pressure sensing antenna was proposed for continuous intracranial pressure (ICP) and pulse monitoring. It adopted a layer of enhanced flexible micro-structured styrene-butadiene-styrene (SBS) elastomer with reduced viscoelastic behaviour as the dielectric substrate. In addition to the thickness variation, the surface of SBS elastomer has quite a number of pyramidal microstructures (PYMs). When pressure is applied, the air between PYMs will be expelled, which results in an improved sensitivity of the developed sensing antenna. The resonant structure consists of two inductive spirals acting as antennae, each on one side of the SBS. The whole stacked structure acts as a resonant tank circuit. With pressure applied, the change in capacitance between the coils is transmitted to external devices by the coils.

Another application for strain sensing is a “smart fabric bellyband” in which a microstrip antenna pattern was knitted with silver-coated yarns [105]. The knitting technique was used because it employs loose and interleaving structures during the fabrication process (see Figure 3.8). Therefore, when the antenna pattern is stretched, its geometry will change according to the tension of the force, which leads to the change in the antenna’s  $f_0$  and radiation properties (e.g. gain).

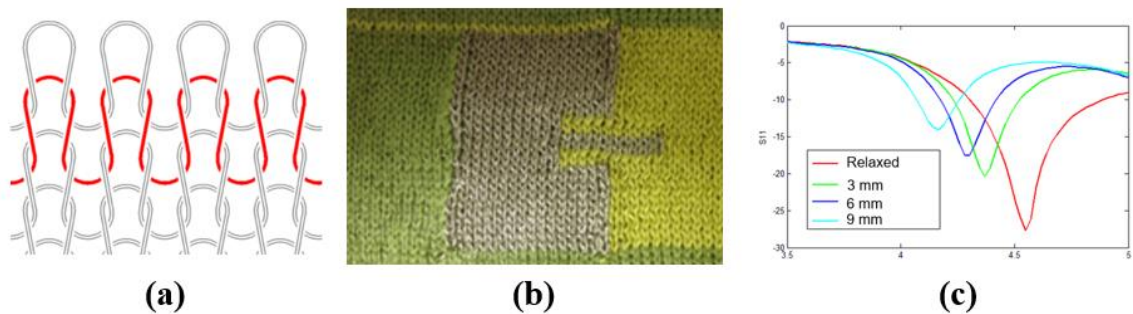


**Figure 3.8. Smart belly band: (a) knitting structure; (b) knitted microstrip sensing antenna; and (c)  $S_{11}$  response to the stretch [105].**

### 3.4.3. Sensing by electrical permittivity

Apart from the mechanical deformation to the physical geometry of sensing antennae, the permittivity, or the  $\epsilon_r$  of the substrate material can also be made to change in response to the sensed signal.

One important property of the  $\epsilon_r$  is that it is not a constant value for the same material under different conditions. For example, for most dielectric substrates used in wearable applications, such as textiles and thin plastic film, their dielectric constant  $\epsilon_r$  increases with rising temperature or humidity. As mentioned previously, the  $f_0$  of the sensing antenna shifts with the  $\epsilon_r$  of the substrate material:

$$f = \frac{v_p}{\lambda} = \frac{c}{\lambda\sqrt{\epsilon_r}} \quad (3.25)$$

Therefore, it is a promising method to monitor the parameters of ambient environment.

In [97], an inkjet-printed passive RFID antenna for sensing ambient humidity was fabricated. This system was intended for sensing ambient humidity within buildings but can be potentially used as part of a wearable health-monitoring system. The sensing antenna was printed on flexible Kapton film which has a linear humidity-permittivity response, and therefore no extra moisture-sensing layer is required. In order to effectively convert the variation of  $\epsilon_r$  into a resonant frequency shift, the arms of the antenna consists of multiple parallel printed conductive plates, thereby increasing the sensitivity of the capacitive sensing. A relatively linear response between the humidity and the lowest-power-on-tag frequency was characterised with a sensitivity of 171 kHz/%RH.

In [101], an LC resonant circuit was fabricated on a piece of flexible and stretchable substrate to sense the existence of sweat on the skin surface. The microporous substrate can spontaneously absorb sweat released from the skin, and thus the dielectric property, i.e.  $\epsilon_r$ , of the substrate changes, which in turn alters the frequency characteristics of the LC sensing circuit. Furthermore, by integrating functional microelectrodes inside the substrate, it is capable of identifying specific chemical ions (e.g.  $\text{OH}^-$  and  $\text{H}^+$ ) in the sweat as they introduce colorimetric effect in the substrate. An external coil antenna can be used to detect the shift of the resonant frequency of the LC circuit.

### 3.5. Summary

This chapter first reviews some widely used methods for characterising dielectric and conductive materials at high frequency. The methods for dielectric characterisation can generally be classified as either a non-resonant method or as a resonant method. Non-resonant method is able to measure dielectric materials over a wide frequency range whereas the resonant method characterises materials at single or discrete frequencies. The conductive materials are normally characterised by measuring the variation of RC and  $Q$ -factor of a resonator with an inserted MUT.

Thereafter, recent proposed structures and designs of EBGs are discussed. The unique properties of EBGs make it a novel substrate material for coplanar antennae. There are mushroom-like EBGs and UC-EBGs, which have been successfully implemented to improve antennae's performance such as enhanced  $S_{11}$ , optimised radiation pattern, and reduced mutual coupling for antenna array.

Finally, reviews on wireless sensing antennae are given. The existing sensing antennae are realised by relating the shift of resonant frequency with external sensed signal. Two different sensing mechanisms are discussed: mechanical sensing and permittivity sensing mechanisms, with illustrated examples for each category.

# Chapter 4

## A Hybrid-Microstrip-Line Method for Material Characterisation

### 4.1. Introduction

As discussed in previous chapters, the performance of antennae and other structures operating at radio frequencies (RF) is highly affected by both the dielectric property of the substrate material and the electrical property of the conductive material [28]. A prior understanding of these properties is critical in delivering a high-quality RF circuit. This is especially important for designing narrowband RF structures such as resonators and sensing antennae. Particularly with short operating wavelength at mm-wave frequencies, the permittivity deviations of the substrate materials can lead to greater frequency shifts in the designed RF structures than at microwave frequencies [61].

However, most substrate manufacturers do not include information about their dielectric properties above 10 GHz in the technical data sheet. Besides, dielectric materials used today for on-body RF applications are not only limited to conventional rigid ceramic laminates, but can include non-conventional flexible materials such as textile fabrics as readily available on the market [106], many of which have no known dielectric values. Moreover, the dielectric properties of different textile products made of the same materials may also vary due to their different fibre construction and organisation methods [20]. Therefore, having a simple and fast method to characterise dielectric materials can significantly shorten the RF design cycle and minimise the frequency shift problem.

This chapter first proposes a novel hybrid-transmission-line (hybrid-TL) method for accurate and quick characterisation of flexible dielectric materials, in which two error boxes are introduced to eliminate the effects of impedance mismatch due to transmission line discontinuity at the interfaces. Based on the proposed method, a test fixture is designed and assembled, which is then utilised for analysing the properties of several

rigid PCBs and flexible fabric materials. Finally, the accuracy of the proposed method is validated and compared with the existing two-transmission-line method.

## 4.2. Hybrid-transmission-line Method

The dielectric materials for wearable applications are normally thin and light, such as fabrics and flexible PET film [20]. However, the characterisation of thin materials ( $< 1\text{mm}$ ) presents an accuracy challenge since any variation of the material's thickness can result in accuracy errors to the characterised dielectric properties. Therefore, a characterisation method that depends less on thickness but more on transverse geometry can lead to more accurate results. Methods based on wave transmission/reflection (T/R) are a good option since the components of the permittivity parallel to the substrate plane ( $\epsilon_{xx}$  and  $\epsilon_{yy}$ ) are measured. With the knowledge of most common RF characteristics of integrated transmission lines, generally determining  $\epsilon_{xx}$  and  $\epsilon_{yy}$  is sufficient for designing high frequency circuits [63].

Dielectric characterisation using two-transmission-line (L-L) and covered-transmission-line (covered-TL) methods were briefly discussed in Chapter 3. Both methods are classified as T/R methods and have been widely adopted for measurement of dielectric properties in both industry and academia research [19, 59, 60, 62, 63]. However, their measured results suffer from impedance mismatches, non-identical transitions, and calibration errors, which caused errors when de-embedding the propagation properties of the materials under test (MUTs) from the measured  $S$ -parameters. Practically, for an L-L method, two TLs with identical characteristic impedance  $Z_0$  but of different lengths must be fabricated onto every MUT to be characterised, prohibiting the use of a “universal” test fixture with two common TLs for all MUTs [19]. On the other hand, a covered-TL method needs a test fixture with known RF properties and a perfect impedance match between the connectors and the on-board TL, which possesses a number of fabrication challenges at mm-waves [63].

The proposed hybrid TL method in this chapter enables the characterisation of dielectric materials without having to know the RF characteristics of the transitions or interfaces based on an approach that may be considered as a hybrid between L-L and covered-TL methods. The focused dielectric materials in this thesis are thin dielectric laminates such as fabric pieces or flexible PCB laminates. This section begins with a theoretical analysis of the proposed method, followed by the design and performance evaluation of the test fixture.

### 4.2.1. Hybrid-transmission-line method

The model for the proposed hybrid-TL method is shown in Figure 4.1. Here, the microstrip-line is used as an example, but the proposed method can be applied to other TL types such as coaxial cables and CPW lines. Two error boxes A and B, one at each end of test fixture, are introduced to represent impedance mismatch and signal path discontinuities caused by the signal path transitions from one type of transmission line to another (e.g. from coaxial cable to the microstrip-line). It should be noted that the RF characteristics (i.e.  $S$ -parameters) of the transitions are not required to be known a priori.

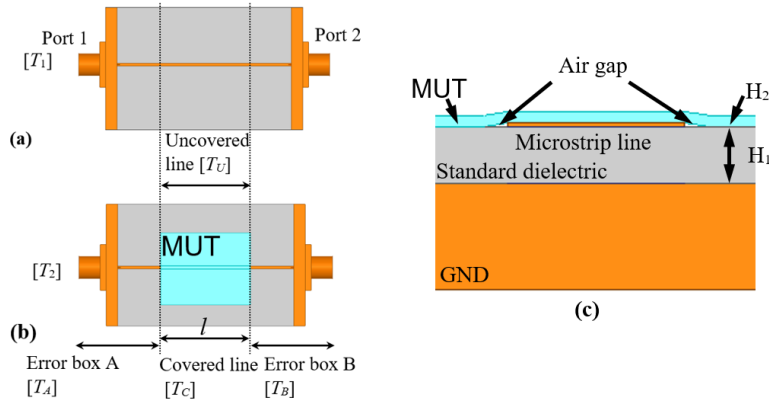


**Figure 4.1. Hybrid-TL model for (a) uncovered; (b) covered scenarios and (c) side view of covered scenario.**

The section between two error boxes is a  $50\text{-}\Omega$  microstrip-line fabricated on a standard substrate with known dielectric properties, which has the same physical length  $l$  as the MUT.

The properties of the standard substrate can be obtained beforehand by other existing characterisation methods such as the L-L method. From (2.10), for both uncovered and covered scenarios, their  $T$ -parameters ( $[T]$ ) are the product of each cascaded subsection:

$$[T_1] = [T_A][T_U][T_B] \quad (4.1a)$$

$$[T_2] = [T_A][T_C][T_B] \quad (4.1b)$$

where  $[T_1]$ ,  $[T_2]$ ,  $[T_A]$ ,  $[T_B]$ ,  $[T_U]$ , and  $[T_C]$ , are the  $T$ -parameters of the uncovered fixture, covered fixture, error box A, error box B, uncovered microstrip-line, and covered microstrip-line, respectively, as shown in Figure 4.1.  $[T_1]$  and  $[T_2]$  can be converted from measured  $S$ -parameters ( $[S]$ ) of uncovered and covered fixture following Table 3.1.

Note that both  $[S]$  and  $[T]$  matrices are complex values, i.e. they have both magnitude and phase information. By multiplying (4.1a) by inverse of matrix  $[T_2]$ , we can obtain:

$$[T_1][T_2]^{-1} = [T_A][T_U][T_C]^{-1}[T_A]^{-1} \quad (4.2)$$

According the definition of similar matrix,  $[T_1][T_2]^{-1}$  and  $[T_U][T_C]^{-1}$  have the same eigenvalues ( $\lambda$ ):

$$\lambda([T_1][T_2]^{-1}) = \lambda([T_U][T_C]^{-1}). \quad (4.3)$$

Supposing that the uncovered microstrip-line section has an ideal 50- $\Omega$  characteristic impedance, from (3.16), its  $T$ -parameters can be expressed as:

$$[T_U] = \begin{bmatrix} e^{-\gamma_1 l} & 0 \\ 0 & e^{\gamma_1 l} \end{bmatrix}. \quad (4.4a)$$

Similarly, the  $T$ -parameters of the covered microstrip-line is:

$$[T_C] \approx \begin{bmatrix} e^{-\gamma_2 l} & 0 \\ 0 & e^{\gamma_2 l} \end{bmatrix} \quad (4.4b)$$

where  $\gamma_1$  and  $\gamma_2$  are complex propagation constant of uncovered and covered microstrip-line, respectively, and  $l$  is the physical length of MUT, which should be at least twice the operating wavelengths for accurate measurement. It has been shown in [59] that the characterised results of a covered-line method are not sensitive to the size of the MUT as long as the length requirement can be fulfilled.

It should be noted that (4.4b) is only valid when  $Z_0$  of the microstrip-line does not change significantly when covered with MUT, i.e. standing wave ratio (SWR) due to impedance mismatch is within 2, or  $|\Gamma|^2 \leq 0.1$  [57]. Otherwise,  $T_{12}$  and  $T_{21}$  of the  $[T_C]$  in (4.4b) are no longer close to zero. While in this work, assuming that for a MUT with a given thickness of 0.35 mm, its  $\epsilon_r$  ranges from 1 to 20, which is sufficiently wide to cover most common dielectric materials such as conventional PCB laminates and textile fabrics. With reference to Table 2.1 in Chapter 2, the  $Z_0$  of the covered section will correspondingly reduce from 50 to 39  $\Omega$ . In turn, this change in  $Z_0$  results in a SWR of 1.28 over the covered line, which can meet the aforementioned requirement.

Since  $[T_U]$  and  $[T_C]$  are diagonal matrices, the two eigenvalues of  $[T_U][T_C]^{-1}$  can be derived as:

$$\lambda_{1,2}([T_U][T_C]^{-1}) = e^{\pm(\gamma_1 - \gamma_2)l} = \lambda_{1,2}([T^{12}]) = \frac{(T_{11}^{12} + T_{22}^{12}) \pm \sqrt{(T_{11}^{12} + T_{22}^{12})^2 - 4(T_{11}^{12} T_{22}^{12} - T_{12}^{12} T_{21}^{12})}}{2} \quad (4.5)$$

where  $[T^{12}] = [T_1][T_2]^{-1}$ . Because  $e^{\pm(\gamma_1 - \gamma_2)l}$  is a function with periodic of  $2\pi$ , by rearranging (4.5), we have:

$$\gamma_2 = \gamma_1 \mp \frac{1}{l} \ln[\lambda_{1,2}([T^{12}]) \pm j2n\pi]. \quad (4.6)$$

Since the RF characteristics of fixture's transitions (i.e.  $[T_A]$  and  $[T_B]$ ) are unknown,  $\gamma_1$ , which is the complex propagation constant of the uncovered microstrip-line, in (4.6) cannot be measured with certainty, but can be derived from simulated  $S$ -parameters of a microstrip-line of identical geometry. This is because the middle section in Figure 4.1(a) is a carefully designed microstrip-line with a  $Z_0$  of  $50 \Omega$ , and thus it should follow the transmission-line theory and the simulated results.

Once  $\gamma_2$  is obtained, the effective dielectric constant ( $\epsilon_{eff}$ ) of the covered microstrip-line section can be derived from:

$$\epsilon_{eff} = (\beta/k_0)^2 \quad (4.7)$$

where  $k_0$  is the wave number in free space, and  $\beta = \text{Im}(\gamma_2)$  is the phase constant. It also gives the actual phase ( $\varphi$ ) of insertion loss ( $S_{12,C}$  or  $S_{21,C}$ ) of the covered microstrip-line:

$$\varphi = \angle e^{-j\beta l} \quad (4.8)$$

A structure with identical geometry of the fabricated microstrip-line is then simulated in the simulation software, HFSS, and the actual dielectric constant ( $\epsilon_{rM}$ ) of MUT is found by iteratively refining  $\epsilon_{rM}$  in HFSS to a value which produces a simulated  $\varphi$  that most closely matches with the actual  $\varphi$  found from  $\epsilon_{eff}$ .

Since the effect due to the size of MUT is inherently included in the measured  $[T_2]$ , a MUT with different dimensions will result in different  $\epsilon_{eff}$ , which gives the actual phase angle ( $\varphi$ ) of transmission coefficients (TC) of the covered microstrip-line structure.

In order to reduce the derivation complexity of the proposed method, this thesis utilises the transmission coefficient ( $S_{12}$  or  $S_{21}$ ) instead of reflection coefficient ( $S_{11}$  or  $S_{22}$ ) that requires the consideration of wave reflections at the impedance discontinuous planes for the covered scenario as illustrated in Figure 4.2. Note that for a passive circuit without any active component, the signal path either from port 1 to 2, or from port 2 to 1 should be the same. Thus, the  $S_{12}$  and  $S_{21}$  values should be equivalent in both the magnitude and phase, and either value can be used to derive  $\epsilon_{rM}$ . In this thesis, we arbitrarily chose  $S_{12}$ .

Regarding the loss factor of the MUT, when a high-conductive and low-loss conductor such as copper is used as the signal path, the attenuation constant  $\alpha = \text{Re}(\gamma_2)$  is largely contributed by the dielectric material. Therefore, the loss tangent of the MUT ( $\tan \delta_M$ ) can be calculated as [104]:

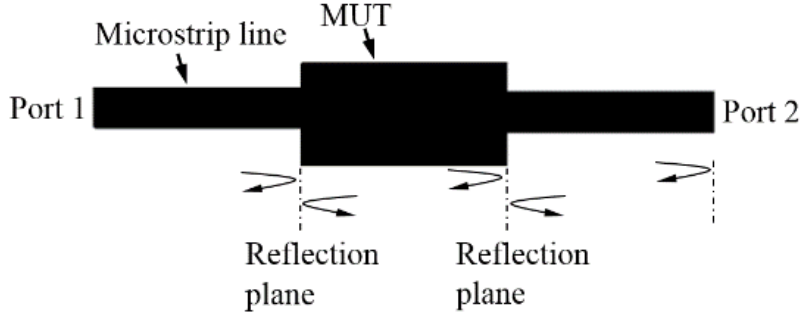


**Figure 4.2. Reflections at impedance discontinuous points.**

$$\tan \delta_M = \frac{\epsilon_{rM}-1}{\epsilon_{rM}(\epsilon_e-1)} \left[ \frac{\alpha \lambda_0 \sqrt{\epsilon_{eff}}}{27.3} - \left( \frac{\epsilon_{eff}-\epsilon_e}{\epsilon_{rS}-1} \right) \epsilon_{rS} \tan \delta_S \right] \quad (4.9)$$

where  $\epsilon_{eff}$  is the effective dielectric constant of the microstrip-line,  $\lambda_0$  is the free space wavelength,  $\epsilon_{rS}$  and  $\tan \delta_S$  are the known dielectric constant, and loss tangent, respectively, of the standard substrate material.

#### 4.2.2. Test fixture design

A test fixture is designed and assembled as shown in Figure 4.3 based on the method presented previously. This fixture is suitable for measuring the focused thin and flexible dielectric materials (e.g. PCB laminates and fabric pieces). The standard dielectric in Figure 4.1 is chosen to be Rogers RT/d5880 laminate since it has excellent dielectric stability over a wide range of frequency. The dielectric constant ( $\epsilon_{rS}$ ) and loss tangent ( $\tan \delta_S$ ) of this substrate is 2.2 and 0.001, respectively, which are valid from 20 to 40 GHz.

A 50- $\Omega$  microstrip-line of width 786  $\mu\text{m}$  is etched on a 254  $\mu\text{m}$  thick standard RT/d5880 substrate (see Figure 4.3(a)). Two 2.92-mm female coaxial connectors (i.e. K connectors) from Southwest Microwave, INC. are used to allow measurements of up to 40 GHz. A 3D-printed plastic base containing an air chamber is placed under the fixture as the mechanical support (see Figure 4.3(b) and (c)) of the fixture. A number of 0.8-mm holes are drilled on top side of fixture for holding down MUTs through air suction, which is important for ultra-light materials such as fabrics and minimise the size of air gaps that may exist between the fixture and the MUT. Notably, the size of the drilled holes (0.8

mm) is much smaller than the operating wavelength (10 mm at 30 GHz), and thus the scattering effect is not significant. In addition, the locations and the size of these holes are simulated in HFSS to ensure that the effects due to the introduced suction holes are included during the characterisation process.

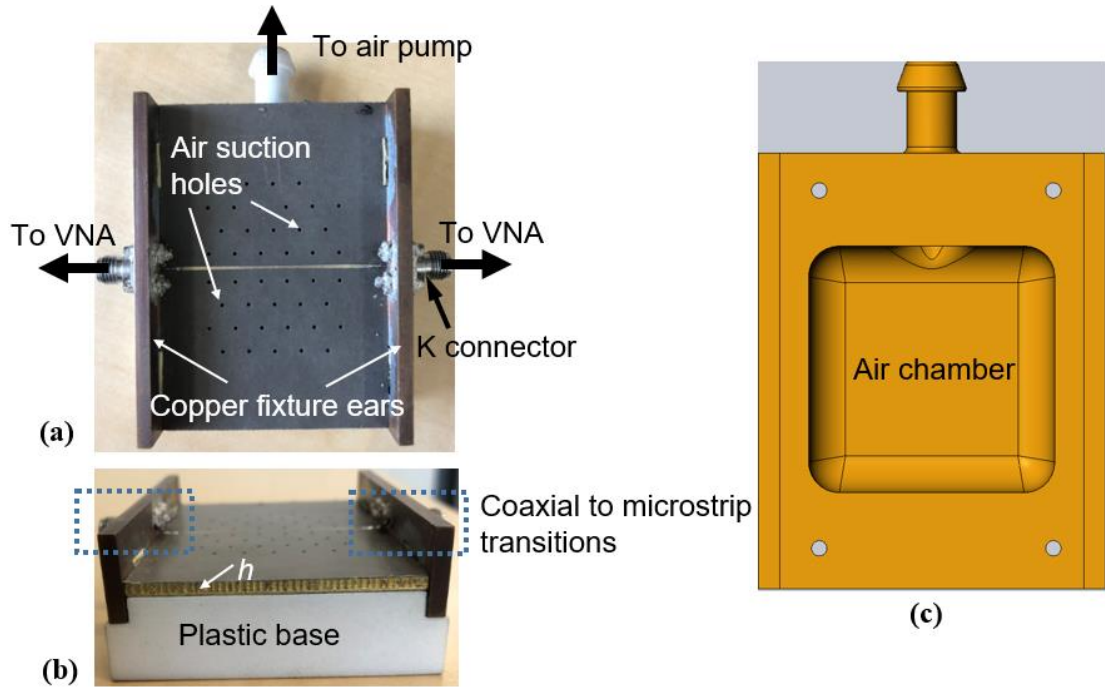


**Figure 4.3. Designed test fixture: (a) top view; (b) side view; and (c) plastic base model.**

Efforts are made during the fixture design and assembling process to minimise the RF energy loss and provide reliable measurements. First of all, the thickness ( $t$ ) of the copper microstrip-line is selected as  $17.5 \mu\text{m}$ , which greatly reduces the size of the air gap that may exist between the MUT and the microstrip-line. Secondly, a customised RT/d5880, one side of which has a 2-mm thick copper cladding instead of the usual  $17.5$  or  $35 \mu\text{m}$ -thick cladding, is ordered from the manufacturer (Rogers Corporation) to fabricate the standard dielectric, serving as a solid ground plane. Thirdly, two copper fixture ears are designed to hold the K connectors, and firmly attached to the thick ground plane of the dielectric board using highly conductive silver epoxy (MG Chemicals, MG8330S-21G, vendor-specified electrical resistivity  $< 0.0007 \Omega \cdot \text{cm}$ ). The second and third efforts significantly reduce the energy loss due to the signal transitions, and the backward current flow over the ground. Furthermore, both ends of the microstrip-line are tapered to reduce the impedance mismatch due to the different geometries of the microstrip-line width  $w$  ( $786 \mu\text{m}$ ) and the diameter of the central pin of K connectors ( $305 \mu\text{m}$ ). The parameters of the fixture are listed in Table 4.1. More detailed information regarding the mechanical drawings and bill of materials of the fixture can be found in Appendix A.

An Anritsu Site Master S820E is used to perform full 2-port measurements in the frequency range from 37 to 39 GHz. The instrument has been pre-calibrated with the conventional short-open-load-thru (SOLT) technique, which involves a set of standard calibration kits, i.e. short, open, matching load and thru, in turn to be connected at the end of measuring cables so that the signal loss and errors due to the cables, adapters and the instrument itself can be removed [108].

**Table 4.1. Parameters of the test fixture.**

Parameter	Value
Microstrip-line width $w$	$786 \mu\text{m}$
Microstrip-line thickness $t$	$17.5 \mu\text{m}$
Dielectric thickness $H_1$	$0.254 \text{ mm}$
Standard dielectric constant $\epsilon_{rS}$	$2.2$
Standard loss tangent $\tan \delta_S$	$0.001$
Ground plane thickness	$2 \text{ mm}$
Diameter of the central pin of K connector	$305 \mu\text{m}$

The magnitude of the fixture's measured  $S$ -parameters is plotted in Figure 4.4. Since an ideal matched microstrip line should give a  $S_{11} < -20 \text{ dB}$ , the result confirms the imperfect impedance match between the microstrip-line and coaxial K connectors, and imperfect symmetric ( $S_{11} \neq S_{22}$ ) property of the fixture. However, it still shows an acceptable matching characteristic as both  $S_{11}$  and  $S_{22}$  are less than  $-10 \text{ dB}$  over the frequency of interest. Therefore, this fixture can be used for validating the efficacy of the proposed characterisation method under imperfect conditions at mm-waves.

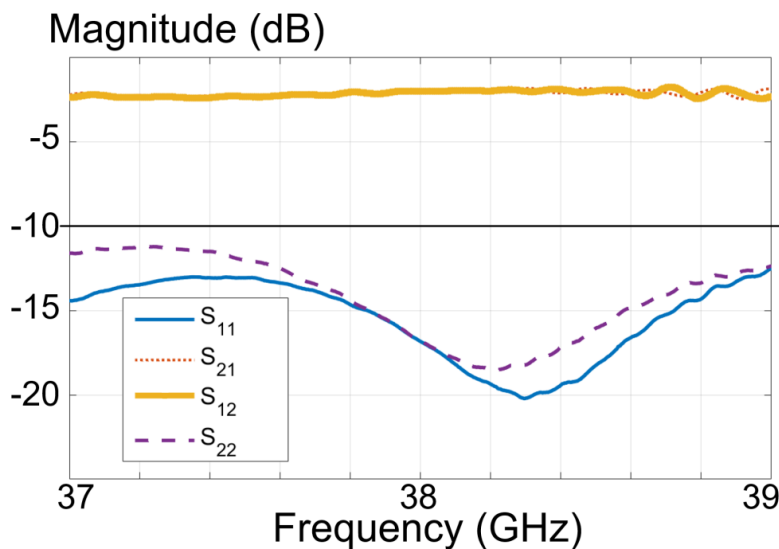


**Figure 4.4. Measured  $S$ -parameters of the designed test fixture.**

In Section 4.2.1 and (4.9), it is assumed that the conductor loss due to low-loss conductor is negligible. For a simple illustration, consider the physical length ( $l$ ) of the 50- $\Omega$  microstrip-line to be 25 mm, and thus its conductor loss  $\alpha_c$  can be calculated as:

$$\alpha_c = 6.1 \times 10^{-5} \frac{R_s Z_0 \epsilon_{eff}}{H_1} \left[ \frac{W'}{H_1} + \frac{\frac{0.667W'}{H_1}}{\frac{W'}{H_1} + 1.444} \right] \cdot A \cdot l = 0.08 \text{ dB}$$

where  $R_s$  is the surface resistivity of copper,  $W'$  is the effective width of microstrip-line,  $H_1$  is the thickness of standard RT/d5880 substrate in Table 4.1, and  $\epsilon_{eff}$  is the effective dielectric constant of the multilayer microstrip-line system. The equations for calculating coefficient  $A$  and  $W'$  can be found from [107].

On the other hand, the ideal total loss ( $\alpha$ ) of the same multilayer microstrip-line system is found to be 0.98 dB from HFSS. This value is based on having a 0.35-mm-thick polyester ( $\epsilon_{rM} = 2.76$ ,  $\tan\delta = 0.0035$ ) as the covered MUT. Therefore, compared to this total loss value, the conductor loss from the copper line is not significant.

### 4.3. Characterisation Procedure

#### 4.3.1. Measurement setup and steps

Figure 4.5(a) illustrates the measurement setup for obtaining the  $S$ -parameters of the fixture. The test samples are firstly cut into rectangular shapes with a size around 25×30 mm<sup>2</sup>, and then placed on top of the test fixture as shown in Figure 4.5(b).

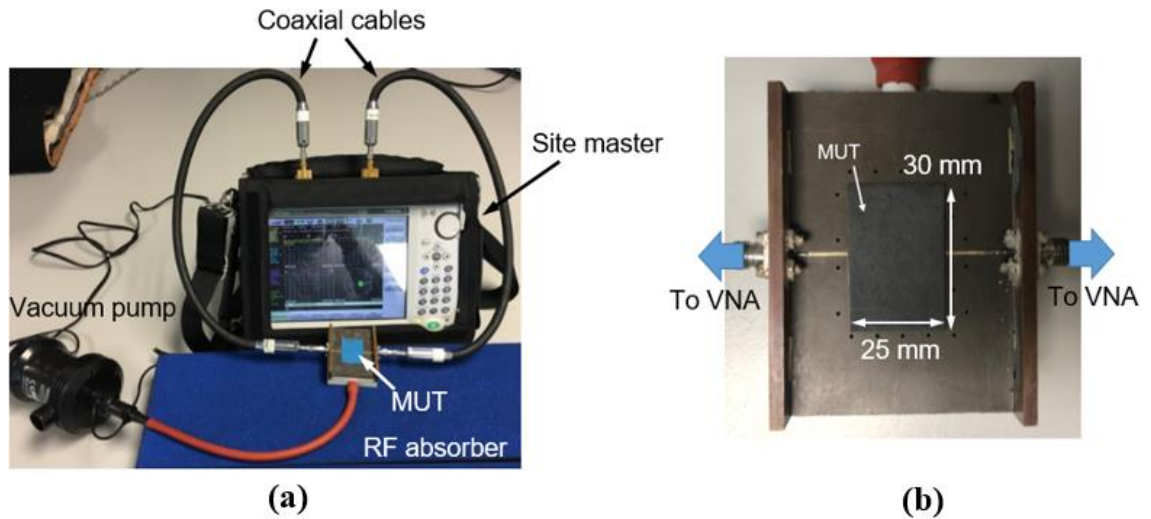


**Figure 4.5. Measuring  $S$ -parameters of the fixture: (a) test setup; and (b) MUT placed on the fixture.**

A vacuum pump is connected to the fixture for air suction. Microwave absorbers are used to avoid RF reflections from the test bench to obtain accurate results.

All together there are 8 steps used to characterise a material sample:

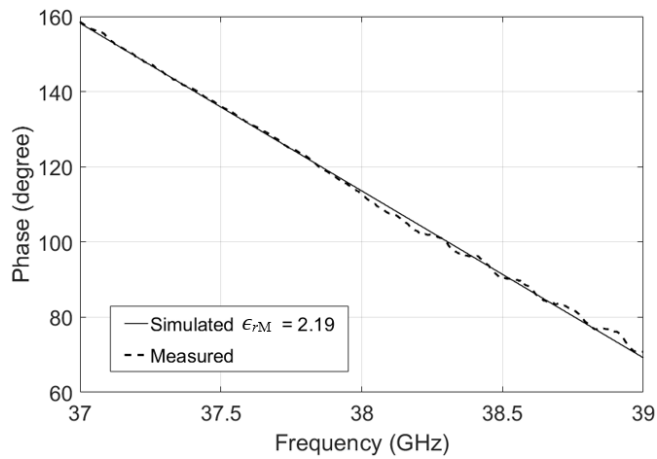
1. Measure the  $T$ -parameters of the uncovered fixture [ $T_1$ ];
2. Measure the  $T$ -parameters of the fixture covered with MUT [ $T_2$ ];
3. Simulate the  $T$ -parameters of the uncovered microstrip-line [ $T_U$ ] and its complex propagation constant  $\gamma_1$ ;
4. Based on Eqs. (4.1–4.6), calculate the  $T$ -parameters of the covered microstrip-line [ $T_C$ ] and its complex propagation constant  $\gamma_2$ ;
5. Calculate  $\epsilon_{eff}$  from  $\gamma_2$ , and its corresponding phase angle  $\varphi$  using (4.7) and (4.8);
6. Simulate  $\varphi$  from HFSS with an estimated  $\epsilon_{rM}$  value of around the calculated  $\epsilon_{eff}$ ;
7. Iteratively refine  $\epsilon_{rM}$  and find the one which can generate a simulated  $\varphi$  that mostly matches with the one obtained in step 6;
8. Calculate  $\tan \delta_M$  using (4.9).

#### 4.3.2. Measurement illustration

A PCB laminate Rogers RT/d5880 and a flexible polyester fabric are used to illustrate the characterisation procedure. After turning on the air pump, the MUTs are placed on top of the fixture with a fine-adjusted position to minimise the size of air gap (see Figure 4.5(b)). Eqs. (4.1–4.8) are then implemented in MATLAB to calculate  $\gamma_2$  and  $\epsilon_{eff}$  from measured  $S$ -parameters [ $S_1$ ] and [ $S_2$ ] (refer to Appendix B for the code). At least 10 measurements are taken and averaged for each MUT in this section.

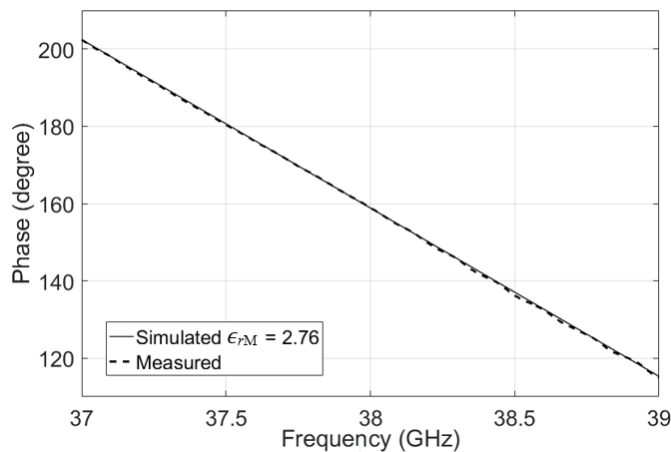
The covered structure with identical dimension is then simulated in HFSS to find the  $\epsilon_{rM}$  which gives the best-fit phase angles. The simulation also seeks to find possible geometrical errors of the fixture and air gap due to the thickness of the microstrip-line.

Figure 4.6 shows the best-fit  $\epsilon_{rM}$  of the RT/d5880, which is the same material as the standard microstrip substrate but with a different thickness ( $H_2 = 0.787$  mm). Its characterised  $\epsilon_{rM}$  is 2.19, and the calculated loss tangent  $\tan \delta_M$  is 0.0013, which are close to their vendor-specified values ( $\epsilon_{rM} = 2.2$ ,  $\tan \delta_M = 0.001$  at 40 GHz), and those reported for the same material using existing methods [63, 110].



**Figure 4.6. Simulated and measured  $S_{21}$  phase for RT/d5880.**

Then, the proposed method is further applied to characterise a piece of plain-woven polyester fabric ( $25 \times 35 \times 0.09$  mm) which can be used as a flexible substrate for e-textile applications. The characterised  $\epsilon_{rM}$  and  $\tan \delta_M$  are 2.76, and 0.0035, respectively, as shown in Figure 4.7.



**Figure 4.7. Simulated and measured  $S_{21}$  phase for polyester.**

As can be observed in Figures 4.6 and 4.7, the average phase difference between the measured and simulated results over the considered frequency range is  $0.56^\circ$  for RT/d5880, and  $0.21^\circ$  for polyester, corresponding to an uncertainty of  $\pm 0.011$  and  $\pm 0.007$ , respectively, in the measured dielectric constant values.

#### 4.4. Complex Permittivity of Measured Materials

Figure 4.8 shows 8 different types of dielectric materials (readily available on the market) that were studied with the proposed hybrid-TL method, including 6 fabric samples that

can be potentially used in wearable applications, and 2 rigid PCB laminates as references. Their description, fabrics' physical specifications, and characterised complex permittivity values measured at 38 GHz are listed in Table 4.2.

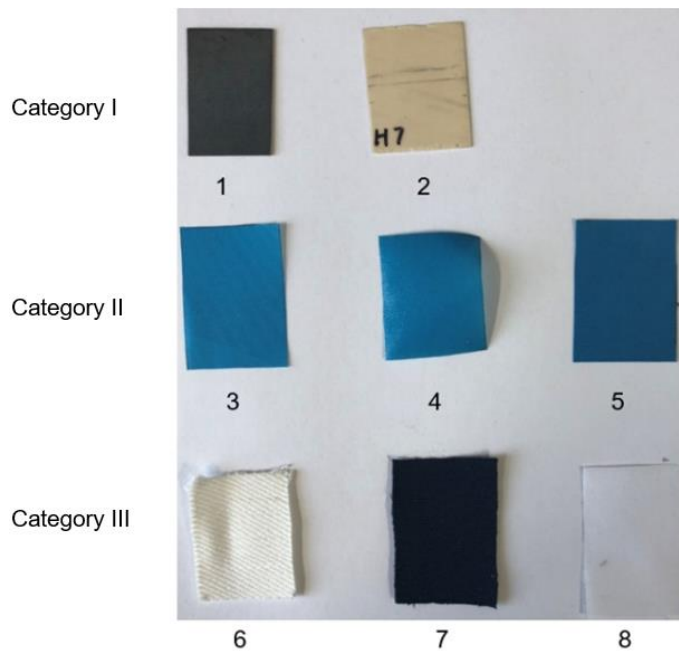


**Figure 4.8. Test samples.**

**Table 4.2. Test samples and their characterised complex permittivity values**

Category	Type	Material & Fabric weight	Thickness (mm)	Fabric structure	Warp×weft count (Dtex)	e.p.i×p.p.i	Measured	
							$\epsilon_r$	$\tan \delta$
I	1	RT/d5880	0.787	N.A.	N.A.	N.A.	2.19	0.0013
	2	RO4003C	0.508	N.A.	N.A.	N.A.	3.54	0.0032
II	3	TU Polyester 60 gsm	0.075	Plain	140×140	100×65	2.76	0.0035
	4	TC Polyester	0.095	N.A.	N.A.	N.A.	2.81	0.0036
	5	HB Polyester	0.32	N.A.	N.A.	N.A.	2.34	0.004
III	6	Cotton 260 gsm	0.66	Satin	200×1200	75×36	1.72	0.01
	7	Cotton 375 gsm	0.35	3/1 twill	700×940	55×50	1.9	0.01
	8	Silk 55 gsm	0.19	Plain	24×24	190×100	1.75	0.01

Abbreviations: TU – thin uncoated; TC – thin coated; TB – thermally bonded.

Units: Dtex – grams per 10 kilometres of yarn;

e.p.i – ends per inch; p.p.i – pick per inch; gsm – grams per square meter

All these materials in Table 4.2 can be classified into three categories:

### *Category I: standard PCB laminates*

Both RT/d5880 and RO4003C are high-reliable PCB laminates from Rogers Corporation, which are reinforced from glass fibres, and can deliver excellent stable electronic performance at RF range. Their dielectric specifications are available in their vendor's data sheet for up to 40 GHz, and thus they are used to verify the accuracy of the proposed method and the assembled fixture.

The measured  $\epsilon_r$  for RT/d5880 and RO4003C are 2.19 and 3.54, respectively, which are quite close to their vendor-specified values of 2.2 and 3.55, respectively. The measured values lead to a  $\epsilon_r$  variation of 0.45% and 0.28%, respectively.

The vendor-specified  $\tan\delta$  are 0.0009 and 0.0027 for RT/d5880 and RO4003C, respectively, at 10 GHz, which are quite close to the calculated values. However, as compared to the measured  $\epsilon_r$ , a larger deviation and a higher value for the measured  $\tan\delta$  are observed. This might be because apart from the dielectric loss, the actual loss for a covered-line system consists of conductor loss, radiation loss and some other losses due to the measurement system, which may be collectively referred to as the system noise. Therefore, the test setup of T/R method, including the proposed hybrid transmission-line method, may introduce a high noise level [19, 63]. Consequently, obtaining an accurate loss factor for the MUT requires a complete understanding of the aforementioned losses. However, this impact is minor if the value of  $\tan\delta$  is below the order of 0.001 for low-loss materials, such as the fabrics used in this thesis [61, 63, 111].

### *Category II: synthetic polyester fabrics*

Polyester is a group of polymers which contain the ester functional group in their main chain. After chemical processing, polyester fibres are extensively used for everyday clothing and home furnishing. Besides, they can be spun together with natural fibres to produce products with blended properties. The advantage of using polyester fabrics is that their ultra-fine fibres can render a relatively smooth surface, which reduces the dielectric variation of the substrates, and enable easier attachment with metallic parts.

Three different types of polyester fabrics, purchased from local fabric suppliers, were examined. Sample type 3 is a single-layer polyester whereas type 4 is coated with smooth interface layer paste (Fabink-UV-IF1) that can reduce the surface roughness and improve the quality of conductive patterns fabricated with printing techniques. Type 5 is a thicker version of sample 3 made by thermally bonding four layers of polyester, resulting in a

final thickness of 0.32 mm. This is done because using a single layer presents challenges to fabricating ultra-fine structures. For example, a 50- $\Omega$  microstrip line is 0.15-mm wide on a 0.075-mm-thick polyester fabric but is 0.762-mm wide on a 0.32 mm thick substrate. The fabrication process of sample type 5 will be explained in Section 5.2.1, where the processes of preparing both dielectric substrates and conductive patterns are presented.

From Table 4.2, the  $\epsilon_r$  of sample type 4 is slightly larger than that of type 3 and has a similar loss factor. This might be due to the fact that the smooth paste fills in the spaces between the polyester fibres and therefore increases the material's  $\epsilon_r$ . Type 5 shows a lower  $\epsilon_r$ , which is probably due to the fabrication process and the introduced bonding material. A steam iron was used for melting the bonding material sandwiched between two single-layer polyester, during which the fluid bonding material filled in the spaces between fibres and increased the spacing size. Since the bonding material has a  $\epsilon_r$  that is close to that of air, the increased spacing size decreases the resultant  $\epsilon_r$  of the fabricated polyester-bonding-material mixture.

### *Category III: woven natural fibre fabrics*

In this category, cotton and silk fabrics supplied by AUT's Textiles and Design Lab or from local fabric retailers were studied. Cotton is widely used for making textile products, including jeans, underwear, T-shirts, bed sheets and towels. Silk is an excellent material for clothing such as shirts, ties and formal dresses.

From the characterised results, both materials have very low  $\epsilon_r$  of  $< 2$ . As  $\epsilon_r$  of air is 1, and a dense material contains less air gaps between textile fibres, sample 7 has a slightly higher  $\epsilon_r$  than that of sample type 6.

In this thesis, sample type 5 was chosen as the substrate for our antenna and EBG design later in Chapter 5. This is because wearable RF structures normally require smooth surfaces so that conductive patterns can sit firmly on the substrate. Besides, all the other single layer fabrics were either too thin or too soft, and so were not suitable for on-body applications as they can cause problems such as crumpling, distortion, and are easily damaged, which may significantly shift the performance of designed RF structures. Finally, sample type 5 exhibits a slightly lower  $\epsilon_r$ , which helps to bring down the design and fabrication difficulties for mm-wave components.

On the other hand, for the design of sensing antennae in Chapter 6, sample type 7 is chosen mainly because the cotton has excellent ability of absorbing moisture from the ambient atmosphere, which will significantly alter its  $\epsilon_r$ .

In above measurements, 3 samples (A, B and C) of each type (1–8) listed in Table 4.2 were prepared, and each sample was measured 5 times to calculate an average value of  $\epsilon_r$  and  $\tan\delta$  over 15 measurements. It has to be clarified that this thesis focuses on developing a new characterisation method rather than analysing the electrical consistency of dielectric substrates, and thus the repeatability between different measurements is more important. In order to prove this, the characterised dielectric properties of sample type 1 and type 5 for each measurement are presented in Tables 4.3 and 4.4, respectively. The reason of choosing these two sample types is because type 1 is the standard dielectric material whereas type 5 is used for designing the EBG and antennae in the following chapters. The measurement follows the sequence: A1→B1→C1→A2→B2→C2→... A5→B5→C5, where the number 1–5 here means five measurements performed on each sample (A, B and C).

**Table 4.3. Dielectric properties of each measurements for sample type 1.**

A	$\epsilon_r$	$\tan \delta$	B	$\epsilon_r$	$\tan \delta$	C	$\epsilon_r$	$\tan \delta$
1	2.19	0.0014	1	2.19	0.0013	1	2.19	0.0014
2	2.19	0.0013	2	2.2	0.0014	2	2.18	0.0013
3	2.19	0.0013	3	2.2	0.0014	3	2.2	0.0013
4	2.2	0.0013	4	2.19	0.0013	4	2.19	0.0013
5	2.19	0.0014	5	2.2	0.0014	5	2.2	0.0013

**Table 4.4. Dielectric properties of each measurements for sample type 5.**

A	$\epsilon_r$	$\tan \delta$	B	$\epsilon_r$	$\tan \delta$	C	$\epsilon_r$	$\tan \delta$
1	2.33	0.0038	1	2.34	0.0041	1	2.33	0.0039
2	2.33	0.0039	2	2.35	0.0041	2	2.33	0.004
3	2.34	0.004	3	2.34	0.004	3	2.32	0.004
4	2.33	0.0039	4	2.34	0.0039	4	2.34	0.0039
5	2.34	0.0041	5	2.35	0.004	5	2.34	0.004

From the above tables, it can be concluded that as a reliable commercialised dielectric substrate used for RF applications, type 1 shows an extremely good repeatability and consistency between different measurements and different samples (A, B and C). For type 5, sample B has slightly higher values than those of A and C, which might due to the uncertainties introduced by the fabrics (e.g. fabrication variation, slightly different density at different fabric locations). However, this variation is minor ( $\sim 0.45\%$  for  $\epsilon_r$  and  $\sim 2.5\%$

for  $\tan\delta$ ) and can be neglected. To conclude, the consistency of the characterised values for each individual sample is good. In the next section, type 5 will be used to validate the proposed method.

## 4.5. Validation and Discussion

### 4.5.1. Method validation

To validate the hybrid-microstrip line method, a 38 GHz antenna on substrate sample type 5 is designed. Using the proposed method, its dielectric properties are characterised as  $\epsilon_r = 2.34$  and  $\tan\delta = 0.004$  as shown in Table 4.2. The reason for not using materials in category A is because their dielectric properties are already well known.

The geometry and prototype of the antenna are shown in Figure 4.9. It is a microstrip antenna with an open-ended tuning stub, which is sensitive to dielectric properties of the substrate, and thus can be used to validate the accuracy of the characterised dielectric values. The antenna is cut from an adhesive aluminium thin foil ( $\sigma = 36.9 \times 10^6$  S/m) on the polyester substrate, and then mounted on a 2.92-mm end-launch connector from Southwest Microwave Inc. with 1.1–1.5 dB vendor-specified insertion loss over the frequency range of interest (37–39 GHz). The measured magnitude of  $S_{11}$  is plotted with its simulated one as a function of frequency in Figure 4.10.

It can be seen that the antenna's measured resonant frequency is in excellent agreement with its simulated one, both approximately at 37.92 GHz. The measured  $S_{11}$  is  $-32.12$  dB while the simulated one is  $-32.78$  dB. However, one can still notice a deviation of  $\pm 0.05$  GHz (an error of 0.1315%) from 38 GHz. This may be due to the unknown RF characteristics of adhesive layer of aluminium foil and the end launch connector, which are not accounted for in the simulation.

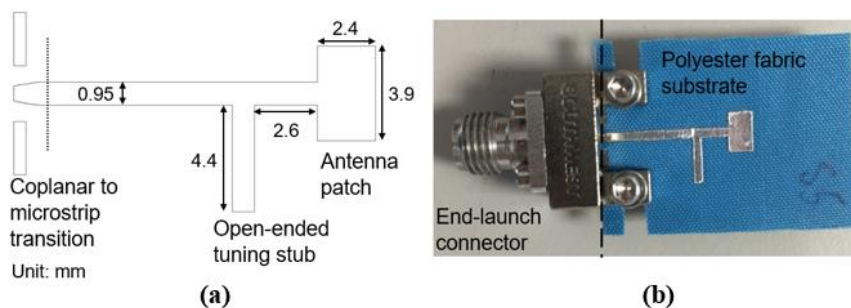


**Figure 4.9. Microstrip antenna designed based on the characterised polyester fabric: (a) geometry; and (b) fabricated prototype.**

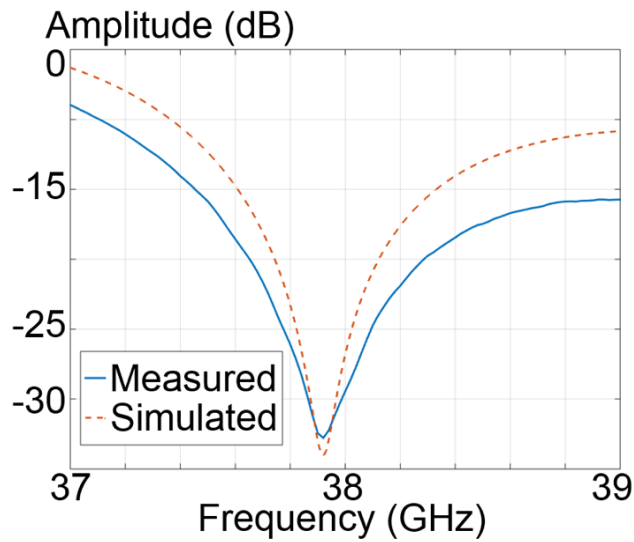


**Figure 4.10. Measured and Simulated  $S_{11}$  of the microstrip antenna.**

#### 4.5.2. Accuracy comparison with two-transmission-line method

The measurement accuracy of the proposed method is compared with that of the L-L method presented in [19, 57]. Due to the limitation of available facilities, other methods such as the covered-TL and cavity resonant methods are not able to be performed.

Here, the standard dielectric RT/d5880 (sample type 1) and thick polyester fabric (sample type 5) are chosen for this assessment. To fulfil the requirement of the L-L method, firstly, the microstrip line with identical width (0.76 mm) but different lengths are etched or cut from copper on the substrates. Then, end-launch connectors are attached to each end of the microstrip lines for measurement. Extra care should be taken when mounting the connectors so that the RF characteristics of transition sections are similar.

The fabricated samples for L-L methods and their dimensions are shown in Figure 4.11. The physical length differences between samples in (a) and (b) are 42.5 mm and 24 mm, respectively. The full 2-port measurements are taken by Anritsu S820E at the frequency range from 37 to 39 GHz.

After obtaining  $[S]$  for each microstrip line, (3.2–3.3) in Chapter 3, which are used for L-L method, are implemented in MATLAB for deriving the effective dielectric constant ( $\epsilon_{eff}$ ) of each type of substrate. The substrate  $\epsilon_r$  can be further calculated using the formulas in Table 2.1 if the  $\epsilon_{eff}$  and the thickness of the substrates are known.

Figure 4.12(a) compares the characterised  $\epsilon_r$  of RT/d5880 between L-L and hybrid-ML methods. The values obtained by both methods are quite close to that specified by the

vendor ( $\epsilon_r = 2.2$ ). However, the value obtained by L-L method shows a larger variance and a maximum error of 5.4% at 38.74 GHz.

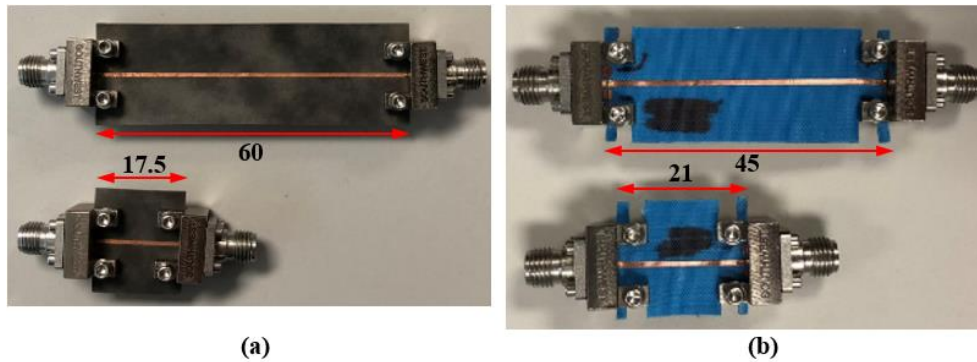


**Figure 4.11. Samples fabricated for L-L method: group (a) RT/d5880; (b) polyester fabric (Unit in mm).**

On the other hand, the characterised  $\epsilon_r$  of polyester fabric by the L-L method also varied across the frequency range of interest (37–39 GHz), with an average  $\epsilon_r$  value of 2.38 at 38 GHz (see Figure 4.12(b)). This value is slightly higher by 0.04 with the one characterised by the proposed hybrid-TL method ( $\epsilon_r = 2.34$ ). The smaller variance of hybrid-ML method may be due to the introduction of error boxes, which help to minimise the effects of impedance mismatch of signal transitions

This comparison shows that the characterised values of the L-L and the hybrid-TL methods are relatively close. It also demonstrates that without introducing the error boxes, the L-L method has a larger measurement error for the standard RT/d5880 than the hybrid-TL method. Since the assemble misalignment due to mechanical and fabrication errors are unavoidable in real measurement, the proposed hybrid-TL method in this chapter can provide a faster and more accurate solution to characterising dielectric materials.

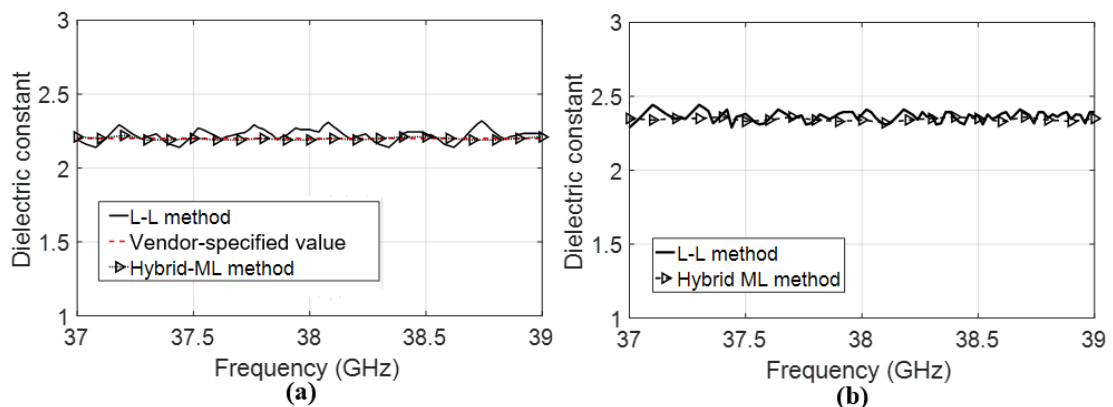


**Figure 4.12. Characterised  $\epsilon_r$  for (a) RT/d5880; and (b) polyester fabric.**

It should be noted here that from past research, the  $\epsilon_r$  of all dielectrics (including textiles) drops with an increasing operating frequency. However, for regular solid dielectrics, this drop is relatively slow except for semiconductors. For example, it has been reported that the  $\epsilon_r$  of a denim fabric drops only by 0.2 when the frequency increases from 14 to 40 GHz [112]. However, it is still necessary to characterise the dielectric substrates at the desired operating frequency band before designing mm-wave RF circuits. It is particularly beneficial for textile substrates even though the dielectric values of individual textile fibres are known. This is because the dielectric properties of textile fabrics vary significantly with different fabrication methods (e.g. knitting or weaving) and different fabric structures (e.g. yarn density, air volume and size of the pores in yarns).

#### **4.6. Summary**

This chapter firstly proposed a hybrid-TL method for characterising thin and flexible dielectric materials. With the introduction of two error boxes at each end of the test fixture, there is no requirement to know the RF characteristics of the transitions (e.g. adapters and connectors) in advance, and the influence due to impedance mismatch can be largely removed. This is particularly important for mm-wave applications, where minor mechanical misalignments when assembling connectors may significantly alter the measured RF characteristics. The effective dielectric constant of the covered-TL section can be found by varying a predefined  $\epsilon_r$  in the simulation software and matching the phase of TC produced by a value with the measured one.

Next, a universal test fixture was designed based on the proposed hybrid-TL method. The fixture was carefully designed and assembled to reduce the system loss and improve the RC of the fixture. In addition, air suction holes for holding down light and flexible MUTs onto the fixture were implemented on the dielectric board. In this way, the air gap size between the MUT and dielectric board due to the height of microstrip line can be minimised.

Thereafter, different types of dielectric materials, including both conventional rigid PCB and new flexible fabrics, were characterised using the assembled test fixture. Detailed characterisation steps were also presented in this chapter. The results show that the values of the standard RT/d5880 are close to that characterised with other existing techniques, and provided by the vendor with an error of 0.4% whereas the measurement uncertainty for the polyester fabric is  $\pm 0.007$ .

Finally, the characterised values of the polyester fabric (sample 5) were evaluated with a microstrip antenna. The result shows that the measured RC of the antenna is in well agreement with the simulated one. In addition, the proposed method was compared with the existing L-L method. This demonstrates that without the two error boxes, the L-L method may introduce greater error in the characterised values.

# Chapter 5

## Flexible EBG Design for MM-wave Wearable Antennae

### 5.1. Introduction

Electromagnetic bandgap (EBG) is a class of high-impedance surfaces (HIS), which can suppress wave propagations within a certain frequency range, thus forming a *surface wave bandgap*. As presented in previous chapters, there exist two main advantages of using EBG: 1) surface wave suppression and 2) in-phase wave reflection. Therefore, the performance of RF structures placed on top of EBG can be improved by benefiting from such bandgap of EBGs at a particular frequency.

Since wearable antennae are intended to function close to human bodies, it is important that their performance will not be significantly altered by the effects of body proximity, and the amount of backward radiation towards the body is minimised [11]. Besides, a medium to high gain ( $\geq 8$  dBi) is normally required for mm-wave antennae to overcome the high-attenuation at frequencies  $> 30$  GHz [27, 49].

On the other hand, patch antennae are very popular for wearable applications due to their low profile, light weight, and ease of integration into regular garments. It has been demonstrated that a ground plane with sufficiently large size on the other side of the patch antenna helps to reduce the backward radiation and minimise the effect of body proximity [11]. However, the implementation of a large ground plane also decreases the operating bandwidth (BW) of antennae. Furthermore, the gain and operating BW of a patch antenna is also limited by its geometry as well as the existence of surface wave and harmonic waves. Therefore, employing an EBG as the antenna's ground is a promising solution to suppress the surface wave and improve the antenna's performance.

Moreover, flexibility is essential for wearable devices since they are required to conform to the curved surfaces of the human body and provide softness for comfortable wearing.

However, to the best of our knowledge, there is no published literature on using flexible EBG to enhance the performance of wearable antennae at mm-waves.

Therefore, this chapter will propose a novel design of a uniplanar-compact (UC) EBG. The unit cell of the EBG has a fractal design with a self-similar window-like structure, which can be easily fabricated with easily accessible techniques at mm-scale. To optimise the design, the performance of the EBG is investigated by varying its geometrical parameters in HFSS. Next, a design of coplanar-waveguide (CPW) antenna will be presented, which is used to evaluate the performance of the proposed EBG. Following that, a fabricated prototype of the EBG serving as a high-impedance surface (HIS) will be integrated with the CPW antenna. The performance of the EBG-backed CPW antenna in terms of the reflection coefficient ( $S_{11}$ ) magnitude, surface current distribution and radiation pattern will be examined. Finally, the performance of the EBG-backed CPW antenna under bending and on-body scenarios will be reported and discussed.

## **5.2. Proposed Electromagnetic Bandgap Structure**

As presented in Chapter 3, a number of different EBG structures have been realised on dielectric substrates for improving the performance of microwave antennae. In [79, 80], a double concentric square EBG is designed to increase the gain and reduce the backward radiation of coplanar waveguide (CPW) antennae at 2.45 and 5.8 GHz. However, the ring design narrows the operating bandwidth of the antenna. An EBG developed from Moore space-filling (MSF) curve is proposed to increase the bandwidth of CPW-fed slot antenna [86], and decrease mutual coupling between the patch antennae [87]. However, this EBG geometry is inherently complex, which presents challenges to its fabrication at millimetre-scale for mm-wave applications.

In this section, an EBG with simple-to-fabricate fractal design will be presented based on selected materials. The frequency ranges of interest are in the mm-wave and quasi-mm-wave bands from 20 to 40 GHz, which cover the unlicensed ISM band (24 GHz), and two candidate frequencies for 5G cellular networks (28 and 38 GHz). The design starts with evaluating the performance of one unit cell of the EBG, and then extends to that of an EBG cell array. Both simulated and measured results of the proposed EBG structure will be presented and discussed.

### 5.2.1. Design of the EBG

#### 5.2.1.1. Material selection and fabrication process

As presented in Chapter 4, the substrate for this design is a soft and flexible plain-woven polyester fabric (sample type 5) as it provides a relatively smooth surface for attaching the conductive layer. As previously shown in Table 4.2, the dielectric constant ( $\epsilon_r$ ) and loss tangent ( $\tan \delta$ ) of this substrate material characterised by the hybrid-TL method are 2.2 and 0.004, respectively. This sample type is thermally bonded with four layers of thin uncoated polyester fabrics (type 3 in Table 4.2). Due to limited available facilities (e.g. the lack of access to a calibrated flatbed heat press), a domestic steam iron (Philips NI-P300T) was used to fabricate sample type 5 manually. This iron has a maximal power of 1,780 W, and a temperature ranges from 80 to 200 °C. There is one rotator on the iron to choose a suitable temperature for ironing different types of fabrics, and the temperature set for this purpose was between silk and wool (~160 °C) as shown in Figure 5.1. To fabricate sample type 5, a piece of thermal bonding film was inserted between 2 layers of polyester fabrics (see Figure 5.2(a)) and the top surface of the fabric was ironed until the bonding material had totally melted (the steam function was not used). Similarly, the opposite side of the sample was ironed until no air bubbles between polyester layers were visible. This process was repeated until all 4 layers of polyester were bonded together (see Figure 5.2(b)). The pressure applied on the iron was similar to that used for regular ironing. However, it should be mentioned that the above fabrication process serves only as a guideline, and the actual resulting substrate could vary with the type of fabric and thermal bonding film used.



**Figure 5.1. Domestic steam iron (Philips NI-P300T) for bonding fabric materials.**

On the other hand, the choice of the conductive material is a trade-off between the current fabrication techniques and the flexibility of materials. The best conductors to be used for

wearable applications should be conductive fabrics or conductive inks. However, there are still a technical challenge to fabricate millimetre-scale patterns with either type of conductors with the required accuracy for mm-wave applications.

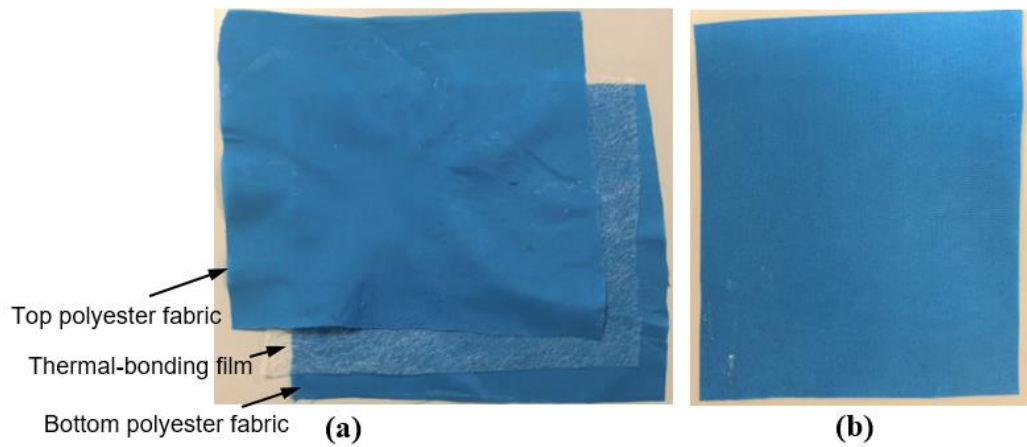


**Figure 5.2. Fabrication of sample 5: (a) a thermal-bonding film sandwiched between two polyester fabrics; and (b) a finalised four-layer polyester fabric.**

For conductive fabrics, the thicknesses of most conductive yarns are between 0.2–0.5 mm [11], which is in the same order as the geometric dimensions of mm-wave conductive patterns. Besides, limited by the existing fabrication techniques, the finest line width that can be realised with conductive fabrics is 0.4 mm with an accuracy of  $\pm 0.15$  mm [21, 22]. Figure 5.3 shows several slots and strips with different widths laser-cut from a conductive fabric made of extremely fine polyester fibres ( $\sim 0.4$  mm). However, the sample clearly shows that there are some extra fibres left on the cut patterns, which will alter the RF performance of the fabricated patterns. Furthermore, the width for the finest 0.4-mm strip is also uneven, which may due to the softness of the fabric.

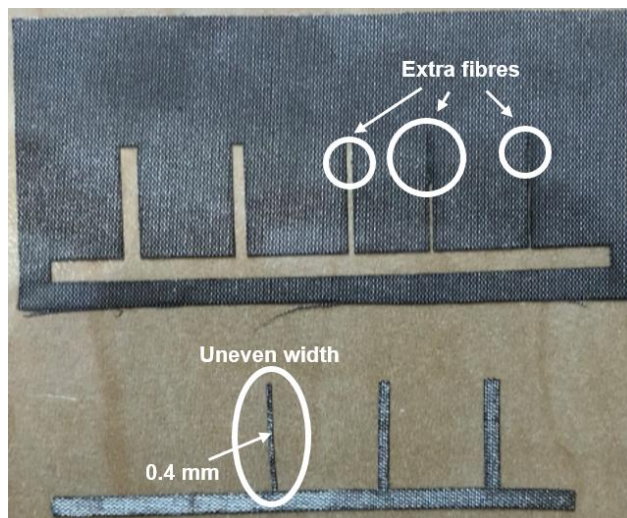


**Figure 5.3. Laser-cut slots and strips on conductive fabric.**

Printing conductive patterns with silver inks is an alternative option to overcome the aforementioned problems when using conductive fabrics. However, it requires expensive material printers (e.g. Dimatix) to achieve controllable geometrical accuracy for mm-wave applications. Besides, due to skin depth issue at RF, in order to meet the minimal conductive-layer thickness for antennae, depositing silver inks at the same position multiple times is required. However, this printing feature is not available in most common printers.

Therefore, in this thesis, laser-cut conductive patterns out of copper foil were used instead. A thin layer of copper foil (thickness: 0.07 mm) with adhesive backing was firstly attached on the polyester fabric substrate. Then, the desired pattern was laser-cut using a Trotec SpeedMaker 1300 MOPA pulse fibre laser machine, and excess copper is removed, as illustrated in Figure 5.4. Unfortunately, due to commercial confidentiality, details of the parameters used by the laser machine to fabricate the conductive patterns are not available for publication. The best geometrical accuracy that this technique can achieve is  $\sim 10 \mu\text{m}$  while maintaining the flexibility of the created structure [21]. A magnified view of the laser-cut conductive patterns under an optical microscope is illustrated in Figure 5.5. It can be seen that the edge of the designed shape is well cut, and no distortion can be observed. Therefore, the quality of the RF performance of laser-cut prototypes can be secured. In addition, unlike most fabrication processes for similar applications where the metallic parts are first cut and then attached onto the fabric substrates, the aforementioned process for this work secures the relative positions of the designed conductive patterns and avoids the shape distortions that may occur when transferring the cut patterns to the substrate.

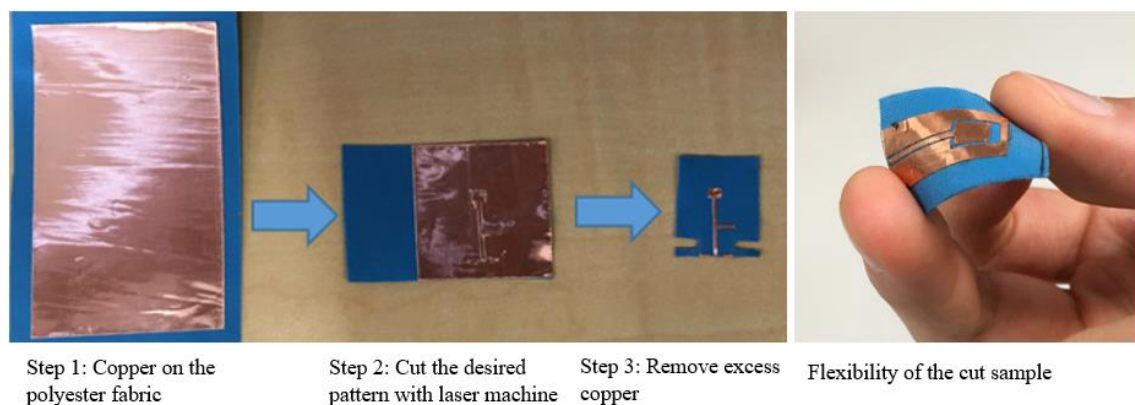


**Figure 5.4. Laser-cut conductive patterns from copper foil.**

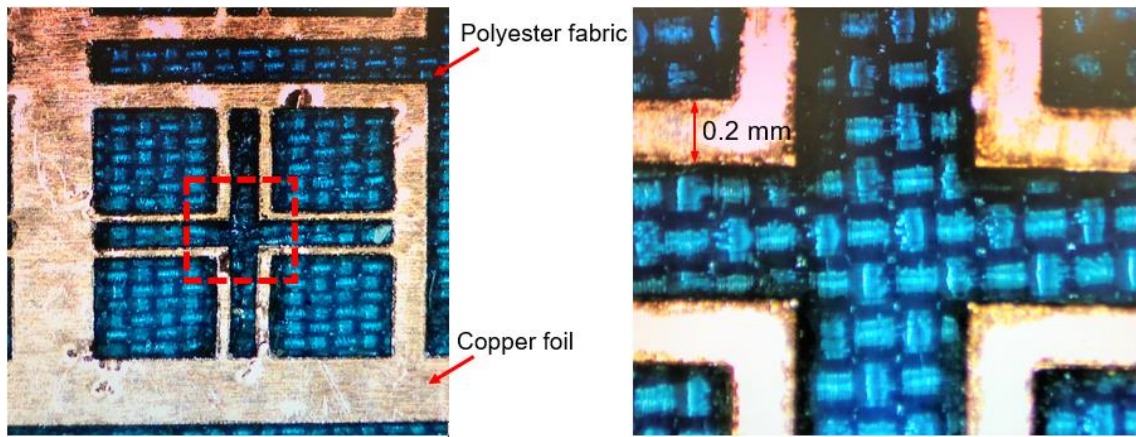


**Figure 5.5. Laser-cut conductive patterns under an optical microscope.**

### 5.2.1.2. EBG design

As introduced in Chapter 3, EBG can suppress the propagation of surface waves within certain frequency ranges, also referred to as the *stopbands* of the EBG. At frequencies below resonance, the EBG surface is inductive and supports TM waves, while at above resonance, the EBG surface is capacitive and supports TE waves. At resonance, the EBG exhibits high surface impedance that prevents wave propagation. Therefore, the EBG can generally be modelled as a *LC* resonant circuit, whose *L* and *C* values are determined by the geometry and dimensions of the unit cell.

The design of the EBG begins with one unit cell, as illustrated in Figure 5.6(a). The strips contribute inductance *L* while the gaps between strips contribute capacitance *C*. Besides, the conductive EBG pattern results in a shunt capacitance seen from the conductive layer, e.g. antenna, on the opposite side of the substrate. The equivalent *LC* circuit of one unit cell is shown in Figure 5.6(b).

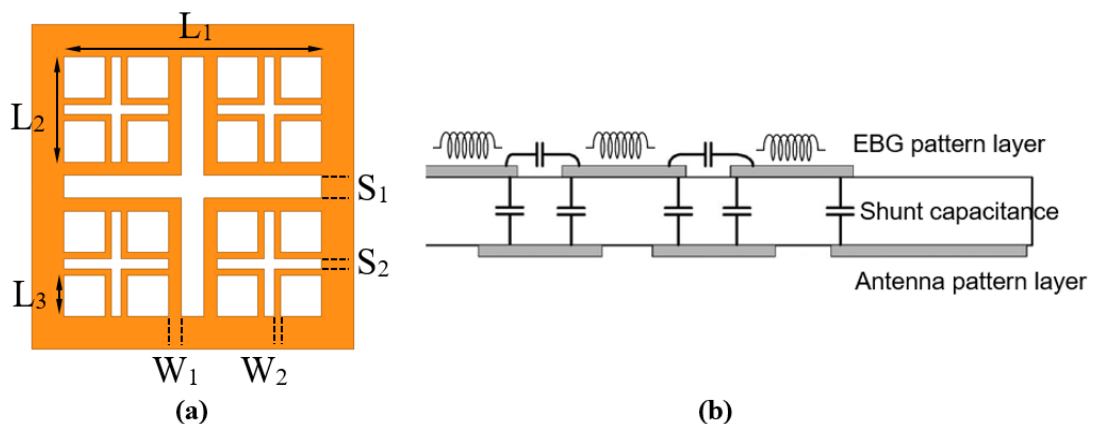


**Figure 5.6. Proposed EBG: (a) geometry; and (b) equivalent circuit of one unit cell.**

The unit cell features a fractal design with self-similarity and space-filling properties which enable the EBG to achieve wide bandwidth and compact geometry. As can be seen, 1 square unit cell (first iteration) of length  $L_1$  has 4 smaller squares of length  $L_2$  (second iteration), each of which has 4 even smaller squares of length  $L_3$  (third iteration). There can be more nested levels, with each level increasing the bandwidth of the EBG. In this thesis, 3 nested levels are sufficient to realise a bandwidth that spans the frequency range of interest from 20 to 40 GHz as shown in Figure 5.6(a).

The proposed EBG has three stopbands at 24, 28, and 38 GHz, which correspond to the resonant frequency ( $f_0$ ) to determine the lengths  $L_1$ ,  $L_2$  and  $L_3$  of the unit cell (collectively referred to as dimension  $\lambda_{EBG}$ ), respectively. Therefore, for the proposed EBG:

$$f_0 = \frac{c}{\lambda_L \sqrt{\epsilon_r}} \quad (5.1a)$$

$$\lambda_{EBG} = \frac{\lambda_L}{2} \quad (5.1b)$$

where  $c$  is the speed of light, and  $\lambda_L$  is the wavelength of the substrate's cut-off frequency to obtain  $\lambda_{EBG} = \{L_1, L_2, L_3\}$ , which are fine-tuned in HFSS to achieve optimal performance.

To initially simulate the bandgap characteristic of the proposed EBG, three unit cells are organised in series with a 50- $\Omega$  microstrip line (ML) positioned on the opposite side of the substrate (see Figure 5.7). The detailed explanation of this technique was presented in Chapter 2 [36]. The magnitude of the transmission coefficient ( $S_{21}$ ) of the ML is then examined in HFSS with the expectation that wave transmission will be blocked within the bandgap range.

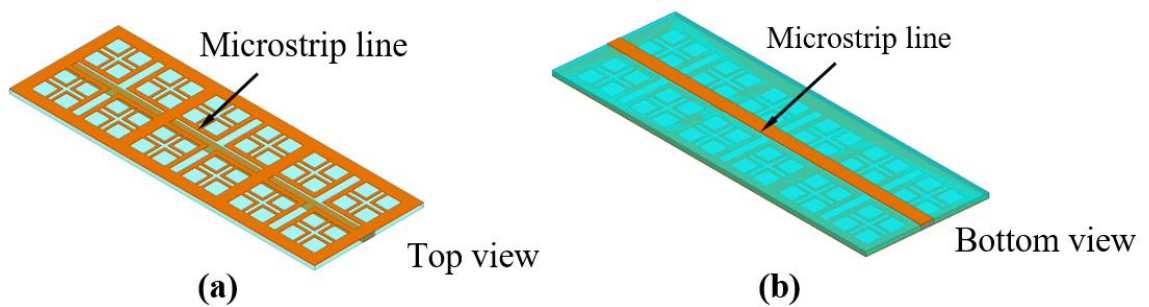


**Figure 5.7. Microstrip line with three unit cells EBG: (a) top view; and (b) bottom view.**

In Figure 5.6(a), the dimensions  $L_1$ ,  $L_2$  and  $L_3$  are initially obtained using (5.1), which are then fine-tuned by varying  $S_1$ ,  $S_2$ ,  $W_1$  and  $W_2$  in HFSS. The simulated results of the  $S_{21}$  for each value of the above parameters are plotted in Figure 5.8. It can be seen that varying

$S_1$  and  $W_1$  can impact the magnitude of the insertion loss whereas varying  $S_2$  and  $W_2$  can shift the resonant frequency of the EBG.

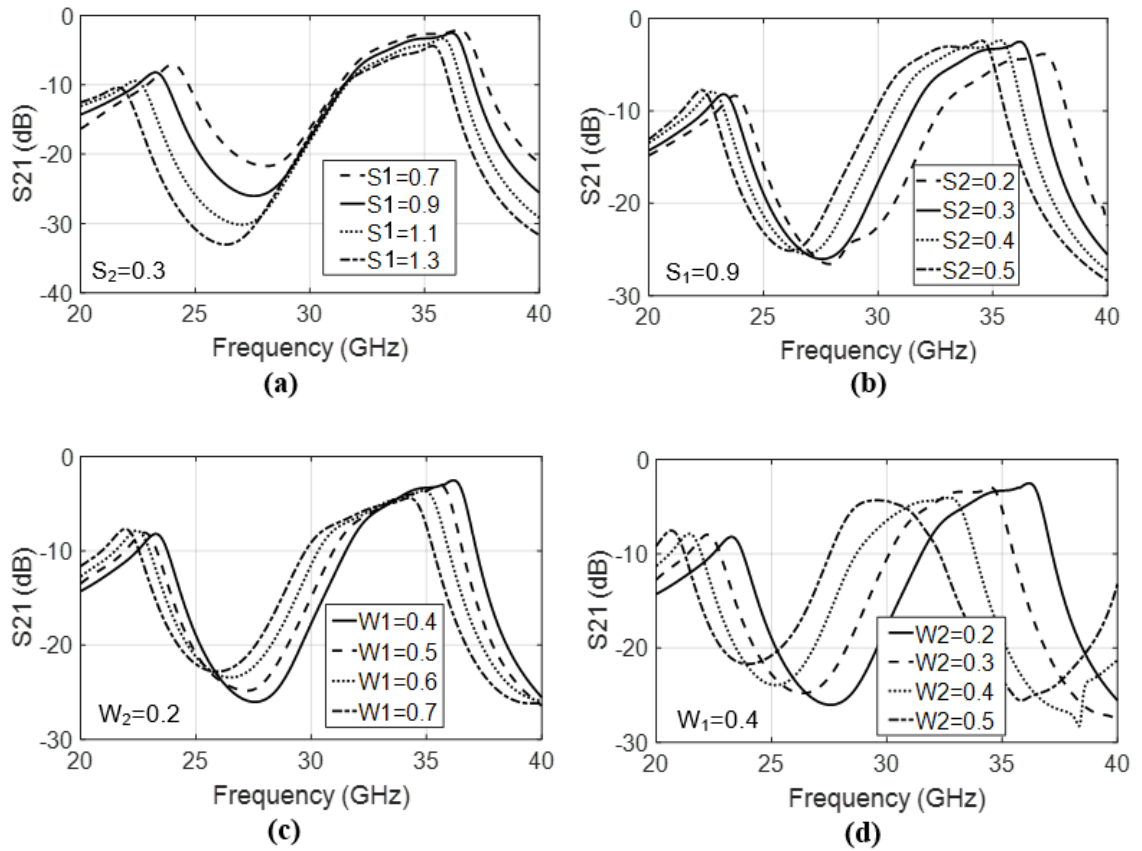


**Figure 5.8. Simulated magnitude of transmission coefficient ( $S_{21}$ ) for different values of: (a)  $S_1$ ; (b)  $S_2$ ; (c)  $W_1$ ; and (d)  $W_2$ . In each sub-figure, other dimension values are maintained as shown in Table 5.1. The unit is in mm.**

Table 5.1 lists the final values for the 7 aforementioned EBG dimensions to achieve an insertion loss  $< -20$  dB at the desired resonant frequencies (24, 28, 38 GHz), and  $< -10$  dB in the frequency range of interest (from 20 to 40 GHz), as plotted with solid line in Figure 5.8 with solid line. The width of the frame is 1 mm.

**Table 5.1. Dimensions of one unit cell of the proposed EBG (unit: mm).**

$L_1$	$L_2$	$L_3$	$W_1$	$W_2$	$S_1$	$S_2$
8.2	3.25	1.275	0.4	0.2	0.9	0.3

Furthermore, the current flow of one unit cell is simulated and plotted in Figure 5.9. It shows that the currents are excited around the loops generated by the second iteration at 28 GHz ( $L_2$ ), and more current flow is concentrated around the small loops ( $L_3$ ) generated

by the third iteration at 38 GHz. This proves the above design that lengths  $L_1$ ,  $L_2$  and  $L_3$  are corresponding to three resonant frequencies of 24, 28 and 38 GHz, respectively.

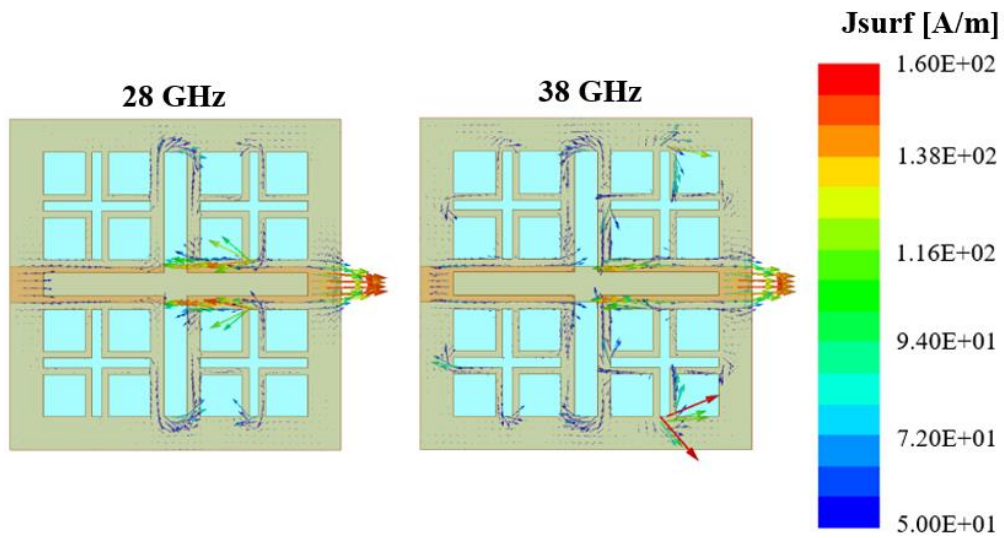


**Figure 5.9. Simulated current flow of one unit cell.**

Figure 5.10 shows a prototype of the proposed EBG with  $3 \times 3$  unit-cells fabricated on a polyester fabric substrate by laser-cutting. The fabricated sample measures  $28 \times 34 \text{ mm}^2$ . The extra 5 mm length at the bottom of the EBG is for interfacing with the end-launch connector for measurements.

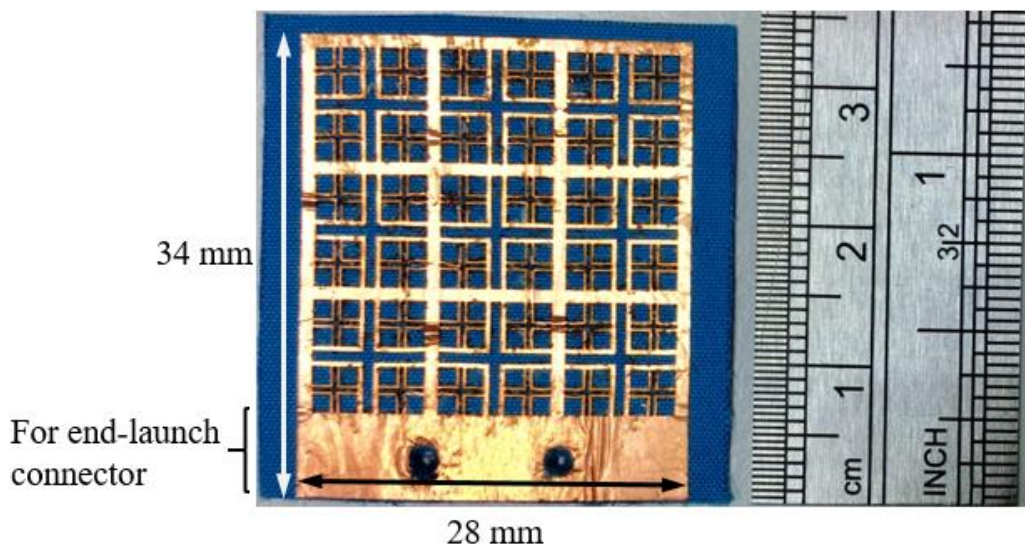


**Figure 5.10. EBG with  $3 \times 3$  unit-cells fabricated on polyester fabric substrate.**

### 5.3. Design of Coplanar Waveguide Antenna

To evaluate the performance of the proposed EBG, a fabric substrate version of the low-profile CPW antenna proposed in [113] is implemented.

This type of antenna is chosen because it has a slot design similar to the proposed EBG. Besides, unlike the dipole and patch structures that are simpler but with much narrower bandwidth, the coplanar design ensures a wide operating BW ( $> 20\%$  with the magnitude of reflection coefficient  $S_{11} < -10$  dB), and thus is more suitable for evaluating the performance of the proposed wideband EBG.

The geometry of the designed CPW antenna is illustrated in Figure 5.11(a). The antenna consists of a radiating patch, a 50- $\Omega$  CPW-feed line and a ground plane (GND) that surrounds the radiating patch and feed line. The wideband characteristic of the antenna is determined by the size of the radiating patch ( $L_{A3}$  and  $W_{A3}$ ) and the gap between the patch and the edge of the GND ( $G_1$ ). After fine tuning in HFSS, the final dimensions that enable the antenna to achieve optimal  $S_{11}$  are listed in Table 5.2.

**Table 5.2. Final dimensions of the CPW antenna (unit: mm)**

$L_{A1}$	$L_{A2}$	$L_{A3}$	$W_{A1}$	$W_{A2}$	$W_{A3}$	$W_{A4}$	$G_{A1}$	$G_{A2}$
10	5	4	20	7	5	0.9	0.5	0.3

The antenna is similarly fabricated by laser cutting on copper foil and using the same polyester fabric substrate as the one used for the EBG. One prototype of the CPW antenna is shown in Figure 5.11(b) with outer dimension ( $W_{A1} \times L_{A1}$ ) of  $10 \times 20$  mm<sup>2</sup>. The side view of the antenna is illustrated in Figure 5.11(c). A 2.92-mm end-launch connector from Southwest Microwave is attached to the end of CPW feed line for interfacing the antenna with a measurement device. The feed line has a length of 10 mm to avoid wave reflection impact due to the connector, and is tapered at the end to increase the inductance at the joint, thereby achieving better impedance matching and minimising the transition loss between the antenna and connector.

The antenna measurements are made by Anritsu S820E from 20–40 GHz. The simulated and measured magnitudes of reflection coefficient ( $S_{11}$ ) for the CPW antenna are shown in Figure. 5.12. It generally shows a broad agreement between the simulated and measured results, except at  $\sim 22$  and 36 GHz. This variation may be due to unknown RF properties of the adhesive layer of copper foil or the interface section of end-launch connector that are not accounted for in simulation. The antenna shows a  $-10$  dB

bandwidth of 37.6% and 4.3% from 20–29.26 GHz, and from 35.12–36.66 GHz, respectively.

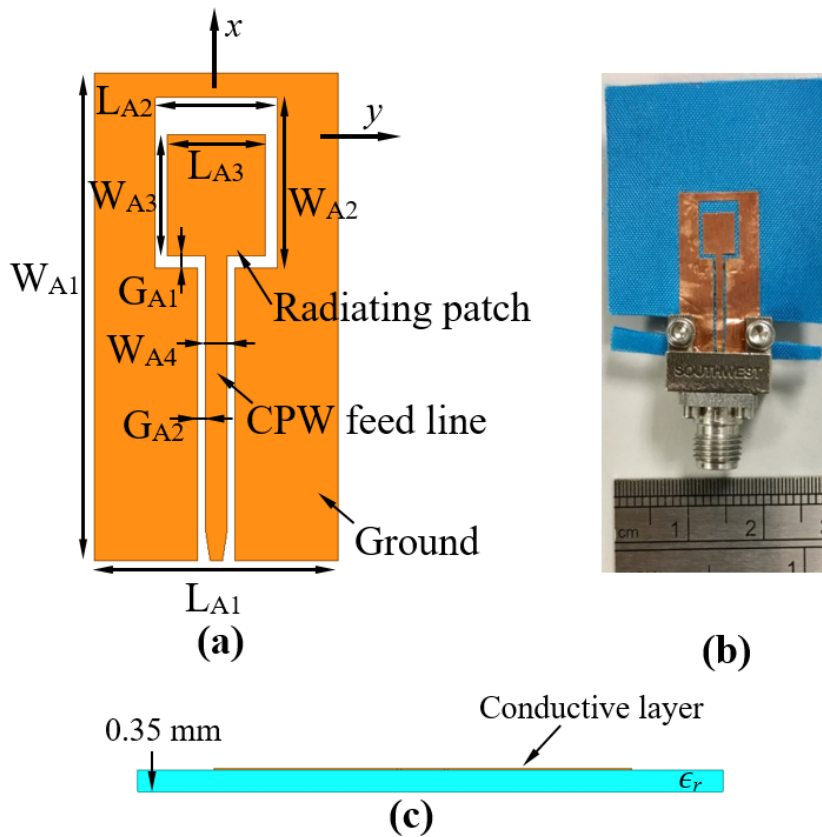


Figure 5.11. CPW antenna: (a) geometry; (b) fabricated prototype; and (c) side view.

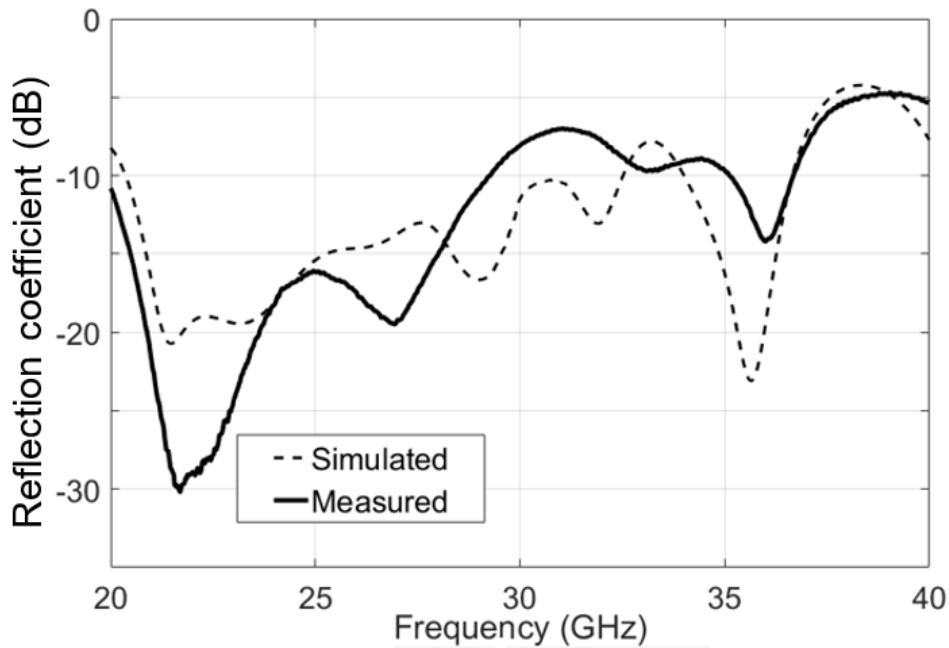
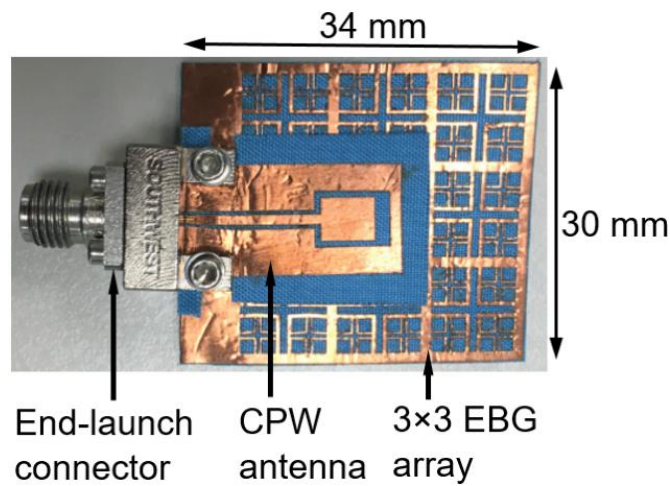


Figure 5.12. Simulated and the measured  $S_{11}$  of the fabricated CPW antenna.

## 5.4. Integration of EBG with the CPW antenna

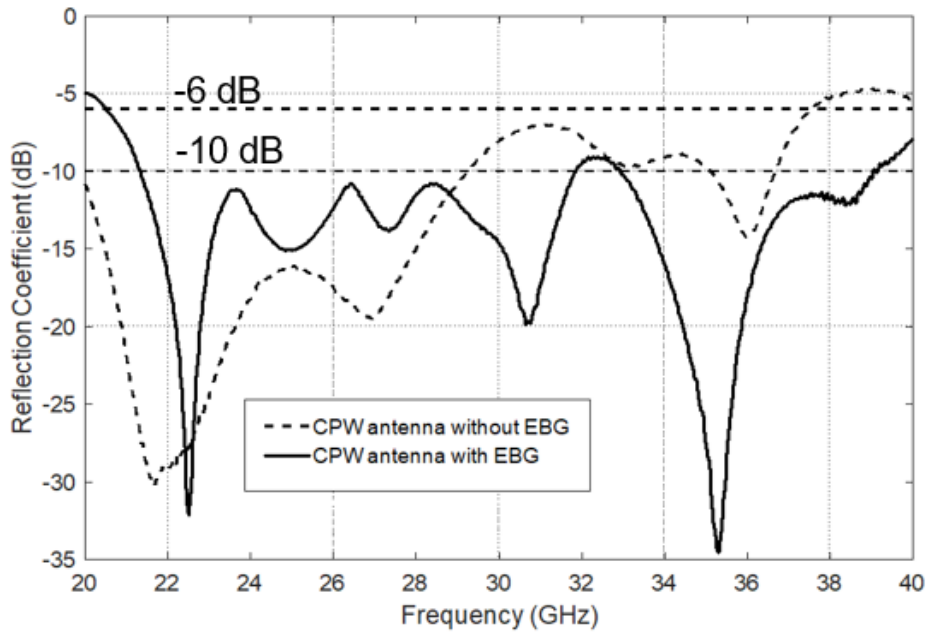
As discussed in previous chapters, the EBG serves as an HIS to improve the performance of low-profile antennae by controlling in-phase plane wave reflection and suppressing the surface waves. Moreover, it is expected that backward radiation of the wearable antenna can be reduced by integration with the EBG.

Figure 5.13 shows the EBG-backed CPW antenna mounted on an end-launch connector. The CPW antenna is carefully attached onto the EBG by thin double-sided tape. The tape is placed on the exposed fabric part of the EBG (away from the conductive square patterns) to minimise the tape's influences on the antenna's performance. The finalised geometry of the EBG-backed antenna is  $28 \times 34 \times 0.9$  mm, which results in an electrical size of  $2.61 \times 3.18 \times 0.08 \lambda_0$ , where  $\lambda_0$  is the free-space wavelength at 28 GHz.



**Figure 5.13. Fabricated EBG-backed CPW antenna.**

The measurements are performed in an RF anechoic chamber with the Anritsu S820E as introduced in Chapter 2. The measured magnitude of  $S_{11}$  of the antenna with and without the proposed EBG is plotted in Figure 5.14. A further comparison of their bandwidth performance is presented in Table 5.3. It is observed that the EBG has only slightly shifted the antenna's resonances while significantly increased the magnitude of  $S_{11}$  at its resonances. The slight detuning of their resonant frequency may be attributed to some mutual coupling between conductive traces that are very close to each other. Besides, the antenna's  $-10$  dB bandwidths are widened to 40% and 17% after introducing the EBG at 24/28 GHz, and 38 GHz, respectively. Notably, the frequency band of 38 GHz that was not originally covered by the antenna's bandwidth, is now included in the bandwidth of the EBG-backed antenna. Furthermore, the  $-6$  dB impedance bandwidth also increases from 61% to 64.4%.



**Figure 5.14. Measured magnitude of reflection coefficient of the CPW antenna with and without the EBG in free space.**

**Table 5.3. Bandwidth comparison of the CPW antenna with and without the EBG.**

	Without EBG	With EBG
-10 dB bandwidth	20–29.26 GHz (37.6%)	21.33–31.86 GHz (40%)
	35.12–36.66 GHz (4.3%)	32.94–39.14 GHz (17%)
-6 dB bandwidths	20–37.52 GHz (61%)	20.52–40 GHz (64.4%)

Next, the simulated surface current distribution of the CPW antenna with and without EBG at 24, 28 and 38 GHz (see Figure 5.15) is compared. It should be noted that the fabric substrate of antenna was configured in HFSS to be ‘transparent’ and only its outline is shown, so that the surface current distribution over the EBG copper surface under the substrate can be visible.

It is observed that with an EBG, the current distribution of the CPW antenna has only slightly changed. Besides, there exist excited currents in the EBG, which enables it to act as a radiating element. As will be shown later in Section 5.5, at higher frequencies, backward radiation suppression is worse as more currents are excited, but it is still 75% less than that of the antenna without EBG. Furthermore, with increasing frequency, the presence of more excited currents in the EBG indicates a higher coupling with the antenna, which improves the impedance bandwidth of  $S_{11}$  at higher frequency bands.

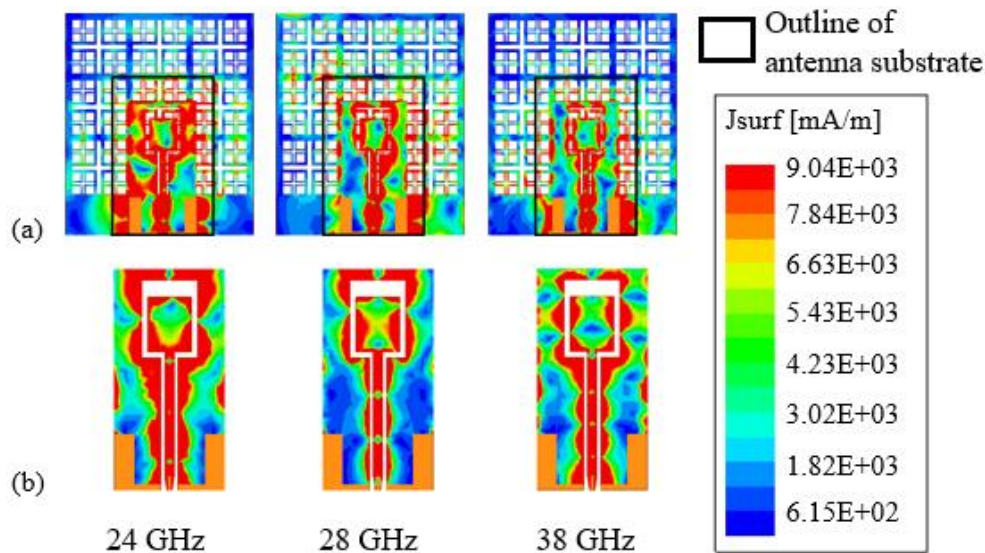


**Figure 5.15. Current distribution of the CPW antenna (a) with; and (b) without the EBG at 24, 28 and 38 GHz.**

Finally, the radiation pattern of the CPW antenna with and without the EBG is measured in the anechoic chamber at 24, 28 and 38 GHz. Figure 5.16 illustrates the setup for measuring the radiation pattern. The antenna under test (AUT) is mounted on a rotatable stand placed 45 cm away from the source horn antenna with a 15 dBi gain. The measurement resolution is  $2^\circ$  per step and the results are plotted in Figure 5.17.

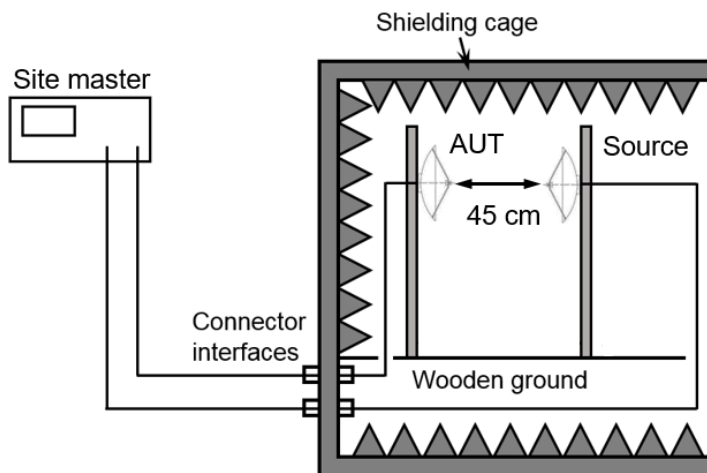


**Figure 5.16. Setup for measuring radiation patterns.**

Generally, the radiation patterns of the CPW antenna without EBG shows a fairly omnidirectional pattern in both  $E(xz)$ - and  $H(xy)$ - planes at all three frequencies. However, with EBG, the antenna's backward radiation is significantly reduced by at least 7 dB at 38 GHz and approximately by 15 dB at 24 and 28 GHz, indicating the effectiveness of the EBG in reducing the amount of radiation directed towards the human body.

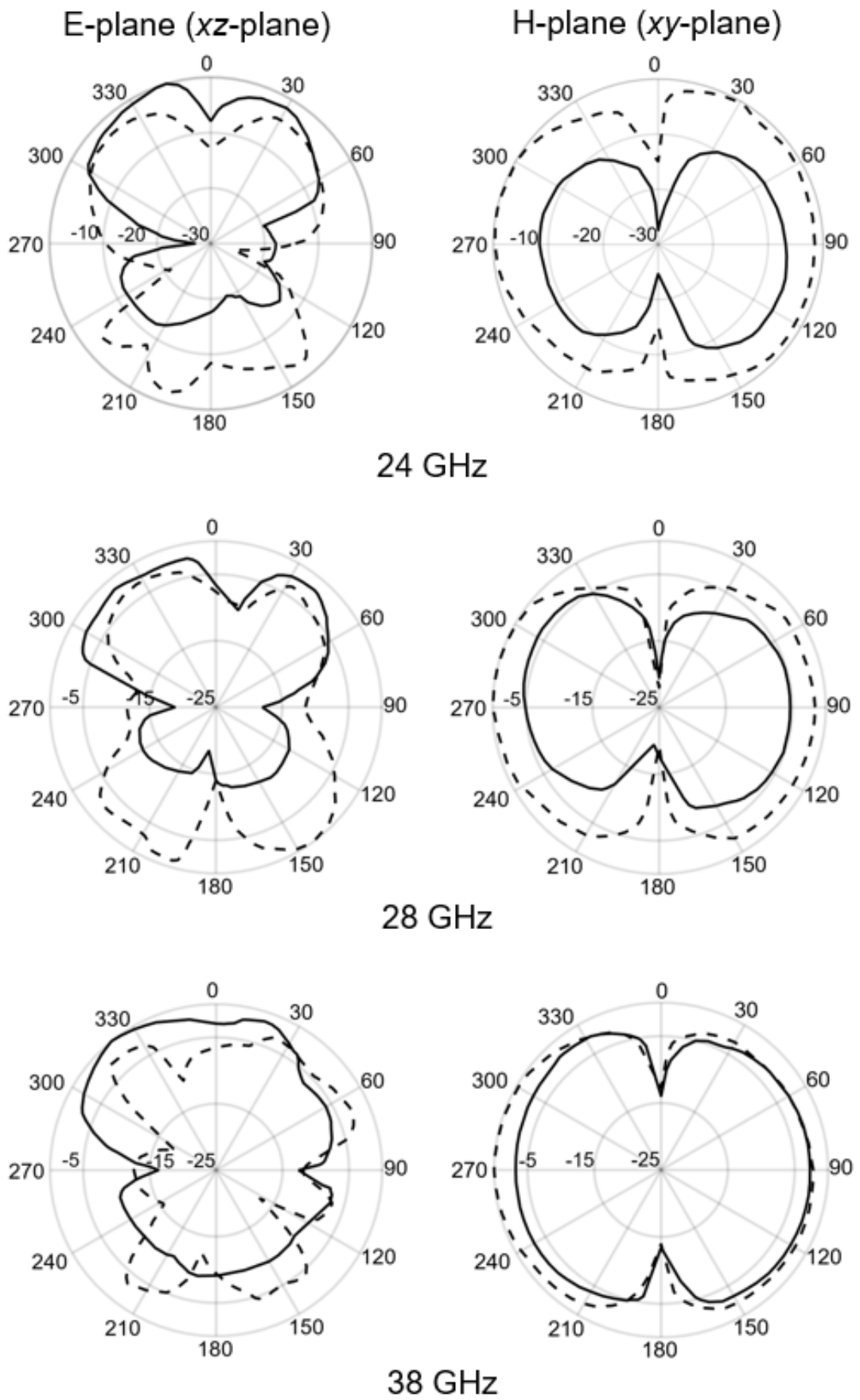


**Figure 5.17. Measured radiation patterns for the CPW antenna with EBG (solid line) and without EBG (dashed line) at 24, 28 and 38 GHz in free space.**

The realised gain of the EBG-backed CPW antenna is 8.4, 7.9 and 10.3 dBi at 24, 28 and 38 GHz, respectively, as compared to 6.4, 6.3 and 7.4 dBi of the CPW antenna without the EBG. The EBG improves the antenna's radiation outwards and away from the human body. This proves that the EBG is acting as a HIS to enhance antenna gain through constructive interference due to in-phase reflection.

## 5.5. On-body Performance of the EBG-back CPW Antenna

There exist a number of problems when integrating wearable RF structures onto human bodies for effective wireless communications. One problem is that human body is fluid rich, possessing relatively high  $\epsilon_r$  and conductivity ( $\sigma$ ) [114], which will significantly affect the on-body antenna performances, such as decreased impedance bandwidth, detuned resonant frequency and reduced antenna gain. Moreover, to conform to the body curves, effects such as the bending of the fabric substrate will also alter the antenna's performance.

Therefore, it is essential to examine the performance of the EBG-backed CPW antenna under bending and on-body scenarios.

### 5.5.1. Bending performance

Considering the curvature and shape characteristics of the human body, it is difficult to assume the flat operating conditions for antennae in on-body applications. To emulate the bending due to body curves, the antenna is positioned on a rolled foam of 60 mm diameter with bending degree of  $\sim 30^\circ$ , emulating the forearm of an average adult (see Figure 5.18). The foam is made of polystyrene that exhibits a similar  $\epsilon_r$  to that of air. This is considered to be a reasonably severe test condition because the forearm is the thinnest body part where such antennae are often placed for wearable applications.

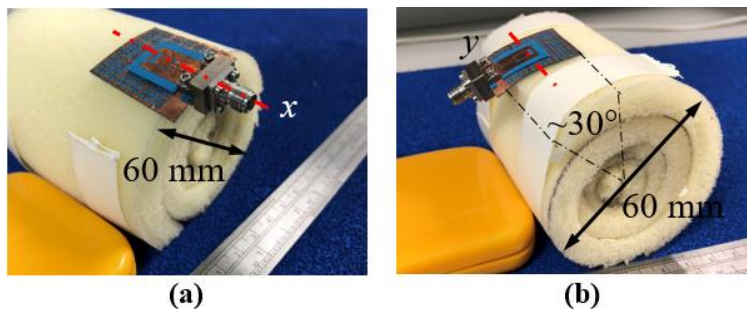


**Figure 5.18. Bending of the EBG-backed CPW antenna along (a)  $x$ ; and (b)  $y$  axes on a rolled foam.**

The measured magnitude of  $S_{11}$  when the EBG-backed CPW antenna is bent along  $x$ - and  $y$ -axis are plotted in Figure 5.19 and compared with that under no bending. As can be seen, the antenna under bending resonates at higher frequencies in all bands, and the  $S_{11}$  magnitude at  $\sim 35$  GHz is decreased. This is because the bending reduces the antenna's resonance length, and thus the resonant frequencies  $f_0$  shift up as well as the input matching bandwidth. However, the EBG-backed antenna can still achieve reasonable  $S_{11}$  ( $< -10$  dB) at 24, 28 and 38 GHz. Since more upwards shifting of  $f_0$  will occur with a larger degree of bending [115], it can be concluded that the EBG-backed CPW antenna will maintain its wideband characteristic when positioned at other parts of the human body.

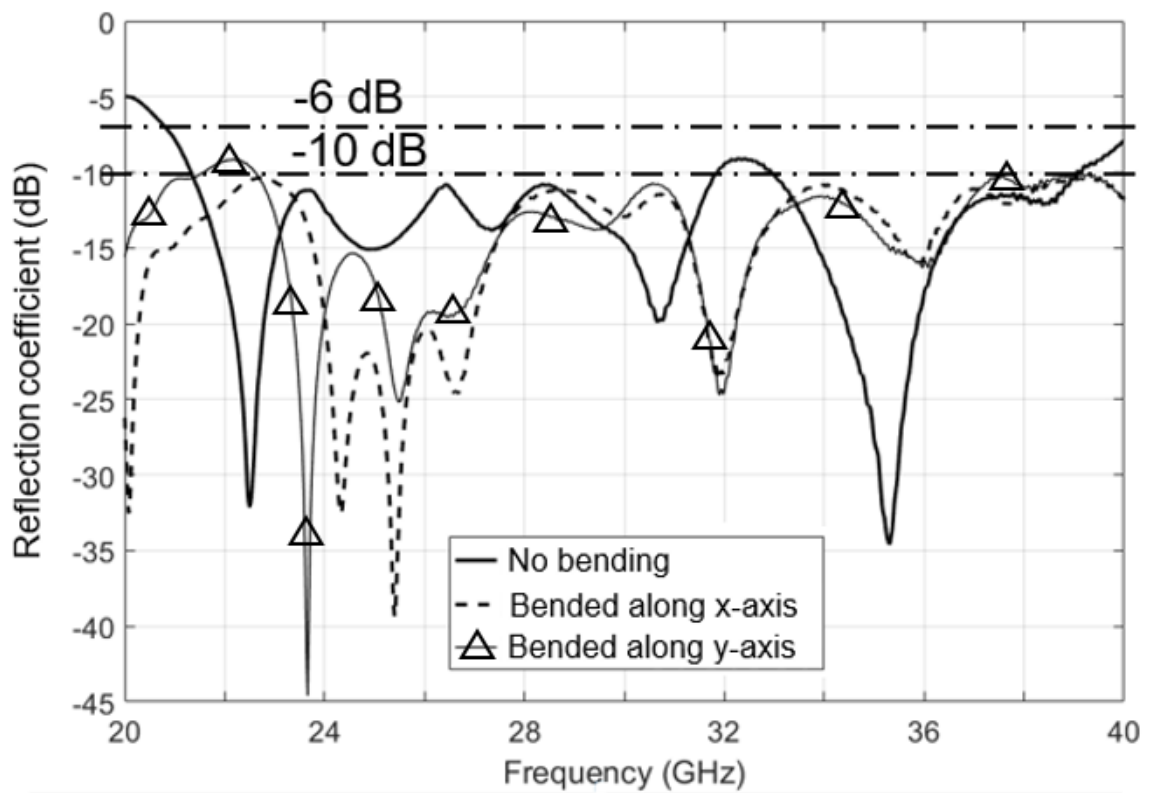


**Figure 5.19. Measured magnitude of the reflection coefficient along  $x$  and  $y$  axes.**

### 5.5.2. On-body performance

For wearable applications, it is expected for the antennae to maintain their performance when integrated with everyday clothing and come into proximity of human body. Therefore, the performance of EBG-backed CPW antenna is further evaluated on a human wearing a cotton sweatshirt and denim jeans. Three typical on-body positions are selected for this experiment: chest, forearm, and thigh, which can be considered as being performed under relatively flat, high bending, and low bending conditions, respectively.

The antenna is carefully attached to the aforementioned positions with thin double-sided tape (see Figure 5.20).

The measured  $S_{11}$  at all three positions are plotted in Figure 5.21. It shows that the  $S_{11}$  frequency response has been altered in comparison with that measured in free-space (see Figure 5.14). As expected, the antenna performs better when positioned on the chest and thigh where it is subject to less bending. On the other hand, the antenna on the forearm experiences more bending, and has its  $f_0$  shifted to higher frequencies, as previously observed on the rolled foam. However, the  $S_{11}$  has not been adversely affected and the EBG-backed antenna still largely maintains a wide operating bandwidth from 20–40 GHz.

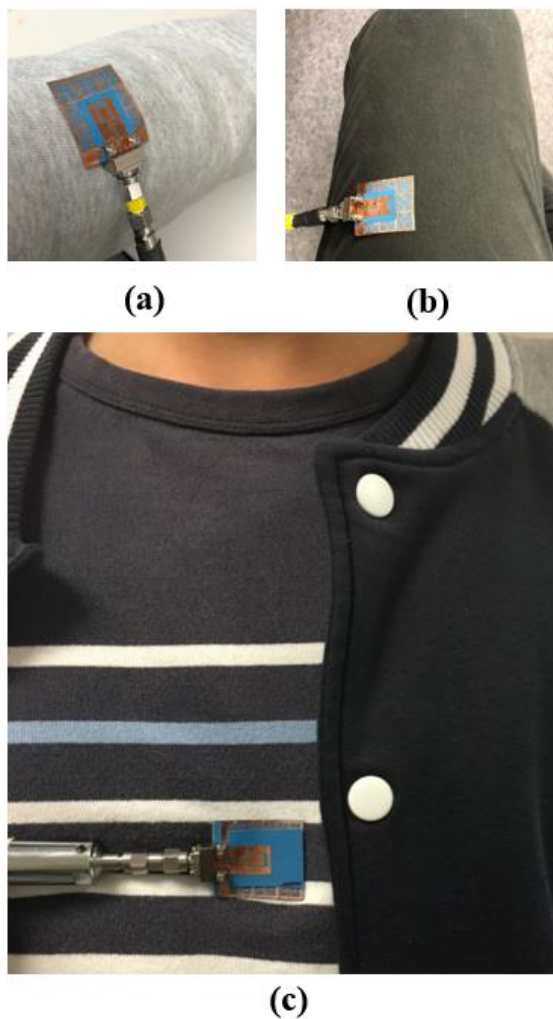


**Figure 5.20. EBG-backed CPW antenna attached on the (a) forearm; (b) thigh; and (c) chest.**

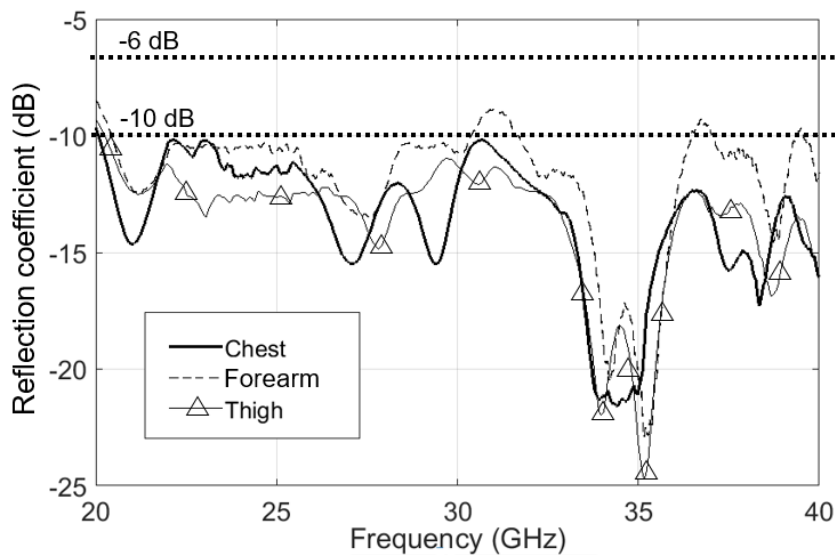


**Figure 5.21. Measured magnitude of  $S_{11}$  of the EBG-backed CPW antenna on human body.**

Furthermore, the radiation pattern of the EBG-backed CPW antenna is measured when it is attached to the forearm at the mid-frequency of interest at 28 GHz. As there is no commercialised body phantom available at this frequency band, this experiment was conducted with a person standing inside the anechoic chamber and wearing the antenna that points towards the source horn at a certain degree. One problem with not using a body phantom is that the person may move in the chamber, which makes the alignment between the transmitting and the receiving antenna difficult. Therefore, in order to minimise the accuracy error, the person had to keep still as long as possible in the chamber and measurements were repeated 5 times at each position step, and their average values plotted in Figure 5.22 and compared to that measured in free space (off-body).

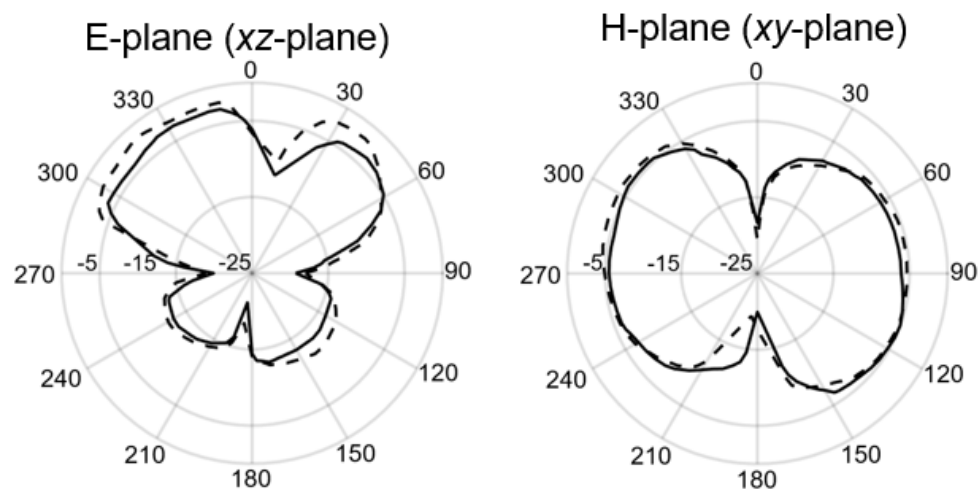


**Figure 5.22. Measured radiation pattern of the EBG-backed CPW antenna in free space (dashed line) and on-body (solid line) at 28 GHz.**

As observed, there is only a slightly distortion in the radiation pattern for on-body scenario, which proves that the antenna with proposed EBG is not highly sensitive to human body proximity. This is mainly because the antenna and EBG lengths (~3 cm) are much smaller compared to the perimeter (~20 cm) of the forearm. Hence, the bending degree is minor (~30°), which did not result in a significant change in the radiation patterns. Besides, the EBG is a high-impedance surface that also serves as a ground plane of the antenna, thus shielding it from the effects of the human body.

Finally, the antenna gain is measured using a method similar to that for radiation patterns. A transmitting antenna with 15-dBi gain is placed at 45 cm away from the body with its height levelled with, and maximal radiation direction pointing at, the on-body antenna. Table 5.4 compares the measured realised gain of the CPW antenna with and without EBG at 24, 28 and 38 GHz. It is clear that the gain of the CPW antenna without EBG is significantly lower than that measured in free space, which is due to the high fluid content of the human body. However, with EBG backing, the gain is only slightly reduced at 24 and 28 GHz, and decreased by up to 2.6 dB at 38 GHz. This is likely caused by the increased conductivity of the body at higher frequency, but the realised gains are still better than that without EBG at these frequency bands.

**Table 5.4. Realised gain of CPW antenna with and without EBG on human body (unit in dBi).**

Frequency	Chest	Forearm	Thigh
24 GHz	7.8 (1.5)	8.1 (2)	8.0 (1.8)
28 GHz	7.2 (1.7)	7.6 (1.8)	7.6 (1.5)
38 GHz	7.7 (0.9)	8.2 (1.4)	7.9 (1.7)

## 5.6. Summary

In this chapter, the design of a flexible fractal EBG for mm-wave wearable antennae was proposed. Firstly, the materials and the chosen fabrication technique for this work were compared and discussed. Secondly, the design of the EBG for both single unit cell and whole array were presented. The single unit cell has three iterations of squares that correspond to resonant frequencies of 24, 28 and 38 GHz, respectively. The dimensions of the EBG were first derived from theoretical formulas and then fine-tuned in HFSS to achieve optimal performance. The simulated current flow of one EBG cell at different

frequencies proves the operating mechanism of the proposed design. The bandgaps of the EBG were examined by evaluating the magnitude of  $S_{21}$  of a microstrip line, which is positioned on the opposite side of the EBG.

Next, a CPW antenna was designed to evaluate the proposed flexible EBG. Both the CPW antenna and the EBG were fabricated on the flexible polyester. The EBG was then integrated with the fabricated CPW antenna, acting as a HIS to improve the antenna's performance. The results show that the EBG-backed CPW antenna achieves a wider impedance bandwidth, reduced backward radiation and enhanced outwards gain as compared to that without the EBG over the frequency of interest.

Furthermore, the performance of the EBG-backed antenna was analysed under bending and on-body scenarios. The results show that the CPW antenna's resonance has only slightly shifted to higher frequencies while still maintaining its wideband characteristic. Besides, in the on-body scenario, the gain and radiation patterns of the EBG-backed antenna are not significantly altered. Therefore, the proposed EBG is a promising backing for mm-wave wearable antennae.

# Chapter 6

## Wearable Environmental Sensing Antennae over 5G Network

### 6.1. Introduction

One important application of wearable antennae is to integrate them as part of a body area network (BAN) system. Recently, BANs have drawn increasing attention from researchers due to their wide-ranging applications in domains such as healthcare, sports, and entertainment [10]. As a specialised form of wireless sensor networks (WSNs) deployed in the near space of human body, a BAN allows physiological sensors with intelligent processing and wireless communication functions to be placed near or implanted into humans for monitoring vital parameters such as body temperature, skin surface humidity, blood pressure and respiratory rate [116].

Clothing is obviously an ideal platform for deploying these sensors in proximity to the body. As introduced in Chapter 2, various types of sensors have been developed for BANs, including temperature and humidity sensors, stretch sensors, pressure sensors, and so on. However, unlike conventional rigid components, wearable applications require highly flexible sensors and antennae with structural integrity [26]. Therefore, there are a few requirements for these on-body sensors nodes. Firstly, they should be capable of sensing physiological or other body-related parameters, processing the sensed data, and wirelessly reporting the processed results to the system. Besides, these nodes need a certain amount of energy to keep them running for the purpose of continuous monitoring. Furthermore, these nodes should be relatively small and flexible, so that they can be integrated within regular garments, adhered to human bodies.

On the other hand, textile-based antennae have been extensively studied at microwave and more recently millimetre-wave (mm-wave) frequencies due to their flexibility to conform to human body and softness for comfortable wearing [11, 14, 21, 22]. It has been shown in literature that regular garment materials are well-suited for use as dielectric

substrates whereas the conductive parts can be constructed of thin metallic foils, conductive textiles or silver inks [11, 22, 27, 82]. These antennae have been successfully used in various BANs for RF communications. However, it is still an ongoing challenge to realize highly integrated, lightweight and ultra-low-power sensors for such wearable applications.

Due to the crowded microwave spectrum, mm-wave frequencies (28 and 38 GHz) have been allocated for the 5<sup>th</sup> generation (5G) cellular networks to access wider bandwidth and achieve faster transmission rate than previous microwave systems [49].

Therefore, in this chapter, a design of a sensing antenna is proposed, which can react to the temperature or humidity of its surrounding environment. The antenna is designed to operate at 38 GHz – a candidate frequency band for future 5G network, offering the possibility of data streaming between BANs and external devices over the ultra-fast and ubiquitous wireless links. Since the proposed structure itself serves as both a sensing and transmission unit, a more compact and low-profile wireless sensor can be realized than those with separate sensing and transmission units. Further, these wireless sensing structures operate mostly passively (event-triggered and respond by backscattering RF energy from some signal sources), thereby consuming less energy than conventional wireless sensors.

The geometry of the proposed antenna will be firstly presented in this chapter. Next, the dielectric constant ( $\epsilon_r$ ) of candidate substrates will be measured under different temperature and relative humidity (RH) levels with the hybrid-ML method in the climate test chamber. The antenna's response to the ambient environment will also be simulated based on the characterised  $\epsilon_r$ . Finally, the measured results of the sensing antenna will be discussed.

## **6.2. Design of the Sensing Antenna**

Wearable temperature and humidity sensors have been extensively investigated during the past few years. Various types of flexible temperature sensors have been reported for a number of electronic skin applications, including thermocouple sensors [117], thermos-resistance temperature sensors [118], and thermistor-transistor integrated sensors [119]. Some efforts were also made to improve the sensitivity of the sensors. For example, a temperature sensor is fabricated by an optimised graphene nano-walls on the flexible

polydimethylsiloxane (PDMS) [120], which is extremely sensitive to small variations of body temperature.

On the other hand, existing wearable humidity sensors are designed based on relating the changes in resistance or capacitance with humidity upon the absorption of moisture. In [121], a resistive humidity sensor is fabricated on textile poly-ethylene terephthalate (PET) monofilament. Since textile yarn is used as the substrate, it is easy to integrate the developed sensor into everyday garments. The sensing material is polyvinyl alcohol (PVA), which has a relatively linear resistivity-humidity response. In [122], a capacitive humidity sensor is presented, where an interdigital capacitor is inkjet-printed directly on the textile substrate. The fabric's moisture absorption increases the substrate's dielectric constant, thereby increasing the sensor's capacitance.

However, for the above wearable temperature and humidity sensors, investigating new and novel materials is normally involved, and a separate transmission unit is required for transmitting their sensed data. Due to limited space for positioning on-body devices, it will be beneficial if one unit can function as both the sensor and transmission unit.

As reviewed in Chapter 3, wireless sensing structures detect external signals either by the deformation of their mechanical structures or by the variation of the substrate's permittivity, where the latter is used by the sensing antennae proposed in this chapter.

Normally, these wireless sensing structures are in the form of patch antennae or *LC* resonant circuits. For example, an inkjet-printed RFID tag antenna was realised on the Kapton polyimide film with the ability of sensing ambient humidity [97]. However, the performance of this antenna is susceptible to human body effects, and thus not suitable for BAN applications. In this Chapter, such sensitivity of the antenna is leveraged as an advantage to design a humidity sensing antenna. Since the human body fluid behaves as a high dielectric constant material, the absorption of ambient moisture with the selected cotton fabric results in increased permittivity of the antenna's substrate, thereby shifting its resonant frequency.

### **6.2.1. Antenna's geometry**

This section presents the design of the sensing antenna. As mentioned in Chapter 4, two types of antenna substrate materials are used in this thesis: a customised polyester fabric (sample 5,  $\epsilon_r = 2.32$ , thickness  $h = 0.32$  mm) and a cotton fabric (sample 7,  $\epsilon_r = 1.83$ ,  $h =$

0.35 mm). The aforementioned values are measured in the climate test chamber with a well-controlled temperature (25°C) and relative humidity (RH) level (30%).

A microstrip patch antenna operating at 38 GHz is designed for each substrate. A patch design inherently exhibits a relatively narrow operating bandwidth, thereby increasing the quality-factor ( $Q$ ) and improving the sensitivity of the sensor. The design follows the formula (2.11) specified for the size of microstrip antennae introduced in Chapter 2, and the effective dielectric constant ( $\epsilon_{eff}$ ) of the substrate is obtained from Table 2.1.

An antenna model is setup in HFSS based on the derived theoretical values. However, since the designed antenna patch exhibits a complex impedance, an inductor-capacitor ( $LC$ ) matching circuit is normally desired. In order to avoid a difficult fabrication process (e.g. by introducing the lumped- $LC$  tuning circuit) while still maintaining the low-profile property of the microstrip antenna, an open-ended stub is utilised as the tuning circuit. The antenna is excited from the end of feed line, and thus can be easily integrated with other RF components. The finalised geometry for the antenna is shown in Figure 6.1, and the dimensions of each substrate type are listed in Table 6.1. Again, long and tapered feed line is implemented for this design to minimise wave reflection from the connector and improve impedance matching with the connector, respectively.

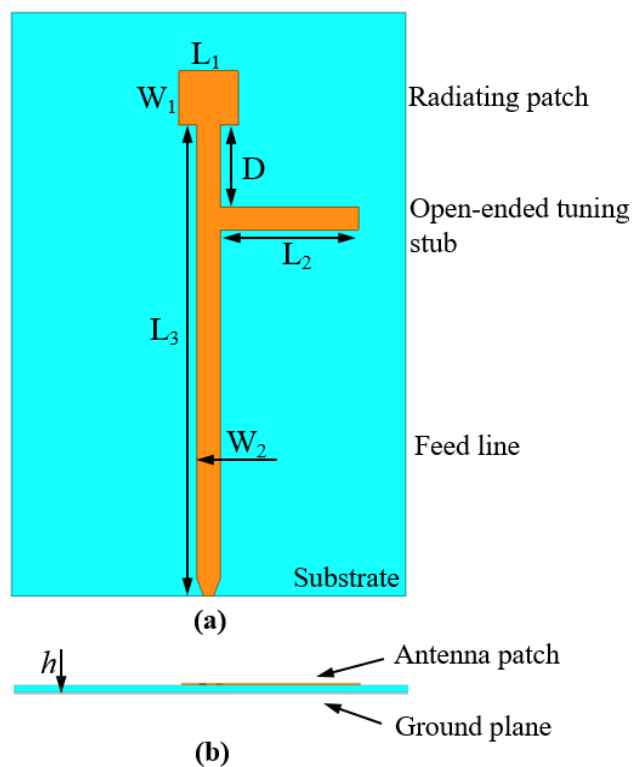


**Figure 6.1. Geometry of the microstrip antenna: (a) top view; and (b) side view.**

**Table 6.1. Values for the parameters of the microstrip antenna (unit: mm).**

Substrate	$h$	$L_1$	$L_2$	$L_3$	$W_1$	$W_2$	$D$
Sample 5	0.32	2.1	7	24.2	2.8	0.95	8.2
Sample 7	0.35	2.8	7	24.2	3	1.18	4.2

As shown in Table 6.1, the size for antennae operating at mm-wave frequencies is relatively small, and thus it will be relatively easy to find an area on the body where the surface is flat to mount and support the fabricated antennae, so that the distortion caused to the antenna's shape is minimal. Therefore, the frequency shift of the sensing antennae due to people's daily movements can be minimised.

### 6.2.2. Simulated results of the antenna

The simulation is performed for the antenna operating in both free space and on-body scenarios. The magnitude of reflection coefficients ( $S_{11}$ ) and radiation patterns for each condition are analysed in HFSS to ensure that the antenna performance will not be significantly altered by the proximity to the fluid-rich human body.

In the simulation, a three-layer human body phantom is employed under the antenna with a 1-mm air gap [26]. As illustrated in Figure 6.2, the phantom is a 40×30 mm laminate with a thickness of 44 mm, and consists of a 1-mm dry skin, 3-mm fat and 4-mm fat. The frequency-dependent electrical properties of the tissues at 38 GHz are retrieved from [114, 123] and listed in Table 6.2.

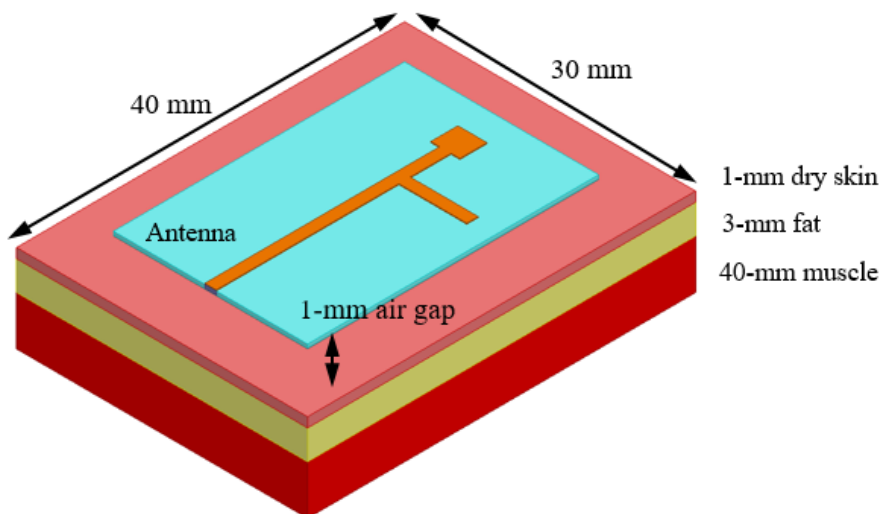


**Figure 6.2. Antenna on the body phantom.**

**Table 6.2. Electrical properties of body phantom at 38 GHz [114, 123].**

Tissue layer	$\epsilon_r$	$\tan\delta$	Conductivity $\sigma$ (S/m)
Dry skin	12.297	1.1941	31.043
Fat	3.4444	0.29331	2.1358
Muscle	41.823	1.0382	19.056

The simulated  $S_{11}$  of the antenna on polyester substrate and cotton substrate are plotted in Figure 6.3(a) and (b), respectively. As can be seen, for both substrates, the  $S_{11}$  magnitude in free space shows a sharp dip at resonance ( $\sim 38$  GHz), and thus is highly sensitive to any small variation in  $\epsilon_r$  of its substrate. For on-body scenario, the resonant frequency ( $f_0$ ) of both antennae are slightly shifted to a higher frequency, and magnitude of  $S_{11}$  is decreased. However, the  $S_{11}$  is still regarded as having relatively high selectivity for on-body scenario. It is note that the polyester fabric has a smaller loss factor than the cotton fabric, and thus a higher  $Q$  factor is observed for the antenna fabricated on the polyester substrate.

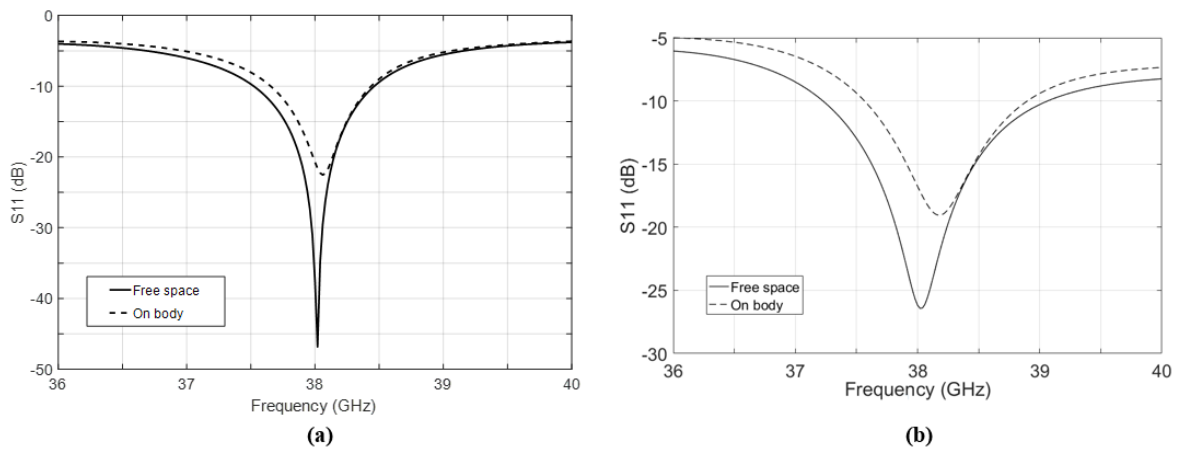


**Figure 6.3. Simulated magnitude of  $S_{11}$  for the antenna on (a) polyester fabric; and (b) cotton fabric.**

The simulated 3D radiation patterns for the antenna on polyester fabric and cotton fabric are presented in Figure 6.4 and Figure 6.5, respectively. Due to the ground plane on the opposite side of the substrate, the human body has limited influence on the antenna's radiation performance, and the gain of both antennae only slightly changed in proximity of the body phantom. A more detailed comparison between the simulated results for free-space and on-body scenarios are listed in Table 6.3.

**Table 6.3. Comparison between the results for free-space and on-body scenarios.**

	Polyester substrate		Cotton substrate	
	Free space	On body	Free space	On body
$f_0$ (GHz)	38.02	38.06	38.02	38.16
$Q$	900	252	172	95
Gain (dBi)	6.1172	5.7670	6.2435	6.3984

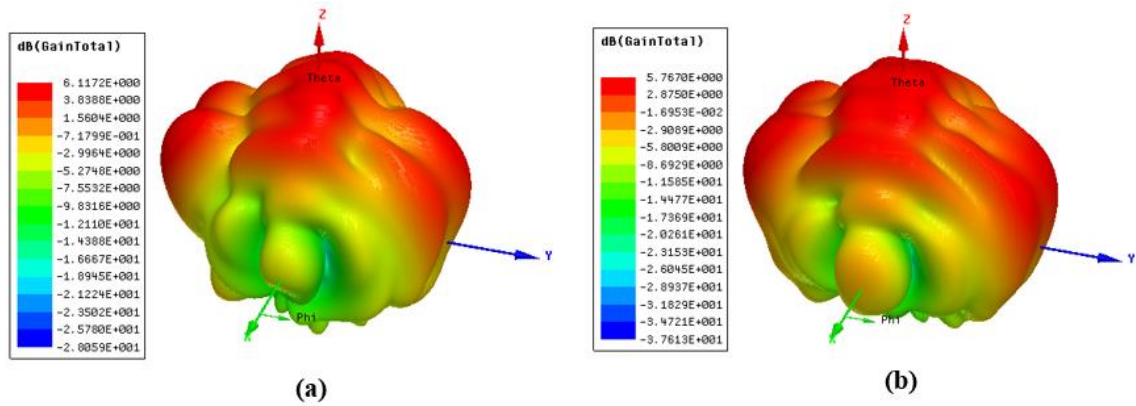


**Figure 6.4. Radiation patterns for the antenna on polyester fabric: (a) free space; and (b) on body.**

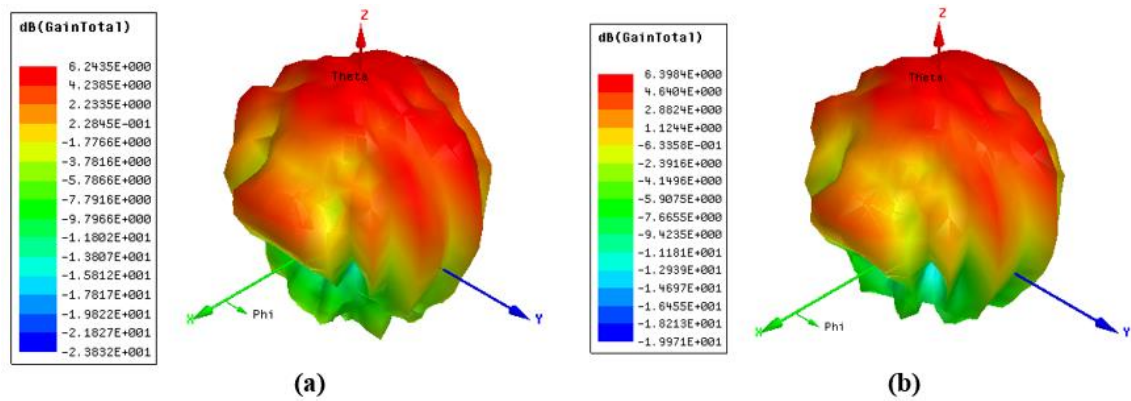


**Figure 6.5. Radiation patterns for the antenna on cotton fabric: (a) free space; and (b) on body.**

### 6.3. Material Characterisation

In order to better understand the sensing antenna's performance under different temperature and RH levels, it is essential to characterise the dielectric behaviours of substrate materials when they are exposed to a changing environment. Therefore, in this section, the measured

values of both polyester and cotton fabrics will be presented, along with the simulated  $S_{11}$  response of the antennae to the variation of environmental parameters.

### 6.3.1. Test setup

The hybrid-ML method proposed in Chapter 4 is employed to measure the  $\epsilon_r$  of substrate materials in the climate test chamber (Weiss WKL34). Considering that polyester has a larger  $\epsilon_r$  and thus a higher thermal coefficient of  $\epsilon_r$  as compared to the cotton substrate [124], the polyester fabric material is characterised under different temperature levels while keeping the humidity unchanged. It is expected that the  $\epsilon_r$  of a solid material, including fabrics, will increase with the temperature [125].

On the other hand, the cotton fabric is measured under different humidity levels while maintaining the temperature. This is because cotton has a strong ability of absorbing ambient moisture with  $\epsilon_r = 21$  and  $\tan\delta = 1.45$  at 38 GHz at 25 °C, which will then result in an increased  $\epsilon_r$  of the antenna's substrate, thereby shifting its resonant frequency. It can be assumed that the high-loss factor of water would lead to a distorted magnitude of  $S_{11}$ .

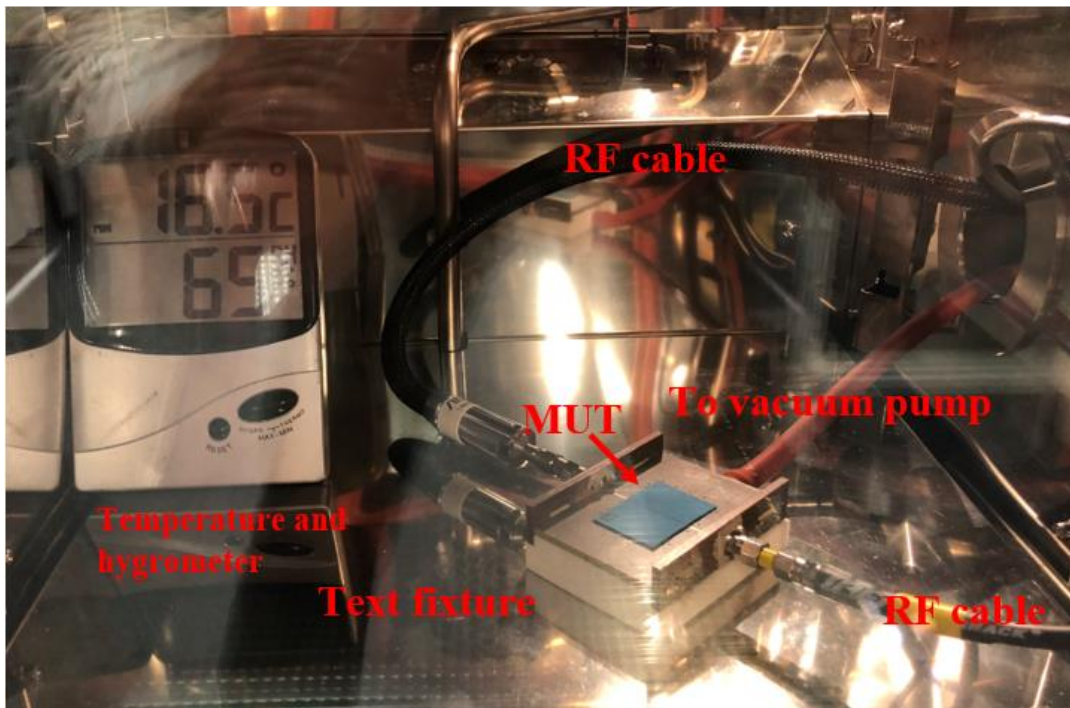


**Figure 6.6. Test setup inside the climate test chamber.**

The test setup inside the climate test chamber is shown as Figure 6.6. Fabric samples and the test fixture are firstly exposed to the preconfigured environmental conditions for a certain period of time after the inner space of chamber reaches a stable condition. A digital

temperature and hygrometer is used during the experiment to monitor the inner temperature and humidity levels. Two RF cables and air suction tubing of the fixture are inserted into the chamber via a through hole on its side wall, and connected to the Site Master S820E and an external vacuum pump, respectively. The MUTs are tested for 5 times for each condition, and the average results are taken.

During the test, a standard Rogers RT/d5880 (thickness 0.254 mm), which is the same dielectric material of the test fixture, is measured before testing MUTs at each condition. Therefore, the variation due to the standard dielectric of the fixture itself can be largely removed when processing the obtained values.

### 6.3.2. Temperature behaviour

A wearable temperature sensing antenna is designed for monitoring temperature variation on the skin surface, which ranges between a normal temperature of 36.8 °C and a feverish temperature of 39 °C. Therefore, the inner temperature of the chamber is increased from 35 °C to 40 °C in steps of 1 °C, while maintaining the inner RH at around 50%±10% to emulate a normal indoor humidity level. The MUT were also tested at 80 and 120 °C to observe the variation of  $\epsilon_r$  under a much wider temperature range. For each temperature level, a 15-min wait time was observed before taking the measurements. From the product specification of the chamber, the heating rate of its inner space is 4 °C per minute, and thus the 15-min interval is sufficient for the inner space to settle down and reach a stable condition. The measured values for the polyester fabric are listed in Table 6.4.

**Table 6.4. The variation of  $\epsilon_r$  of polyester substrate with temperature.**

Temperature (°C)	35	36	37	38	39	40	80	120
$\epsilon_r$	2.32	2.32	2.31	2.33	2.32	2.34	2.36	2.41

As what can be concluded from Table 6.4, within the temperature range of interest from 35 to 40 °C, the characterised  $\epsilon_r$  does not increase monotonically as expected. Instead, it fluctuates at about 2.33.

This result may be due to the measuring resolution of the fixture. According to [125], the  $\epsilon_r$  of a Terylene film increases by only 0.04 over a temperature range of 20 °C, corresponding to a change of 0.002 in the  $\epsilon_r$  for 1 °C. This variation is too tiny to be measured by the test fixture, and thus failing to characterise the materials.

This problem may be also caused by the small thermal coefficient of  $\epsilon_r$ . It is expected that a material with high  $\epsilon_r$  has a large thermal coefficient, but the  $\epsilon_r$  of polyester fabric (2.32) is not adequately high.

However, it is still demonstrated that the  $\epsilon_r$  of the substrate has a significant change from 2.32 to 2.41 over a much wider temperature change from 35 to 120 °C, proving the theory that the  $\epsilon_r$  of solid materials increases with temperature.

Therefore, it is concluded that the polyester fabric is not a suitable material for the body temperature sensing antenna. However, it may be used for other applications such as alarming the firefighters for a significant environmental temperature change.

### 6.3.3. Humidity behaviour

A humidity sensing antenna can be used for various applications such as breath humidity and skin hydration monitoring. Therefore, it is likely to operate inside the room where both temperature and humidity levels are well controlled.

Relative humidity (RH) describes the ratio of the partial pressure of water vapour ( $p_w$ ) to the equilibrium vapour pressure of water ( $p_{w,max}$ ) at a given temperature of an air-water mixture:

$$RH = \frac{p_w}{p_{w,max}} \times 100\%. \quad (6.1)$$

Compared to absolute humidity (AH), RH gives the percentage of water contained within a given space. Therefore, RH is more widely used than AH for describing the *humidity level*, which is the same in this work.

The parameter used to describe the ability of absorbing moisture of a material is moisture regain (MR), which is defined as [126]:

$$MR(\%) = \frac{\text{conditioned weight} - \text{dry weight}}{\text{dry weight}} \times 100\% \quad (6.2)$$

where the conditioned weight in this thesis is the weight of the material after it has been placed in a preconfigured humidity level in the chamber, and the dry weight is that achieved by exposing the materials in an oven at 105 °C for 5 hours [126]. Both the conditioned and dry weight were measured by a precision balance KERN 400-35A, whose weight ability is 600 g with a resolution of 0.01g. In order to minimise the variation of environmental condition while performing the measurements, the balance was placed beside the chamber, and the fabrics and antenna samples were weighed immediately after taken out of the chamber.

Prior to testing the humidity behaviour of the MUTs, they were proceeded to reach a dry status. Thereafter, the MUTs are placed inside the chamber, where the RH level is increased from 30% to 90% in steps of 10% while maintaining the ambient temperature at 35 °C (body skin temperature). Because the vacuum pump is actually sucking out the inner wet air, it takes more time for the RH and the MUTs inside the chamber to stabilise. Therefore, the waiting time is set to 20 minutes for this experiment. It should also be clarified here that from the technical specification, the 30% is the minimal RH level that can be reached by the climate test chamber if its inner temperature is set to 35 °C.

The measured phase of the transmission coefficient of cotton fabric under different RH levels are plotted in Figure 6.7, and the characterised  $\epsilon_r$  values and the MR of the cotton fabric are listed in Table 6.5.

**Table 6.5. The variation of  $\epsilon_r$  of cotton fabric to RH levels.**

RH (%)	30	40	60	80	90
$\epsilon_r$	1.83	1.85	1.91	1.98	2.02
MR (%)	2.30	4.60	6.89	9.19	10.35

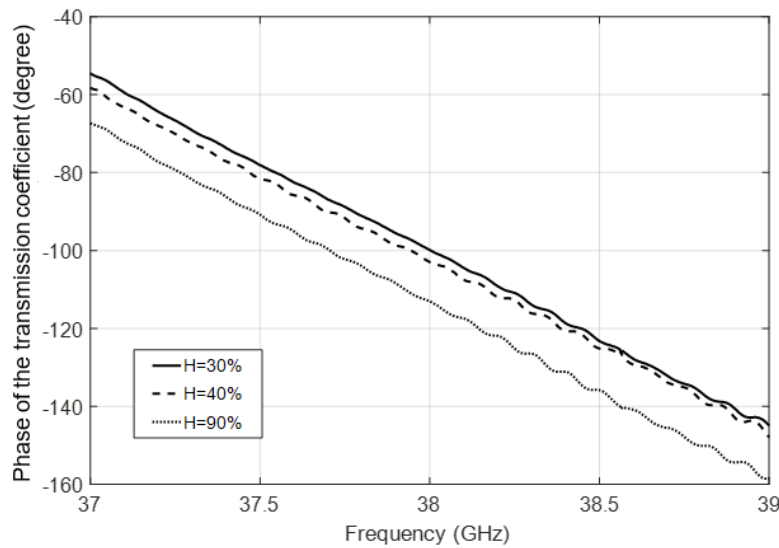


**Figure 6.7. Measured phase of transmission coefficient under different RH levels.**

It shows that the characterised  $\epsilon_r$  has a relatively linear relationship with the RH, increasing by about 0.02–0.04 when the RH increases for 10%.

Notably, the  $\epsilon_r$  characterised at 60% (1.91) is close to the one presented in Chapter 4 at around 50% (1.90). The small variation may be due to the ambient environmental effects

as the measurements in Chapter 4 were not taken in a well-controlled and sealed space as those taken in this work.

Based on the characterised values, the variation of  $S_{11}$  with the RH levels were further analysed. This is done by changing the  $\epsilon_r$  of the substrate material in HFSS according to Table 6.5, and simulating the  $S_{11}$  representing for different RH levels. The results are plotted in Figure 6.8, which clearly shows that the resonant frequency of the sensing antenna decreases with an increasing RH level.

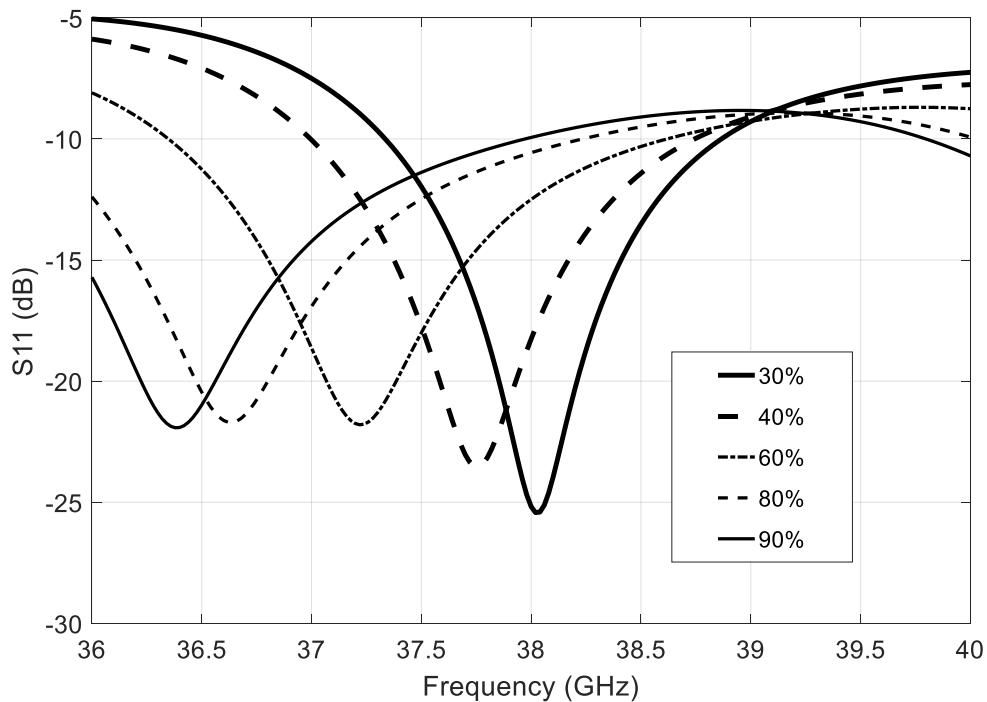


**Figure 6.8. Simulated  $S_{11}$  response with the variation of RH levels.**

## 6.4. Performance of the Humidity Sensing Antenna

As discussed in Section 6.3, it is more promising to realise a humidity sensing rather than temperature sensing antenna for BAN applications. Therefore, a fabricated humidity sensing antenna will be presented, and its measured  $S_{11}$  response under different RH levels.

### 6.4.1. Fabricated antenna prototype

The antenna was laser-cut from thin copper foil with adhesive backing on fabric substrate. One fabricated prototype is shown in Figure 6.9, whose outer dimensions are approximately 30 mm  $\times$  20 mm. To maintain the flexibility of the antenna, its ground

plane still uses a plain-woven conductive fabric tape, which is made of nylon plated with nickel and copper. Similar to previous chapters, an end-launch connector is attached at the end of feed line for interfacing the antenna with a measurement system.



**Figure 6.9. Fabricated prototype of the humidity sensing antenna.**

The measurement setup for obtaining the antenna's  $S_{11}$  is shown in Figure 6.10. A RF coaxial cable is inserted from VNA into the climatic test chamber via its through hole for in-situ measurement.

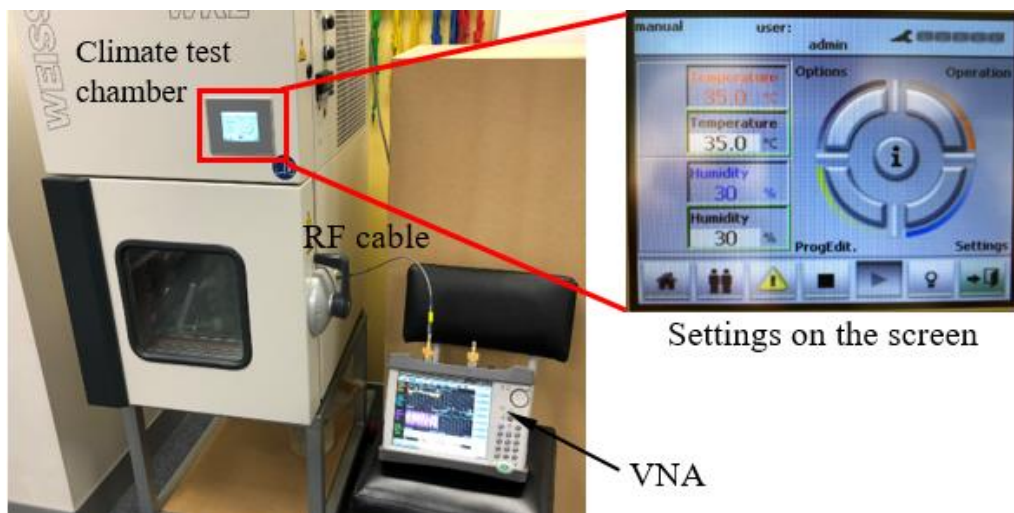


**Figure 6.10. Measurement setup of measuring  $S_{11}$ .**

Figure 6.11 compares the measured and simulated  $S_{11}$ , which shows good agreement in terms of their magnitude and resonant frequency at 35 °C and 30% RH. The slight differences may be due to effects of the thin adhesive layer of copper foil and unknown RF characteristics (e.g.  $S$ -parameters) of the end-launch connector not considered in the simulation.

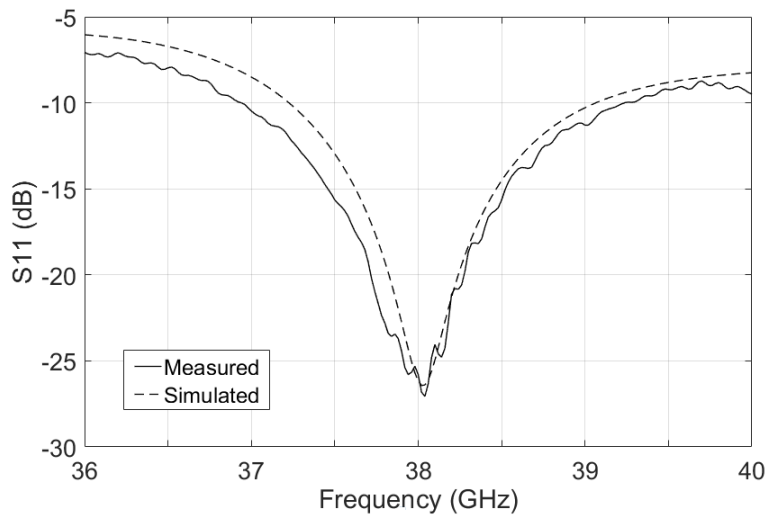


**Figure 6.11. Measured and simulated  $S_{11}$  for the sensing antenna.**

#### **6.4.2. Antenna response to ambient humidity**

The antenna's response to ambient RH level is then further evaluated. The test setup is that as shown as Figure 6.10. For consistency with previous measurements, the RH level inside the chamber is increased from 30% to 90% in steps of 10% while maintaining the chamber at 35 °C. Since no vacuum pump is used here, for each step, the waiting time is reverted to 15 minutes for antenna condition to settle before measurement. As before, the antenna was placed in an oven to reach its dry status, and its measured dry weight is 0.47 g (including copper ground and radiating patch). To compare, the antenna's weight at each RH level was listed in Table 6.6. As can be seen, however, the weight increased only very slightly between each humidity levels, which might be due to the inadequate resolution of the scale. From previous literature, the MR for cotton fibres is ~7.5% at 65% RH [126]. It means that a pure 0.47-g cotton fabric can only increase by a maximal of 0.035 g, which results in a 0.005-g weight variation for 10% RH change, and this is beyond the resolution of the scale (0.01 g).

Figure 6.12 shows the measured  $S_{11}$  response (averaged over five measurements) under different RH levels. As can be seen from Figure 6.12, it has the same trend as the simulated result, i.e. the antenna's resonant frequency ( $f_0$ ) decreases with increasing RH level. Further, the  $f_0$  exhibits a relatively linear relationship with humidity (see Figure 6.13), from which a high sensing resolution of 26 MHz per 1% RH is achieved.

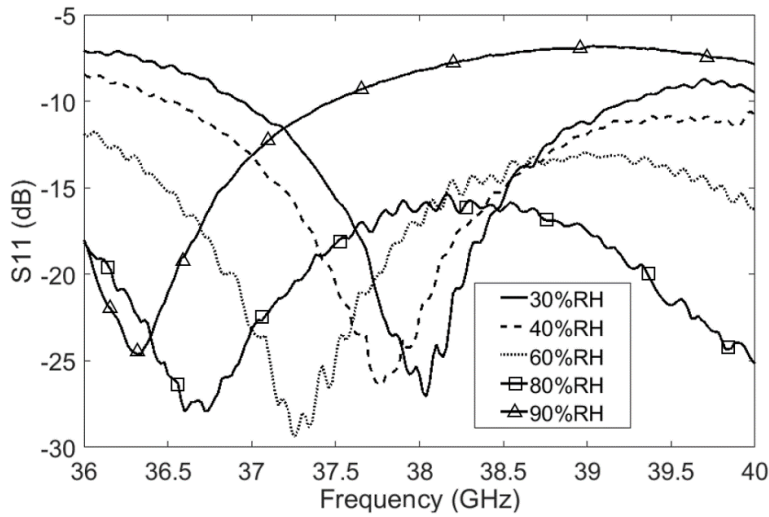


**Figure 6.12. Measured  $S_{11}$  response of antenna to ambient RH level.**

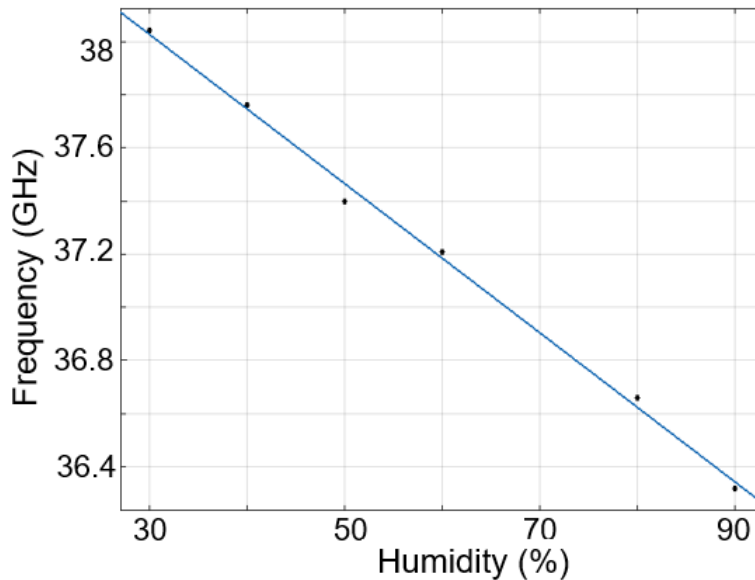


**Figure 6.13. Humidity-resonant frequency relationship.**

The linear RH- $f_0$  relationship shown in Figure 6.13 can be simply expressed as:

$$\text{RH (\%)} = af + b \quad (6.2)$$

where  $a = -35.23$  and  $b = 1371$  are the best-fit coefficients found in MATLAB, and  $f$  is the measured resonant frequency of the antenna.

One should note there exist differences between the simulated and measured magnitude of  $S_{11}$  for each RH levels in Figure 6.7 and Figure 6.11, respectively. This is because the inner space of the climate test chamber is unlike a RF anechoic chamber, where the antenna is shielded from reflections and external interferences by the absorbers, and Faraday cage, respectively. Therefore, the measured results in the climatic test chamber are less accurate, and particularly affected by wave reflections. Besides, the loss factor of

water is large at 38 GHz, which also distorted the  $S_{11}$  curve. However, there is still a good agreement in the resonant frequency between the measured and simulated results as listed in Table 6.6.

**Table 6.6. Measured and simulated resonant frequency of the antenna response to the ambient RH levels, and the measured weight under each humidity level.**

RH level	30%	40%	60%	80%	90%
Simulated $f_0$ (GHz)	38.05	37.76	37.22	36.65	36.3
Measured $f_0$ (GHz)	38.04	37.78	37.26	36.68	36.32
Measured weight (g)	0.48	0.48	0.50	0.51	0.52

Finally, the realised gain of the humidity sensing antenna is examined in the anechoic chamber, following the setup in Figure 2.19 and Figure 5.13, and the method for the realised gain measurement presented in Chapter 2. The measurement was done by transferring the antenna to the anechoic chamber once it has been exposed to 30% RH for 15 minutes in the climate test chamber. The realised antenna gain measured in free space is  $\sim 5.5$  dBi, which can be further enhanced by other methods such as the EBG presented in Chapter 5.

It should be noted that during measurement, the RH level is the only changing parameter inside the chamber while all other conditions (e.g. temperature) remain unchanged. Thus, it can be concluded that the variation of the  $\epsilon_r$  of the cotton fabric and the  $f_0$  of the antenna is due to the moisture contents in the cotton substrate.

In this thesis, a portable network analyser Anritsu S820E was used to measure the frequency shift of the antenna prototypes. This shift can also be evaluated with spectrum analysers by observing the variation of the frequency where peak power is received on the analyser side. A wideband antenna can be used to receive the sensing data. However, both instruments are bulky and expensive, and thus not convenient for daily usage and civilian applications. Fortunately, with advances in mm-wave identification (MMID) technology and accelerating progress of commercialising MMID chips [127], optimised sensing antennae with higher sensitivity can be designed to work with MMID tag chips. Therefore, this frequency shift can be measured by detecting the variation of power reflection coefficient of the chip by MMID readers, whose tentative operating bandwidth is 5 GHz [128].

## 6.5. Summary

In this chapter, the design of a wearable sensing antenna operating at 38 GHz was presented. The antenna is intended for monitoring the temperature of the skin surface and the humidity level in the near space of the human body.

The antenna was designed to be a low-profile microstrip patch structure and utilise regular fabrics as the substrate, which enables an easy integration of the antenna into everyday garments for healthcare monitoring applications.

Two types of substrates, a polyester fabric and a cotton fabric, were selected for this design. In this chapter, the geometrical dimensions of the antenna were first determined in HFSS for each type of the substrate. Next, the simulated  $S_{11}$  and radiation patterns were presented for both antennae when operating in free space or in proximity to human bodies. The results show slight differences between these two operating conditions, mainly due to the ground plane on the opposite side of the substrate which minimises the human body effects. When positioned on a human body, the antenna still exhibits a relatively high- $Q$  factor that is sensitive to small variations of  $\epsilon_r$  of the substrate fabric.

Following that, the candidate substrate materials were measured using the hybrid-ML method in the climate test chamber. Concerning the material's temperature response, as the tiny change of the  $\epsilon_r$  over the small range of body temperature is beyond the measuring resolution of the test fixture, the characterisation work is unfortunately not successful. However, it is still demonstrated that  $\epsilon_r$  can significantly change over a large temperature range, which will be beneficial to other on-body applications.

On the other hand, the material's  $\epsilon_r$  has a relatively linear response to the ambient RH levels. The results show that the antenna's resonant frequency decreases with increasing RH levels.

Finally, a prototype of the humidity sensing antenna was laser-cut on cotton substrate. Differences can be observed in the magnitude of the  $S_{11}$  between the simulated and measured results, which may be due to the less-than-ideal RF test environment of the inner space of the climate test chamber, and the large loss factor of water at 38 GHz. However, there exists a good agreement between the measured and simulated antenna responses in terms of its resonant frequency in free space. The antenna is found to have a high sensing resolution of 26 MHz per 1% RH.

# Chapter 7

## Conclusion and Future Work

### 7.1. Conclusion

This thesis focuses on the design of flexible RF structures operating at mm-waves for wearable applications, with a focus on the areas of characterising dielectric materials, enhancing the performance of wearable antennae and designing sensing antennae for BANs. In the first three chapters, an introduction to the research, background concepts, and critical analysis of related literature are presented. In Chapter 4, a novel hybrid-TL method was proposed to characterise the properties of several dielectric materials for BANs at mm-waves. The accuracy of the proposed method and the designed test fixture was investigated. Chapter 5 presented a flexible EBG whose unit cell has a fractal design with self-similar window-like patterns that can be easily fabricated with existing laser-cutting technique. The fabricated EBG was then integrated as a high-impedance surface (HIS) with a wearable CPW antenna. The performance of the EBG-backed CPW antenna, such as the magnitude of  $S_{11}$ , radiation patterns and realised gain, was evaluated and compared with those obtained for a stand-alone CPW antenna. Finally, in Chapter 6, the design of wearable sensing antennae for monitoring skin surface temperature or humidity level was investigated. Two candidate substrate materials were measured at different temperature or humidity levels in the climate test chamber. Thereafter, a prototype of the humidity sensing antenna and its measured response to ambient humidity in free space were presented.

The following summarises the main contributions of this thesis, discusses the limitations encountered, and suggests promising research directions for future work.

### 7.2. Contributions

The contributions of this thesis can be summarised as follow:

- A hybrid-TL method was firstly proposed to characterise dielectric materials at mm-waves. Since it is not common for substrate manufacturers to provide their products' electrical specifications at mm-waves, particularly for new materials that have been introduced for wearable RF applications, the proposed method offers an accurate and fast way to characterise the materials' complex permittivity, which helps to avoid the frequency shift due to dielectric variation of the substrate materials. Besides, by introducing two error boxes at the end of transmission line, the impacts of impedance mismatch and signal path discontinuities caused by the signal path transitions from one type of TL to another can be largely removed.
- A universal test fixture was designed and fabricated based on the proposed hybrid-TL method. Rows of air suction holes were designed on top of the fixture for holding down light and flexible substrate materials during measurement. Several types of dielectric materials, including conventional RF PCB laminates and flexible fabrics, were measured with the fixture. The results showed that the characterised dielectric properties of the materials are close to those specified by vendors, and characterised with other existing techniques. Due to the introduction of the error boxes, less error can be observed for the proposed hybrid-TL method as compared to those obtained by existing L-L method.
- An EBG design was proposed for wearable antennae at mm-waves. Fractal design was applied to each individual unit cell of this EBG, which was realised by repeatedly constructing square strips within a larger square with multiple iterations. The bandgap of this EBG was evaluated by examining the transmission coefficient of a microstrip line that is suspended over the EBG. The simulated results show that three iterations can cover the frequency range of interest from 20 to 40 GHz. A prototype of the EBG with  $3 \times 3$  unit cells was fabricated on polyester fabric substrate, and then integrated with a wearable CPW antenna. The measurement results show that compared to stand-alone CPW antenna, the EBG-backed CPW antenna can achieve a wider  $-10$ -dB bandwidth, reduced backward radiation patterns and an enhanced antenna gain directing away from the human body. The on-body performance of the EBG-backed CPW antenna was also evaluated, which demonstrated only slight differences from that in free space scenario.
- Sensing antennae were investigated for monitoring the temperature of skin surfaces and humidity level of the user's surrounding. The antennae detect signals based on the fact that their substrate's permittivity can be changed by

environmental factors. The antenna was designed based on a microstrip patch, which inherently behaves a narrow bandwidth and high quality factor ( $Q$  factor) to improve the sensitivity of the sensing antennae. The characterised values of candidate substrate materials showed that the response of dielectric constant to temperature is weak and beyond the measuring resolution of the test fixture. However, there is a significant dielectric response of the material to the ambient humidity, and thus a humidity sensing antenna was fabricated. There is a good agreement between the measured and simulated results. It shows that the sensing antenna has a relatively linear relationship with ambient humidity, and a high sensing resolution of 26 MHz per 1% RH can be achieved with the proposed design.

### **7.3. Limitations and Future work**

There still exist some limitations for this work, and thus a number of research directions for future work can be pursued in this area:

- A trade-off was made when choosing conductive materials between the flexibility and fabrication accuracy at mm-waves. Therefore, flexible copper foil, which is still classified as conventional solid metal, was used to construct the antenna patches and feed lines in this thesis. This introduced a few problems. For example, the unknown property of the glue under the adhesive copper foil, which is difficult to separate for characterisation, may introduce uncertainties and altered the performance of the fabricated structures. Since conductive inks are the most ideal materials for wearable applications, it is worth investigating the fabrication of fully fabric mm-wave RF structures by using high-resolution printing techniques. Further, the characterisation of conductive inks at mm-waves can be another interesting topic to study;
- For the proposed hybrid-TL method, even though two error boxes are introduced at the ends of the TL, the result accuracy and measureable range of dielectric constant are still affected by the quality of impedance matching at the transition sections. Besides, other factors such as radiation loss, air suction strength and air gap size, are also introducing errors into the measured results. To fully understand the proposed hybrid-TL method, further evaluation of its accuracy by considering the aforementioned factors is recommended. Furthermore, an algorithm such as

the pencil matrix or Taylor Expansion can be implemented to process the measured results in order to minimise the system noise introduced by the test fixture;

- The EBG-backed CPW antenna has been well studied in this work. However, its radiation pattern was evaluated when it was worn by a person standing inside the anechoic chamber. This configuration introduced difficulties and potential errors in the measurement process. Therefore, the use of a body phantom for mm-wave is preferred for such measurements. Besides, it will be interesting to analyse its performance when it is crumpled and after washing. Furthermore, the performance of the EBG for other types of wearable antennae and RF components such as filters and duplexers could be investigated;
- The design of the temperature sensing antenna was unfortunately not successful, mainly due to the properties of the substrate materials. This could be improved in two aspects: the first is the aforementioned accuracy improvement for the characterisation method and the current test fixture; the second is to develop more suitable textile substrates, which can be realised by depositing high-dielectric particles into the textile fibres to increase the dielectric constant of the fabricated product, thereby increasing its thermal coefficient of dielectric constant;
- Restricted by the facilities, the extent of on-body performance evaluation of the humidity sensing antenna is limited. This is because it requires a sufficiently large climatic test chamber equipped with suitable facilities for RF measurements.

To summarise, this thesis has further studied the application of flexible dielectrics and soft conductors to construct wearable RF structures operating at mm-wave frequency bands. The research contributes to characterising textile dielectric materials, improving the performance of wearable antennae, and designing wearable antennae as sensing elements in BANs for 5G networks. The investigation and experiments presented indicate that there are huge possibilities to use flexible wearable antennae to replace conventional rigid ones for on-body applications, and will help in the future realisation of a complete fabric body-worn antenna system in our daily living.

# Appendix A

## Design of Test Fixture

In Chapter 4, a test fixture is designed based on the proposed hybrid-transmission-line method to characterise the complex permittivity of dielectric materials. This appendix presents its bill of materials (BOM) and mechanical drawings from CAD software.

### A.1. Bill of Materials

The materials required for constructing the fixture is listed as Table A.1.

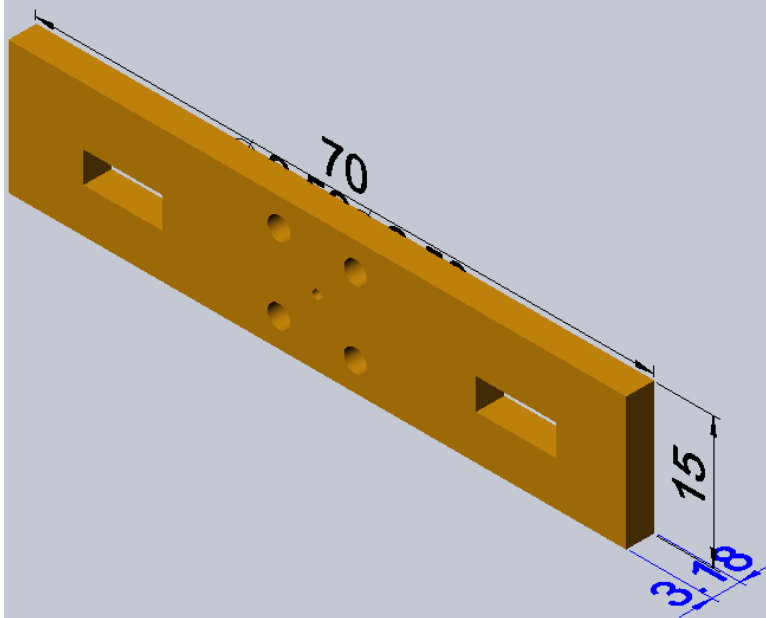
**Table A.1. Bill of materials.**

No.	Item	Specification	Qty.
1	Rogers RT/d5880	Dielectric thickness 0.254 mm, one side copper 12.5 $\mu\text{m}$ , the other side copper 2 mm	1
2	2.92-mm connector	Female connector 4 hole, 0.500" square flange - accepts 0.012 pin diameter Southwest Corp.: 1012-01SF	2
3	Transition pin/dielectric	Southwest Corp.: 1090-06G	2
4	Test fixture ear	Copper made fixture ears with drilled holes to hold connectors	2
5	Fixture base	3D printed plastic fixture base with air chamber	1
6	Silver epoxy	MG Chemicals, MG8330S-21G	As required

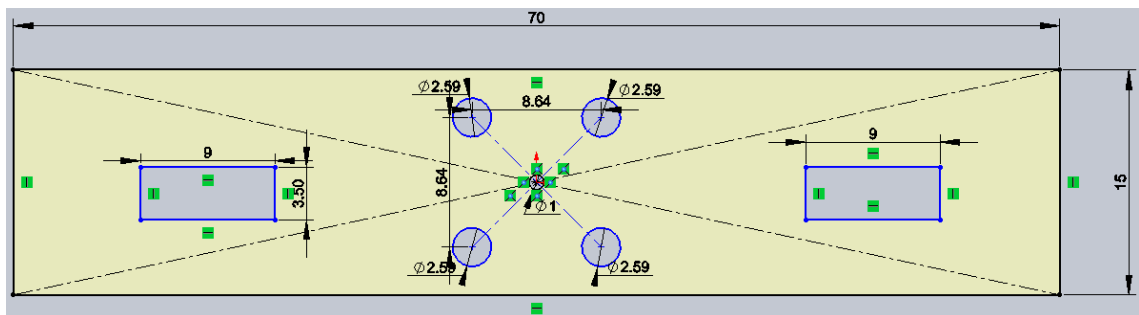
## A.2. Mechanical Drawings

### A.2.1. Test fixture ear

The mechanical drawings of the test fixture ear is illustrated in Figure A.1.



(a)

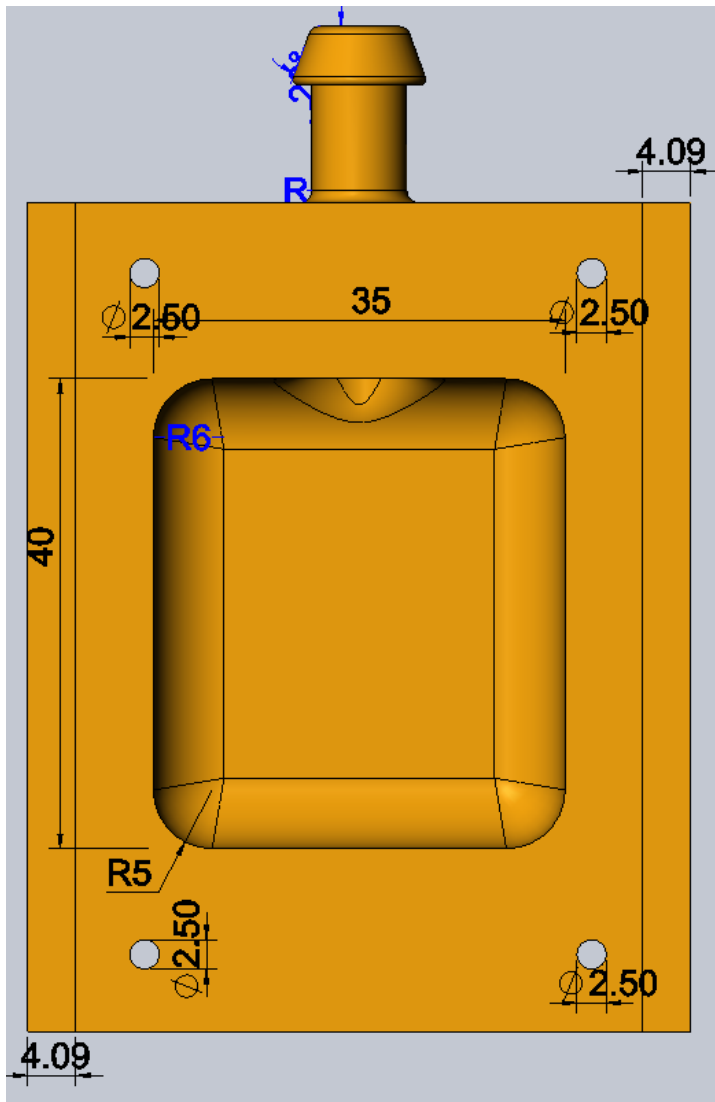


(b)

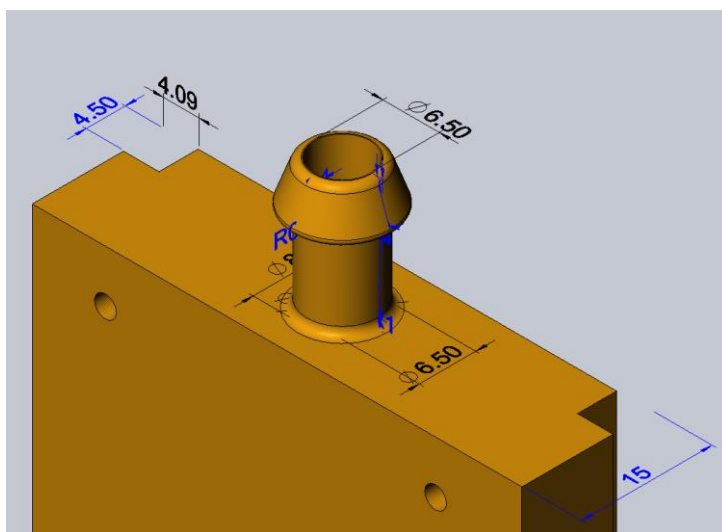
Figure A.1. Test fixture ear: (a) 3D view; (b) 2D view.

### A.2.2. Fixture base

The mechanical drawing of the fixture base is illustrated in Figure A.2. The design is saved as .DXF format and then 3D printed with plastic powders.



(a)



(b)

Figure A.2. Test fixture base: (a) top view; (b) zoom-in of the top part of the base.

### A.2.3. Dielectric board

The design of the dielectric board and the microstrip line is illustrated in Figure A.3.

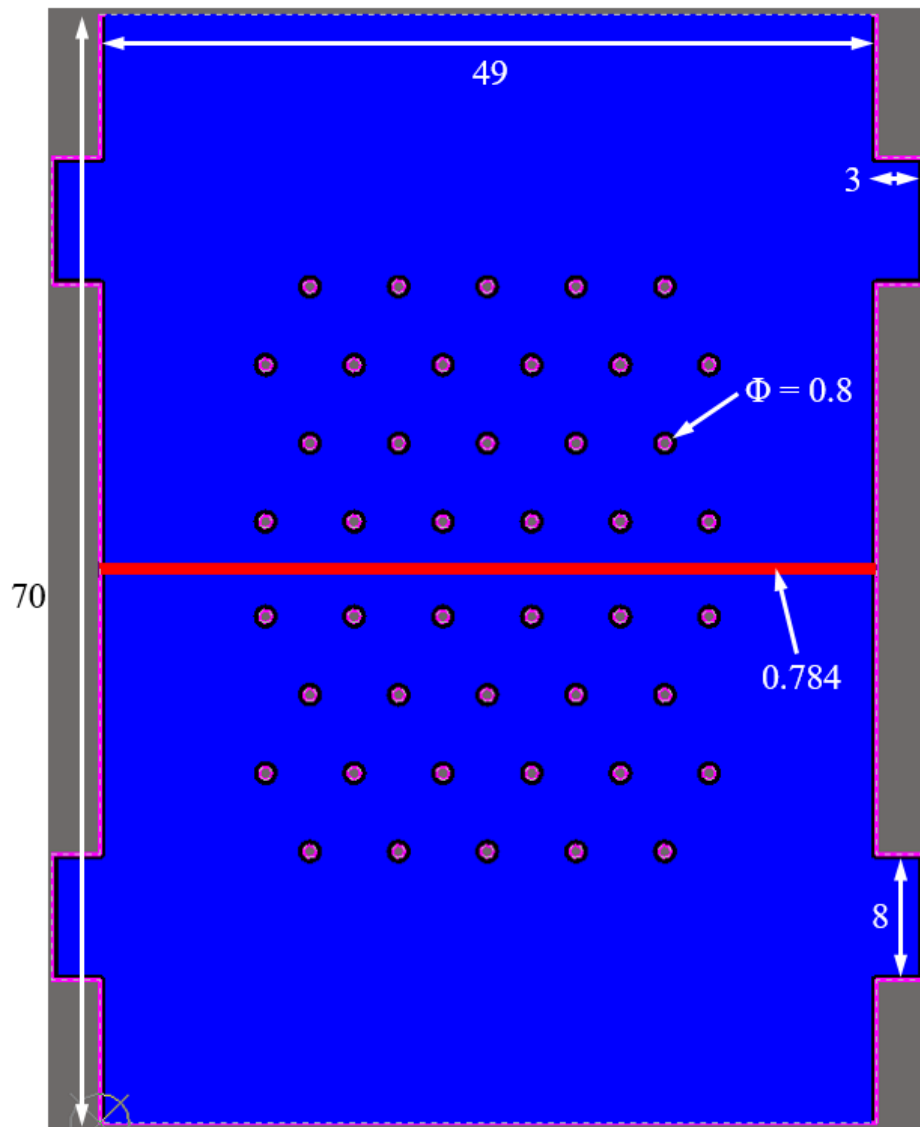


Figure A.3. Dielectric board and microstrip line (unit: mm).

# Appendix B

## MATLAB Code for Characterising Dielectric Materials

The code provided below is for charactering dielectric materials based on the proposed hybrid-transmission-line method and the variation of measured  $[S]$  of the fixture designed in Chapter 4.

```
clear
clc

L=0.028; %covered length, unit in metre
mu0=4*pi*10^(-7); %permeability in the vacuum
c0=2.99792458*10^(8); %speed of light in the air
e0=1/(c0*c0*mu0); %permittivity in the vacuum

%read T1 and T2, and get frequency range info
t1=tparameters('init 2.s2p'); % [T] of the uncovered fixture
%read measured T2 and averaging
t21=tparameters('9 2.s2p');
t22=tparameters('12.s2p');
t23=tparameters('13.s2p');
t24=tparameters('14.s2p');
t25=tparameters('15.s2p');

freq=t1.Frequencies; %freq range 37-39 GHz

%read measured only T-parameters
T1=t1.Parameters; %uncovered fxiture [T] only
T2=t21.Parameters; %covered fixture [T] only
T22=t22.Parameters;
T23=t23.Parameters;
T24=t24.Parameters;
T25=t25.Parameters;

%averageing the multiple-time measurements
for k=drange(1:501)
    T2(:, :, k)=T21(:, :, k);
end

%calculate the product of [T1*T2-1]
for k=drange(1:501)
    invT2(:, :, k)=inv(T2(:, :, k)); %inverse matrix of T2;
end

for k=drange(1:501)
    M1(:, :, k)=T1(:, :, k)*invT2(:, :, k); %the product of [T1*T2-1]
```

```

end

%calculate the eigenvalues of [T1*T2-1]
for k=drange(1:501)
    eigenvalue(k, :, :) = eig(M1(:, :, k)); %eigenvalues of fixture results
end

eigenvalue1 = eigenvalue(:, 1); %get one eigenvalue
x1 = log(eigenvalue1);
x2 = (x1 + 2*pi*0*j) ./ L; %"+" or "-"

%calculate gamma1 (bared line)

t1 = tparameters('unc28_501.s2p'); %T parameters of the bared
line
T1 = t1.Parameters;

for k=drange(1:501)
    T111(k, :, :) = T1(1, 1, k); %This is T111
end

gamma11 = log(T111) + 2*pi*5*j;

gamma1 = gamma11 ./ L; %prop c of the bared line
gamma2 = gamma1 - x2;

beta = imag(gamma2);
figure(1)
subplot(3, 1, 1)
plot(freq, beta)
title('Beta')

%calculate k0
k0 = 2.*pi.*freq./c0;
subplot(3, 1, 2)
plot(freq, k0)
title('Wave Number in the Air')

eff = (beta./k0).^2;

```

# References

- [1] M. Stoppa, and A. Chiolerio, “Wearable electronics and smart textiles: a critical review,” *Sensors*, vol. 14, no. 7, pp. 11957-11992, 2014.
- [2] L. M. Castano and A. B. Flatau, “Smart fabric sensors and e-textile technologies: a review,” *Smart Materials and Structures*, vol. 23, no. 5, pp. 1–27, 2014.
- [3] N. V. Desai, “A low power, reconfigurable fabric body area network for healthcare applications,” Ph.D. dissertation, Dept. of Elect. Eng. Comput. Sci., Massachusetts Institute of Technology, Cambridge, MA, 2012.
- [4] M. Swan, “Sensor mania! The internet of things, wearable computing, objective metrics, and the quantified self 2.0,” *J. Sensor Actuator Networks*, vol. 1, no. 3, pp. 217–253, 2012.
- [5] P. Rashidi, A. Mihailidis, “A survey on ambient-assisted living tools for older adults,” *IEEE J. Biomed. Health Inform.*, vol. 17, no. 3, pp. 579–590, 2013.
- [6] A. Bouazizi, G. Zaibi, M. Samet and A. Kachouri, “Wireless body area network for e-health applications: Overview,” *2017 International Conference on Smart, Monitored and Controlled Cities*, Sfax, 2017, pp. 64–68.
- [7] N. Chahat, M. Zhadobov, L. Le Coq, S. I. Alekseev, and R. Sauleau, “Characterization of the interactions between a 60-GHz antenna and the human body in an off-body scenario,” *IEEE Trans. Antennas Propag.*, vol. 60, no. 12, pp. 5958–5965, 2012.
- [8] H. Xiaomu, S. Yan and G. A. Vandebosch, “Wearable button antenna for dual-band WLAN applications with combined on and off-body radiation patterns,” *IEEE Trans. Antennas Propag.*, vol. 65, no. 3, pp. 1384–1387, 2017.
- [9] M. M. Khan, Q. H. Abbasi and R. H. Ashique, “Comprehensive design and propagation study of a compact dual band antenna for healthcare applications,” *J. Sensor Actuator Netw.*, no. 4, pp. 50–66, 2015.
- [10] R. Cavallari, F. Martelli, R. Rosini, C. Buratti and R. Verdone, “A survey on wireless body area networks: technologies and design challenges,” *IEEE Commun. Surv. Tuts.*, vol. 16, no. 3, pp. 1635–1657, 2014.
- [11] I. Locher, M. Klemm, T. Kirstein and G. Troster, “Design and characterization of purely textile patch antennas,” *IEEE Trans. Adv. Packag.*, vol. 29, no. 4, pp. 777–788, 2006.
- [12] Z. Wang, L. Zhang, Y. Bayram and J. L. Volakis, “Multilayer printing of embroidered RF circuits on polymer composites,” in *IEEE Int. Symp. Antennas Propag.*, July 2011, pp. 278–281.
- [13] W. G. Whittow, Y. Li, R. Torah, K. Yang, S. Beeby and J. Tudor, “Printed frequency selective surfaces on textiles,” *Electronics Lett.*, vol. 50, no. 13, pp. 916–917, 2014.
- [14] M. E. B. Jalil, M. K. Abd Rahim, N. J. Ramly, N. A. Samsuri, K. Kamardin, M. Azfar Abdullah and H. A. Majid, “Planar Textile Antenna for Body Centric Wireless Communication System,” *Progress Electromag. Res. C*, vol. 54, pp. 29–40, 2014.
- [15] D. Cottet, J. Grzyb, T. Kirstein and G. Tröster, “Electrical characterization of textile transmission lines,” *IEEE Trans. Adv. Packag.*, vol. 26, no. 2, pp. 182–190, 2003.
- [16] Y. Ouyang and W. J. Chappell, “High frequency properties of electro-textiles for wearable antenna applications,” *IEEE Trans. Antennas Propag.*, vol. 56, no. 2, pp. 381–389, 2008.

- [17] R. K. Shawl, B. R. Longj, D. H. Werner and A. Gavrin, "The characterization of conductive textile materials intended for radio frequency applications," *IEEE Antennas Propag. Mag.*, vol. 49, no. 3, pp. 28–40, 2007.
- [18] S. Sankaralingam and B. Gupta, "Determination of dielectric constant of fabric materials and their use as substrates for design and development of antennas for wearable applications," *IEEE Trans. Instrum. Meas.*, vol. 59, no. 12, pp. 3122–3130, 2010.
- [19] F. Declercq, H. Rogier and C. Hertleer, "Permittivity and loss tangent characterization for garment antennas based on a new matrix-pencil two-line method," *IEEE Trans. Antennas Propag.*, vol. 56, no. 8, pp. 2548–2554, 2007.
- [20] R. Salvado, C. Loss, R. Gonçalves and P. Pinho, "Textile materials for the design of wearable antennas: a survey," *Sensors*, vol. 12, no. 11, pp. 15841–15857. 2012.
- [21] N. Chahat, M. Zhadobov, S. A. Muhammad, L. Le Coq and R. Sauleau, "60-GHz textile antenna array for body-centric communications," *IEEE Trans Antennas Propag.*, vol. 61, no. 4, pp. 1816–1824, 2013.
- [22] N. Chahat, M. Zhadobov, L. Le Coq and R. Sauleau, "Wearable endfire textile antenna for on-body communications at 60 GHz," *IEEE Antennas Wireless Propag. Lett.*, vol. 11, pp. 799–802, 2012.
- [23] X. Liu, Y. Di, H. Liu, Z. Wu and M. M. Tentzeris, "A planar windmill-like broadband antenna equipped with artificial magnetic conductor for off-body communications," *IEEE Antennas Wireless Propag. Lett.*, vol. 15, pp. 64–67, 2016.
- [24] M. Ur-Rehman, N. A. Malik, X. Yang, Q. H. Abbasi, Z. Zhang and N. Zhao, "A low profile antenna for millimetre-wave body-centric applications," *IEEE Trans. Antennas Propag.*, vol. 65, no. 12, pp. 6329–6337, 2017.
- [25] Y. J. Cheng, W. Hong and K. Wu, "94 GHz substrate integrated monopulse antenna array," *IEEE Trans. Antennas Propag.*, vol. 1, no. 60, pp. 121–129, 2012.
- [26] Z. Wang, L. Z. Lee, D. Psychoudakis and J. L. Volakis, "Embroidered multiband body-worn antenna for GSM/PCS/WLAN communications," *IEEE Trans. Antennas Propag.*, vol. 62, no. 6, pp. 3321–3329. 2014.
- [27] B. K. Tehrani, B. S. Cook, and M. M. Tentzeris, "Inkjet printing of multilayer millimeter-wave Yagi-Uda antennas on flexible substrates," *IEEE Antennas Wireless Propag. Lett.*, vol. 15, pp. 143–146, 2016.
- [28] D. M. Pozar, *Microwave engineering*. 3rd ed. New York, U.S.A: John Wiley & Sons: 2009.
- [29] C. P. Wen, "Coplanar waveguide: A surface strip transmission line suitable for nonreciprocal gyromagnetic device applications," *IEEE Trans. Microw. Theory Techn.*, vol. 17, no. 12, pp. 1087–1090, 1969.
- [30] G. A. Deschamps, *Microstrip microwave antennas*, Presented at the 3rd USAF Symposium on Antennas, 1953.
- [31] A. B. Constantine, *Antenna theory: analysis and design*. 3rd ed. New York, U.S.A.: John wiley & sons: 2016.
- [32] J. D. Kraus, and R. J. Marhefka, *Antennas for all applications*. 3rd. ed. New York, U.S.A: McGraw-Hill: 2003.
- [33] D. F. Sievenpiper, Lijun Zhang, R. F. J. Broas, N. G. Alexopolous and E. Yablonovitch, "High-impedance electromagnetic surfaces with a forbidden frequency band," *IEEE Trans. Microw. Theory Techn.*, vol. 47, no. 11, pp. 2059–2074, 1999.
- [34] M. Abegaonkar, A. Orlandi, *Electromagnetic bandgap (EBG) structures: common mode filters for high speed digital systems*. 1st ed. Hoboken, N.J., U.S.A.: IEEE Press: Wiley: 2017.

- [35] D. F. Sievenpiper, "High-impedance Electromagnetic Surfaces", Ph.D. dissertation, Dept. Elect. Eng., UCLA, California, L.A., 1999.
- [36] A. Aminian, F. Yang, and F. Rahmat-Samii, "In-phase reflection and EM wave suppression characteristics of electromagnetic band gap ground planes," In *Antennas Propag. Soc. Int. Symp.*, vol. 4, pp. 430–433, Los Angeles, CA, 2003.
- [37] S. Schneegass, and O. Amft, Smart textiles. Cham, Switzerland: Springer: 2017.
- [38] M. Syduzzaman, S. U. Patwary, K. Farhana, and S. Ahmed, "Smart textiles and nano-technology: a general overview," *J. Text. Sci. Eng.*, vol. 5, 1000181, 2014.
- [39] S. Coyle *et al.*, "BIOTEX - biosensing textiles for personalised healthcare management," *IEEE Trans. Inform. Techn. Biomedicine*, vol. 14, no. 2, pp. 364–370, 2010.
- [40] T. Acti *et al.*, "Embroidered wire dipole antennas using novel copper yarns," *IEEE Antennas Wireless Propag. Lett.*, vol. 14, pp. 638–641, 2015.
- [41] S. Zhang, A. Paraskevopoulos, C. Luxey, J. Pinto and W. Whittow, "Broad-band embroidered spiral antenna for off-body communications," *IET Microw. Antennas Propag.*, vol. 10, no. 13, pp. 1395–1401, 2016.
- [42] J. A. Rogers, and Y. Huang, "A curvy, stretchy future for electronics," *Proc. Nat. Academy Sci.*, vol. 106, no. 27, pp. 10875–10876, 2009.
- [43] H. Jinno, K. Kuribara, M. Kaltenbrunner, N. Matsuhisa, T. Someya, T. Yokota, and T. Sekitani, "Printable elastic conductors with a high conductivity for electronic textile applications," *Nature communications*, no. 6, 7461, 2015.
- [44] X. Lin, and B.-C. Seet, "A linear wide-range textile pressure sensor integrally embedded in regular fabric," *IEEE Sensors J.*, vol. 15, no. 10, pp. 5384–5385, 2005.
- [45] J. Wissman, A. Perez-Rosado, A. Edgerton, B. M. Levi, Z. N. Karakas, M. Kujawski, and E. Smela, "New compliant strain gauges for self-sensing dynamic deformation of flapping wings on miniature air vehicles," *Smart Mater. Structures*, vol. 22, no. 8, 085031, 2013
- [46] X. Chen, K. Zhou, L. Zhang, and I. Bennion, "Dual-peak long-period fiber gratings with enhanced refractive index sensitivity by finely tailored mode dispersion that uses the light cladding etching technique," *Applied optics*, vol. 46, no.4, pp. 451–455, 2007.
- [47] M. A. Hanson, H. C. P. Jr, A. T. Barth, K. Ringgenberg, B. H. Calhoun, and J. H. Aylor, "Body area sensor networks: challenges and opporpentunities," *Computer*, vol. 42, no. 1, pp. 58–65, 2009.
- [48] K. Cherenack, K., and L. van Pieteron, "Smart textiles: challenges and opportunities," *J. Applied Physics*, vol. 112, no. 9, 091301, 2012.
- [49] T. S. Rappaport, S. Sun, R. Mayzus, H. Zhao, Y. Azar, K. Wang and F. Gutierrez, "Millimeter wave mobile communications for 5G cellular: It will work!," *IEEE Access*, vol. 1, pp. 335–349, 2013.
- [50] J. Du Preez, and S. Sinha, Millimetre-wave antennas: configurations and applications. Switzerland: Springer: 2016.
- [51] J. E. Freehafer, D.E. Kerr, Propagation of short radio waves. Chicago, U.S.A.: McGraw-Hill, Illinois: 1990.
- [52] K. -C. Huang, Z. Wang, Millimetre wave communication system. Hoboken, NJ: Wiley-IEEE Press: 2011.
- [53] T. S. Rappaport, R. W. Heath Jr, R. C. Daniels, J. N. Murdock, Millimeter wave wireless communications. Upper Saddle River, NJ: Prentice Hall, Pearson Education: 2015.
- [54] J. M. Jin, The finite element method in electromagnetics. Hoboken, NJ: Wiley: 2014.

- [55] L. F. Chen, C. K. Ong, C. P. Neo, V. V. Varadan, and V. K. Varadan, *Microwave Electronics: Measurement and Materials Characterization*, 1st ed. Chichester, U.K.: Wiley, 2004.
- [56] J. Krupka, and C. Weil, "Recent advances in metrology for the electromagnetic characterization of materials at microwave frequencies," In *12th Int. Conf. Microwaves Radar*, pp. 243–253, Krakow, Poland, 1998.
- [57] J. Baker-Jarvis, M. D. Janezic, and D. C. DeGroot, "High-frequency dielectric measurements," *IEEE Instrum. Meas. Mag.*, vol. 13, no. 2, pp. 24–31, 2010.
- [58] K. P. Latti, M. Kettunen, J. P. Strom, and P. Silventoinen, "A review of microstrip T-resonator method in determining the dielectric properties of printed circuit board materials," *IEEE Trans. Instrum. Meas.*, vol. 56, no. 5, pp. 1845–1850, 2007.
- [59] N. K. Das, S. M. Voda, and D. M. Pozar, "Two methods for the measurement of substrate dielectric constant," *IEEE Trans. Microwave Theory Tech.*, vol. 35, no. 7, pp. 636–642, 1987.
- [60] A. Lewandowski, A. Szyplowska, M. Kafarski, A. Wilczek, P. Barmuta, and W. Skierucha, "0.05–3 GHz VNA characterization of soil dielectric properties based on the multilayer TRL calibration," *Meas. Science and Technology*, vol. 28, no. 2, 024007.
- [61] T. Zwick, A. Chandrasekhar, C. W. Baks, U. R. Pfeiffer, S. Brebels, and B. P. Gaucher, "Determination of the complex permittivity of packaging materials at millimeter-wave frequencies," *IEEE Trans. Microw. Theory Techn.*, vol. 54, No. 3, pp. 1001–1010, 2006.
- [62] M. Q. Lee, and S. Nam, "An accurate broadband measurement of substrate dielectric constant," *IEEE Microwave Guided Wave Lett.*, vol. 6, no. 4, pp. 168–170, 1996.
- [63] A. P. Toda, and F. De Flaviis, "60-GHz substrate materials characterization using the covered transmission-line method," *IEEE Trans. Microw. Theory Techn.*, vol. 63, no. 3, pp. 1063–1075, 2015.
- [64] N. J. Farcich, J. Salonen, and P. M. Asbeck, "Single-length method used to determine the dielectric constant of polydimethylsiloxane," *IEEE Trans. Microw. Theory Techn.*, vol. 56, no. 12, pp. 2963–2971, 2008.
- [65] R. K. Shawl, B. R. Longj, D. H. Werner, and A. Gavrin, "The characterization of conductive textile materials intended for radio frequency applications," *IEEE Antennas Propag. Mag.*, vol. 49, no. 3, pp. 28–40, 2007.
- [66] Y. Ouyang, and W. Chappell, "Measurement of electrotiles for high frequency applications," in *IEEE Int. Microwave Symp. Digest*, Long Beach, CA, USA, June 2005, pp. 1679–1682.
- [67] J. J. Barroso, P. J. Castro, and J. P. L. Neto, "Electrical conductivity measurement through the loaded Q factor of a resonant cavity," *Int. J. Infrared Millimeter Waves*, vol. 24, no. 1, pp. 79–86, 2003.
- [68] P. Vesa, M. Riku Makinen, L. Juha Lilja, P. Ville, M. Pauliina, K. Markku, "Significance of Conductivity and Thickness of Thin Inkjet Printed Microstrip Lines", *12th IEEE Workshop Signal Propag. Interconnects*, Avignon, France, July 2008, pp. 1–4.
- [69] H. Shimasaki, T. Nakagawa, and M. Akiyama, "Measurement of the surface resistance of conductive textiles at microwave frequency" in *IEEE Asia Pacific Microwave Conf.*, pp. 2580–2583, Singapore, Singapore, Dec. 2009,
- [70] A. Pirhadi, F. Keshmiri, M. Hakkak, and M. Tayarani, "Analysis and design of dual band high directivity EBG resonator antenna using square loop FSS AS superstrate layer," *Progress Electromagn. Res.*, vol. 70, pp. 1–20, 2007.

- [71] R. Mittra, C. H. Chan, and T. Cwik, "Techniques for analyzing frequency selective surfaces-a review," *Proceedings IEEE*, vol. 76, no. 12, pp.1593–1615, 1988.
- [72] F. Yang, and Y. Rahmat-Samii, "Reflection phase characterizations of the EBG ground plane for low profile wire antenna applications," *IEEE Trans. Antennas Propag.*, vol. 51, no. 10, pp. 2691–2703, 2003.
- [73] R. C. Hadarig, M. E. De Cos, and F. Las-Heras, "Microstrip patch antenna bandwidth enhancement using AMC/EBG structures," *Int. J. Antennas Propag.*, vol. 2012, 843754, 2012.
- [74] L. Leger, T. Monediere, and B. Jecko, "Enhancement of gain and radiation bandwidth for a planar 1-D EBG antenna," *IEEE Microwave Compon. Lett.*, vol. 15, no. 9, pp. 573–575, 2005.
- [75] C. M. Lin, H. H. Su, J. C. Chiu, and Y. H. Wang, "Wilkinson power divider using microstrip EBG cells for the suppression of harmonics," *IEEE Microwave Compon. Lett.*, vol. 17, no. 10, pp. 700–702, 2007.
- [76] D. Qu, L. Shafai, and A. Foroozesh, "Improving microstrip patch antenna performance using EBG substrates," *IEE Proc. Microwaves, Antennas Propag.*, vol. 153, no. 6, pp. 558–563, 2006.
- [77] J. Chappell, M. P. Little, and L. P. Katehi, "High isolation, planar filters using EBG substrates," *IEEE Microwave Comp. Lett.*, vol. 11, no. 6, pp. 246–248, 2011.
- [78] R. Ikeuchi, and A. Hirata, "Dipole antenna above EBG substrate for local SAR reduction," *IEEE Antennas Wireless Propag. Lett.*, vol. 10, pp. 904–906, 2011.
- [79] F. R. Yang, Y. Qian, R. Coccioli, and T. Itoh, "A novel low-loss slow-wave microstrip structure," *IEEE Microwave Guided Wave Lett.*, vol. 8, no. 11, pp. 372–374, 1998.
- [80] R. J. Langley, E. A. Parker, "Double square frequency selective surfaces and their equivalent circuit", *Electron. Lett.*, vol. 19, pp. 675–677, 1983.
- [81] S. Zhu, and R. Langley, "Dual-band wearable antennas over EBG substrate," *Electron. Lett.*, vol. 43, no. 3, pp. 141–142, 2007.
- [82] S. Zhu, R. Langley, "Dual-band wearable textile antenna on an EBG substrate," *IEEE Trans. Antennas Propag.*, vol. 57, no. 4, pp.926–935, 2009.
- [83] D. H. Werner, S. Ganguly, "An overview of fractal antenna engineering research", *IEEE Antennas Propag. Mag.*, vol. 45, pp. 38–57, 2003.
- [84] Y. Yang, J. J. Huang, Z. H. Feng, "A novel fractal multi-band EBG structure and its application in multi-antennas", *Int. Symp. Antennas Propag. Soc.*, pp. 5447–5450, Honolulu, HI, USA, Jun 2007.
- [85] H. P. Tian, L. M. Zhao, Q. Luo, J. T. Huang, Y. F. Ji, "Wideband quasi-isotropic H-shaped slot fractal UC-EBGs with alternately arranged symmetrical unit cells", *J. Electromagn. Waves Appl.*, vol. 27, pp. 962–968, 2009.
- [86] J. Zhang, G. Ci, Y. Cao, N. Wang and H. Tian, "A wide bandgap slot fractal UC-EBG based on Moore space-filling geometry for microwave application," *IEEE Antennas Propag. Lett.*, vol. 16, pp. 33–37, 2017.
- [87] Xu Yang, Ying Liu, Yun-Xue Xu, Shu-xi Gong, "Isolation enhancement in patch antenna array with fractal UC-EBG structure and cross slot", *IEEE Antennas Propag. Lett.*, vol. 16, pp. 2175–2178, 2017.
- [88] F.-Q. Shan, B.-X. Gao, "Novel compact photonic band-gap structure using rectangular increasing-distance spiral slots", *Microw. Opt. Technol. Lett.*, vol. 43, no. 6, pp. 537–539, 2004.
- [89] M. J. Al-Hasan, T. A. Denidni, A. Sebak, "A new UC-EBG based dielectric resonator antenna for millimeter-wave applications", in *Proc. IEEE Int. Symp. on Antennas Propag.*, pp. 1274–1276, Spokane, WA, USA, Aug. 2011.

- [90] O. M. Haraz, A. Elboushi, S. A. Alshebeili, and A. Sebak, "Dense Dielectric Patch Array Antenna With Improved Radiation Characteristics Using EBG Ground Structure and Dielectric Superstrate for Future 5G Cellular Networks", *IEEE Access*, vol. 2, pp. 909–913, 2014.
- [91] R. D. Seager, A. Chauraya, J. Bowman, M. Broughton, R. Philpott, and N. Nimkulrat, "Fabric based frequency selective surfaces using weaving and screen printing," *Electron. Lett.*, vol. 49, no. 24, pp. 1507–1509, 2013.
- [92] A. Y. Ashyap, Z. Z. Abidin, S. H. Dahlan, H. A. Majid, S. M. Shah, M. R. Kamarudin, and A. Alomainy, "Compact and low-profile textile EBG-based antenna for wearable medical applications," *IEEE Antennas Propag. Lett.*, vol. 16, pp. 2550–2553, 2017.
- [93] A. Tennant, W. Hurley and T. Dias, "Experimental knitted, textile frequency selective surfaces," *Electro. Lett.*, vol. 48, no. 22, pp. 1386–1388, 2012.
- [94] A. Tennant, W. Hurley and T. Dias, "Knitted, textile, high impedance surface with integrated conducting vias," *Electro. Lett.*, vol. 49, no. 1, pp. 8–10, 2013.
- [95] Y. Hao, A. Brizzi, R. Foster, M. Munoz, A. Pellegrini and T. Yilmaz, "Antennas and propagation for body-centric wireless communications: current status, applications and future trend," *2012 IEEE International Workshop Electromag.: Appl. Student Innovation Competition*, Chengdu, Sichuan, 2012, pp. 1–2, Aug 2012.
- [96] N. F. M. Aun, P. J. Soh, A. A. Al-Hadi, M. F. Jamlos, G. A. E. Vandenbosch and D. Schreurs, "Revolutionizing wearables for 5G: 5G technologies: recent developments and future perspectives for wearable devices and antennas," *IEEE Microwave Mag.*, vol. 18, no. 3, pp. 108–124, 2017.
- [97] J. Virtanen, L. Ukkonen, T. Bjorninen, A. Z. Elsherbeni, and L. Sydänheimo, "Inkjet-printed humidity sensor for passive UHF RFID systems," *IEEE Trans. Instrum. Meas.*, vol. 60, no. 8), pp. 2768–2777, 2011.
- [98] F. Molina-Lopez, D. Briand, and N. F. De Rooij, "All additive inkjet printed humidity sensors on plastic substrate," *Sensors Actuators B: Chemical*, vol. 166, pp. 212–222, 2012.
- [99] J. Fernández-Salmerón, A. Rivadeneyra, M. A. C. Rodríguez, L. F. Capitan-Vallvey, and A. J. Palma, "HF RFID tag as humidity sensor: Two different approaches," *IEEE Sensors J.*, vol. 15, no.10, pp. 5726–5733, 2015.
- [100] K. G. Ong, Design and Application of Planar Inductor–Capacitor Resonant-Circuit Remote Query Sensor, Dissertation, University of Kentucky, 2000.
- [101] K. J. Loh, J. P. Lynch, and N. A. Kotov, "Inductively coupled nanocomposite wireless strain and pH sensors," *Smart Structures Sys.*, vol. 4, no. 5, pp. 531–548, 2008.
- [102] V. K. Varadan, P. T. Teo, K. A. Jose, and V. V. Varadan, "Design and development of a smart wireless system for passive temperature sensors," *Smart Materials Structures*, vol. 9, no. 4, pp. 379.
- [103] A. Daliri, A. Galehdar, S. John, C. H. Wang, W. S. Rowe, and K. Ghorbani, "Wireless strain measurement using circular microstrip patch antennas," *Sensors Actuators A: Physical*, vol. 184, pp. 86–92, 2012.
- [104] L. Y. Chen, B. C. K. Tee, A. L. Chortos, G. Schwartz, V. Tse, D. J. Lipomi, and Z. Bao, "Continuous wireless pressure monitoring and mapping with ultra-small passive sensors for health monitoring and critical care," *Nature commun.*, vol. 5, 5028, 2014.
- [105] Drexel Researchers Develop Smart Fabric Belly Band, Drexel University, April 2016. Available at <http://drexel.edu/now/archive/2014/May/Belly-Band/>

- [106] N. H. M. Rais, P. J. Soh, F. Malek, S. Ahmad, N. B. M. Hashim, and P. S. Hall, "A review of wearable antenna," In *Antennas Propag. Conf.*, pp. 225–228, Loughborough, UK, Nov, 2009.
- [107] I. J. Bahl and S. S. Stuchly, "Analysis of a microstrip covered with a lossy dielectric," *IEEE Trans. Microw. Theory Techn.*, vol. 28, no. 2, pp. 104–109. 1980.
- [108] Anritsu Corporation, *Understanding vector network analysis*, Product guide, March, 2018.
- [109] J. Svacina, "Analysis of multilayer microstrip lines by a conformal mapping method," *IEEE Trans. Microw. Theory Techn.*, vol. 40, no. 4, pp. 769–772. 1992.
- [110] D. E. Zelenchuk, V. Fusco, G. Goussetis, A. Mendez and D. Linton, "Millimeter-wave printed circuit board characterization using substrate integrated waveguide resonators," *IEEE Trans. Microw. Theory Techn.*, vol. 60, no. 10, pp. 3300–3308. 2012.
- [111] A. Elhawil, C. Roda Neve, B. Olbrechts, I. Huynen, J.-P. Raskin, G. Poesen, L. Zhang, J. Stiens, R. Vounckx, "Contactless monitoring of Si substrate permittivity and resistivity from microwave to millimeter-wave frequencies", *Microw. Opt. Technol. Lett.*, vol. 52, no. 11, pp. 2500–2505, 2010.
- [112] S. W. Harmer, N. Rezgui, N. Bowring, Z. Luklinska, and G. Ren, "Determination of the complex permittivity of textiles and leather in the 14–40 GHz millimetre-wave band using a free-wave transmittance only method," *IET Microw., Antennas Propag.*, vol. 2, no. 6, pp. 606–614, 2008.
- [113] H.-D. Chen, "Broadband CPW-fed square slot antennas with a widened tuning stub," *IEEE Trans. Antennas Propag.*, vol. 51, no. 8, pp. 1982–1986, 2003
- [114] C. Gabriel, *A compilation of the dielectric properties of body tissues at RF and microwave frequencies*, Radiofrequency Radiation Division, Brooks AFB, 1996.
- [115] P. Salonen and Y. Rahmat-Samii, "Textile antennas: Effects of antenna bending on input matching and impedance bandwidth," *2006 First European Conf. Antennas Propag.*, Nice, France, 2006, pp. 1–5.
- [116] M. U. Talha and J. Ahmad, "Body area networks (BANs)—An overview with smart sensors based telemedical monitoring system", *Int. J. Computer Applicat.*, vol. 84, no. 8, 2013, pp. 20–23, 2013.
- [117] J. J. Park, and M. Taya, "Design of micro-temperature sensor array with thin film thermocouples," *J. Electron. Packag.*, vol. 127, no. 3, pp. 286–289, 2005.
- [118] J. Jeon, H. B. R. Lee, and Z. Bao, "Flexible wireless temperature sensors based on Ni microparticle-filled binary polymer composites," *Adv. Mater.*, vol. 25, no. 6, pp. 850–855, 2013.
- [119] N. T. Tien *et al.* (2014). "A flexible bimodal sensor array for simultaneous sensing of pressure and temperature," *Adv. Mater.*, vol. 26, no. 5, 796–804, 2014.
- [120] J. Yang, D. Wei, L. Tang, X. Song, W. Luo, J. Chu, and C. Du, "Wearable temperature sensor based on graphene nanowalls," *RSC Advances*, vol. 5, no. 32, pp. 25609–25615, 2015
- [121] J. H. Jang and J. I. Han, "Cylindrical relative humidity sensor based on poly-vinyl alcohol (PVA) for wearable computing devices with enhanced sensitivity," *Sensors Actuators A: Physical*, vol. 261, pp. 268–273, 2017.
- [122] J. Weremczuk, G. Tarapata and R. Jachowicz, "Humidity sensor printed on textile with use of ink-jet technology," *Procedia Engineering* 47, Krakow, Poland, 2012, pp. 1366–1369.
- [123] Institute for Applied Physics, Italian National Research Council, "Dielectric properties of body tissues in the frequency range 10 Hz–100 GHz," [Online]. Available: <http://niremf.ifac.cnr.it/tissprop/htmlclie/htmlclie.php>.

- [124] S. Muruganand, S. K. Narayandass, D. Mangalaraj, and T. M. Vijayan, "Dielectric and conduction properties of pure polyimide films," *Polymer Int.*, vol. 50, no. 10, pp. 1089–1094, 2001.
- [125] J. W. Hearle and W. E. Morton, *Physical properties of textile fibres*. Boca Raton, FL: CRC Press. 1997.
- [126] C. Hertleer, A. Van Laere, H. Rogier, and L. Van Langenhove, "Influence of relative humidity on textile antenna performance," *Textile Res. J.*, vol. 80, no. 2, pp. 177–183, 2010.
- [127] K. Wu, P. Burasa, T. Djerafi and N. Constantin, "Millimeter-wave identification for future sensing, tracking, positioning and communicating systems," *2016 Global Symp. Millimeter Waves ESA Workshop on Millimetre-Wave Technology Applications*, Espoo, Finland, 2016, pp. 1–4.
- [128] D. Hotte, R. Siragusa, Y. Duroc, and S. Tedjini, "Design of a planar passive MMID tag antenna," *IET Microwave Antenna Propag.*, vol. 11, no. 12, pp. 1751–8725, 2017.